Numerical study of wind turbine wakes using modal-decomposition techniques and stability analysis

Department of Mechanics, Mathematics and Management

Mechanical and Management Engineering

Ph.D. Program

SSD: ING-IND/08 - Fluid Machinery

Final dissertation

Numerical study of wind turbine wakes using modal-decomposition techniques and stability analysis

by

Giovanni De Cillis

Supervisors:

Prof. Pietro De Palma

Prof. Stefania Cherubini

Coordinator of the Ph.D. Program:

Prof. Giuseppe P. Demelio

Course n° 33, 01/11/2017 - 31/10/2020

Department of Mechanics, Mathematics and Management

Mechanical and Management Engineering

Ph.D. Program

SSD: ING-IND/08 - Fluid Machinery

Final dissertation

Numerical study of wind turbine wakes using modal-decomposition techniques and stability analysis

by

Giovanni De Cillis

Referees:

Prof. Carlo Cossu

Prof. Antonio Segalini

Supervisors:

Prof. Pietro De Palma

Prof. Stefania Cherubini

Coordinator of the Ph.D. Program:

Prof. Giuseppe P. Demelio

Course n°33, 01/11/2017 - 31/10/2020

Abstract

This thesis is focused on numerical analysis of wind turbines wakes. The flow over wind turbines is simulated performing Large Eddy Simulations (LES), where the rotor blades are modeled using the Actuator Line Method, whereas the Immersed Boundary Method is employed for tower and nacelle. The effect of tower and nacelle on wake dynamics is investigated by means of Proper Orthogonal Decomposition (POD) of numerical velocity data produced by two LES of a model wind turbine: one accounts only for the blades effect; the other includes also tower and nacelle. The turbine operates at Reynolds number $Re = 6.3 \times 10^5$ and tip-speed ratio $\lambda = 3$. The two simulations are analysed and compared in terms of mean flow fields and POD modes that mainly characterize the wake dynamics. In the rotor-only case, the most energetic modes in the near wake are composed of high-frequency tip and root vortices, whereas in the far wake, low-frequency modes, mostly located in the wake shear layer region, are found. When tower and nacelle are included, low-frequency POD modes are present already in the near wake, linked to the von Karman vortices shed by the tower. These modes interact non linearly with the tip vortices in the far wake, generating new low-frequency POD modes, some of them lying in the frequency range of wake meandering. An analysis of the mean kinetic energy entrainment of each POD mode shows that tip vortices sustain the wake mean shear, whereas low-frequency modes contribute to wake recovery. This explains why tower and nacelle induce a faster wake recovery.

The proper orthogonal decomposition, despite being able to isolate energetic flow structures in the wake, does not provide any physical information on their origin. In an attempt to determine the physical mechanisms responsible for the emergence of these flow structures, the numerical data obtained without tower and nacelle are

further analyzed performing two-dimensional modal and non-modal stability analysis of the turbulent mean flow developing downstream of a wind turbine rotor. Linear stability and optimal forcing analyses have been carried out in different cross-sections sufficiently far from the rotor, where nonparallel effects are rather weak. The frequency content and spatial structure of the most amplified perturbations are compared with that of the most energetic coherent structures recovered by POD analysis. Results show that most unstable modes computed relatively close to the rotor resemble large-scale oscillations isolated by the POD. Moving downstream, this matching is no longer verified; however, restricting the stability analysis to waves having streamwise wavenumber consistent with that of the POD analysis, we find three slightly stable eigenmodes bearing a strong resemblance with the most energetic POD modes.

The analyses described above are based on a model wind turbine; however utility-scale wind turbines operate at far larger Reynolds number, of the order of 10^8 and higher tip-speed ratio. These differences can lead to a different wake dynamics. For this reason a reference utility-scale wind turbine (i.e. the NREL 5-MW) is simulated and analyzed using Proper Orthogonal Decomposition and Dynamic Mode Decomposition (DMD) in its sparsity promoting variant, which selects a limited subset of dynamically relevant modes. In contrast to the model wind turbine, the wake meanflow is, in this case, essentially aligned with the rotor axis and axisymmetric, suggesting a weaker impact of the tower. The coherent structures isolated by the two modal-decomposition techniques are similar to those observed for the model turbine, but a weaker interaction of tower's wake and tip vortices is confirmed and a faster breakdown of the latter is reported. Furthermore, POD and DMD of the flow field provide rather different results. Large-scale, low-frequency oscillations are not present among the most energetic POD modes. On the contrary, sparsity-promoting dynamic mode decomposition suggests that large-scale structures, developing far from the rotor, are relevant to the flow dynamics, despite their energetic content is not sufficiently high to overcome that of the tip vortices and their harmonics, which are among the first

POD modes. This result demonstrates that while Proper Orthogonal Decomposition is efficient at identifying coherent structures, it may not be suitable for building a low-dimensional model of a wind turbine wake, while sparsity-promoting DMD can be a better choice.

Contents

List of Figures

List of Tables

Chapter 1

Introduction

1.1 Historical background

Wind has been a source of power for humankind for millenia. The first historical use of wind as a power source was to propel sailing ships and boats, with the first recorded proofs belonging to the Egyptians and dating back to 3200 B.C.. Later, another wind-powered tool of fundamental importance developed: the windmill. The first reliable written account of the use of windmills dates to 10th century, and describes how Persian, in the region of Sistan, exploited the wind power to drive mills and pump water for irrigation [95]. Persian windmills were vertical-axis wind turbines consisting of a vertical shaft connected to a spoked reel with 6 to 12 upright ribs, each covered with cloth to form separate sails. However, Persian windmills never came into use into northern Europe, where, instead, another kind of windmill became widespread from the twelfth century. The european design of windmills was characterized by the horizontal axis of rotation with the rotor facing the wind, which provided a larger efficiency than its counterpart with vertical axis rotor. In the late 19th and early 20th centuries, the conversion of wind energy to electrical energy was conceived almost simultaneously in multiple place. In the same years the advent and development of airplanes gave rise to a growing interest in aerodynamics research, which strongly

contributed to the development of wind turbines. Professor Albert Betz and other aerodynamicists, in those years laid the foundation for wind energy science. In the following years different wind-turbine designs developed; the most seminal, among these, for the development of modern wind industry was the so-called "Danish design". The latter owes its origin to Johannes Juul, who built in 1957 a cost-effective and very robust three-bladed horizontal axis wind turbine, equipped with an asynchronous generator and connected directly to the grid (see Figure 1.1). However, about 30 years had to pass before wind energy could gain visibility as a commercial power generation, due to the 1973 oil crisis. The economical and technological growth of wind energy lasted until the oil price rose fell again in 1980. As the 21th century began fossil fuels prices were still low, nevertheless concerns about fossil fuels depletion and global warming rekindled interest in renewable energy technologies, which experienced a tremendous growth in the last 20 years, making wind energy competitive with respect to fuel-based energy.

1.2 Motivation

In order to limit the negative impact of energy production by fossil fuels on the environment and climate equilibrium, in the upcoming years a larger fraction of energy demand must be satisfied by renewable sources. In 2018, 80% of the global energy consumption has been provided by fossil fuels (coal, oil and gas) [44]. Moreover, world energy consumption is growing, especially driven by some emerging countries: global energy demand increased by 2.1% in 2017 [43] and 2.3% in 2018 [44], and it is expected about to double by 2030 [14]. The energy production from renewable sources increased by 4% in 2018 [44], accounting for almost one-quarter of global energy demand growth. Wind energy contributed for about 30% to this increment and is expected to be one of the key technologies for clean energy production in the future. In fact, renewable power capacity is expected to expand by 50% between 2019 and 2024 [79], onshore

Figure 1.1: The three-bladed wind turbine build by J. Juul in 1957 near Gedser (Zealand, Denmark). Juul's turbine established the so-called "Danish design" which was adopted by manufacturers around the globe as reference for the development of modern wind turbines.

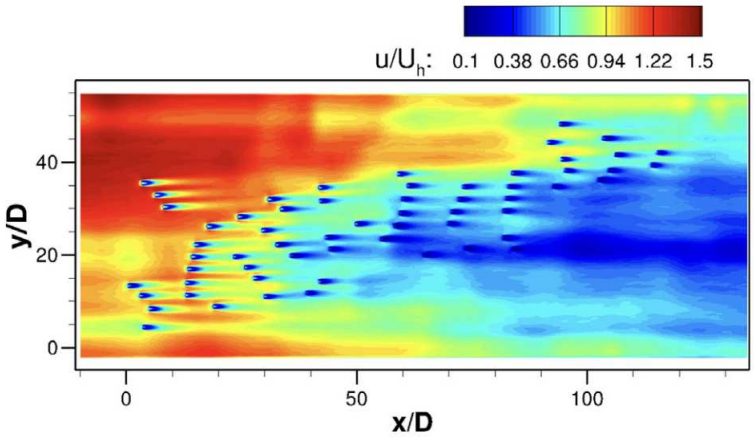

Figure 1.2: Numerical simulation of the Invenergy Vantage wind farm (located in the Washington state, USA) in complex terrain [111]. Color contours of the time-averaged downwind velocity on a plane parallel to and located at $z_h = 80m$ above the ground.

wind energy production representing one-quarter of this growth. Achieving such a target requires the design and installation of new large wind farms, constituted of up to hundreds of turbines, and the upgrade of existing ones exploiting new technologies for improving efficiency and reliability. The performance of wind farms are closely related to the dynamics of the atmospheric boundary layer and therefore to mesoscale meteorological processes [87, 86], as well as landscape characteristics [74, 41] and the design of the farms themselves [110, 94]. When clustered in large farms, a great part of the wind turbines operates in the wake of upwind turbines, as can be observed in Figure 1.2. The velocity deficit and the high turbulence level of the incoming flow induces power losses and fatigue blade loading [9, 84, 101]. For this reason, understanding the dynamics of wind turbine wakes is fundamental for the design and optimization of wind turbines and farms, where, limiting the wake losses, is, indeed, one of the key issues. However, this is a challenging task due to the multi-scale nature of atmospheric turbulence spreading over a wide range of spatial scales ranging from millimeters, corresponding to the Kolmogorov turbulence length scale, influencing the flow past the blade airfoils, to thousands of kilometers, linked to the horizontal length scale of the vortices in the atmosphere, influencing the interaction

between the atmospheric boundary layer and large wind farms [78]. The wind energy research community is indeed engaged in the study of a variety of fluid dynamics topics covering all the length scales involved in wind energy technology and their interaction.

1.3 Wake dynamics and coherent structures

As mentioned above, the study of wind turbine wakes is of fundamental importance in the context of wind farms, where a large number of turbines can be affected by the wake of upstream turbines. In wakes produced by horizontal-axis wind turbines two regions are typically recognized: the near wake and the far wake [106]. The near wake is the region just behind the rotor where the dynamics of the flow is determined by the geometry and working conditions of the rotor itself, namely, by the number of blades, blade aerodynamics, tip vortices, rotational speed. The far wake is the region beyond the near wake, where the structures linked to the bladesâĂŹ aerodynamics are no longer visible and the flow is dominated by convection and turbulence diffusion. The latter region is also reported to show large-scale low-frequency oscillation referred to as wake meandering [66], the origin of the which still being a matter of scientific debate [63, 48, 52]. In order to decrease losses due to wakes and maximize power harvesting, different control strategies have been developed at the farm level, where coupling between the turbines is taken into account. These include torque gain control, pitch and yaw and tilt angle control [20, 54, 70, 23, 22]. In any case a fast wake recovery is desired, which is closely related to the turbulence intensity of the flow, and consequently to atmospheric stability. It has been shown that during day-time (unstable regime) wind turbine wakes experience a faster recovery with respect to night-time (stable regime), being the former characterized by a higher turbulence intensity [78]. Therefore stable atmospheric conditions are the most critical with regard to power losses due to wake effects, where turbulence is mainly produced by the

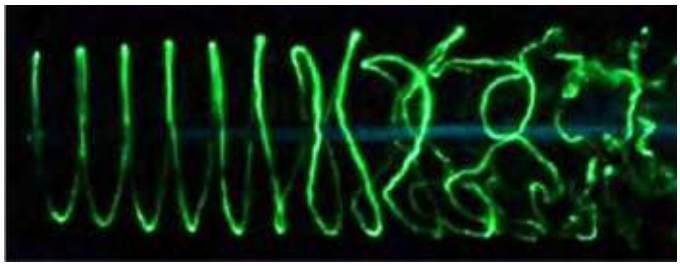

Figure 1.3: Dye visualization of a single tip-vortex helix subject to pairing instability. [59]

turbines. In the near wake, coherent helicoidal vortex structures shed from the tip and the root of the rotor blades undergo instability mechanisms and break down forming small-scale turbulent structures (Figure 1.3). At the center of the near wake there is the so-called hub vortex, a vortical structure elongated in the streamwise direction and characterized by a single-helix counter-winding periodic instability, which may interact with the tip vortices triggering the breakdown of the vortex system [71, 52]. The breakdown of coherent vortices shed by the rotor defines qualitatively the boundary between the near and the far wake, which is, therefore characterized by a higher turbulence intensity promoting the entrainment of the outer flow and consequently the wake recovery [48, 1].

Although many studies have essentially focused on the vortical dynamics induced by the rotor, the tower and nacelle are now believed to have a fundamental role in the breakdown of the vortices shed by the rotor and on the consequent wake recovery. The wake of the tower appears to promote the breakdown of the tip vortices, increasing the mean kinetic energy flux into the wake [85]. Similarly to background turbulence, tower-wake interactions also induce an asymmetry of the wake deficit, leading to a decreased efficiency and increased blade stress levels for a turbine placed downstream [76]. Moreover, the role of the nacelle on the origin of wake meandering in the near field of a single turbine has been recently investigated. The helical hub vortex that forms behind the turbine nacelle interacts with the tip vortices while expanding radially, leading to turbulent coherent structures in the far wake that can be connected to the wake meandering phenomenon [29]. For this reason, incorporating the presence of

the nacelle in wind farm simulations is crucial for accurately predicting the dynamics of wake meandering as well as the loads on downwind turbines [30]. Nevertheless, most of these studies including the effect of tower and nacelle focus on the features of the mean flow only, failing to capture unsteady phenomena due to the interaction of coherent structures with different frequencies and structures, which may have a strong impact on wake entrainment and recovery. An analysis of the influence of both tower and nacelle on the main frequencies and spatial features of the coherent structures developing in the turbine wake, which is at the moment still lacking, will be crucial to determine the impact of these components of a wind turbine on the entrainment and recovery of its wake and represents an objective of the present work.

One of the most widely used methods for extracting coherent structures from flow data is the Proper Orthogonal Decomposition (POD) [62, 96, 13]. POD allows one to find a finite set of deterministic modes whose linear combination optimally reconstructs the energy of a set of stochastic flow data. Such a technique has been recently introduced in the study of the flow through wind turbines and wind farms. Andersen et al.[4] simulated the turbulence in the interior of a wind farm using large eddy simulation and the actuator line method. The flow was reconstructed by applying the POD to the velocity field extracted in a plane perpendicular to the streamwise direction. VerHulst & Meneveau[105] proposed one of the first applications of the three-dimensional POD analysis to the study of a wind farm. They classified the resulting POD modes into four categories according to their general structure and determined how many of these POD modes are needed to capture a large fraction of the turbulent kinetic energy of the flow. Sarmast et al.[89] focused on the stability properties of the tip vortices and the mechanisms leading to vortex pairing by means of large eddy simulation (LES), continuing the work previously performed by Ivanell et al.[49]. The flow was perturbed by using low-amplitude excitations near the tip of the blades and the POD technique was employed to extract the unstable modes, demonstrating a prominence of the mutual inductance phenomenon. Also Bastine et

al.[12] applied the two-dimensional POD to the LES data of the wake of a wind turbine, considering a more realistic incoming flow representing a turbulent atmospheric boundary layer (ABL) in the case of a neutrally stratified atmosphere. Hamilton et al.[35, 37] investigated wake interaction and recovery dynamics in different wind turbine array configurations using the POD applied to velocity measurements. Resulting modes were used for constructing low-dimensional models of turbulence statistics. Double POD applied on a similar dataset [36] has indicated that the structure of the wake can be described using a small subset of the original mode basis, providing a total reduction to 0.015% of the degrees of freedom of the wind turbine wake. POD has been also used to extract coherent structures of the thermally stratified wind turbine array boundary layer [2], showing that, in the unstable and neutrally stratified regimes, the structures related to the atmospheric boundary-layer flow, which are beneficial for wake recovery, dominate over those introduced by the presence of the turbines. The effect of the spacing between wind turbines on POD modes has been assessed by Ali et al. [3], showing that modifying the streamwise and spanwise spacing leads to changes in the background structure of the turbulence as well as on power producted. Numerous other works focused on the wake of a single wind turbine. Sorensen et al.[98] applied the POD on the LES results for a single-turbine wake analyzing the flow field in planes behind the rotor. The spatial development of the POD modes was employed to describe the breakdown process in the transition region from the near wake to the far wake. Bastine et al.[11] applied the POD technique to LES data, extracted in one plane in the wake, to investigate a new stochastic modeling approach for the wake of a wind turbine. They showed that approximately six POD modes are sufficient to capture the load dynamics on large temporal scales. Debnath et al.[26] studied the dynamics of wind turbine wakes and instabilities of helicoidal tip vortices using three-dimensional POD. Snapshots of the velocity field obtained from the LES of an isolated wind turbine were considered as dataset. The dominant wake structures were selected for the formulation of a reduced order model.

The present work aims at assessing the effect of tower and nacelle on the dynamics of coherent structures in the wake of wind turbines using large eddy simulations and POD analysis.

However, despite extracting the most energetic flow structures, POD analysis does not provide in general a deep insight on the physical origin of coherent structures, which might be due to modal or non-modal instability mechanisms. Linear stability analysis of time-averaged mean flows has proved to be a powerful tool able to predict low-frequency coherent oscillations in different flow configurations [8, 33, 102]. Following this approach, by means of a 'local', one-dimensional analysis carried out in the vicinity of the rotor, Iungo et al.[47] found highly unstable eigenmodes with temporal frequency typical of the wake meandering and associated with small azimuthal wavenumbers. A similar one-dimensional analysis has been then performed by Iungo et al.[107] adding different eddy viscosity models to take into account the turbulent diffusion of perturbations. This analysis provided eigenspectra with maximum growth rate at temporal and azimuthal wavenumbers corresponding to those typical of the wake meandering phenomenon. The influence of turbulence intensity and blade aerodynamics on the hub-vortex instability frequencies and related flow structures has been studied by Ashton et al.[6, 5] using a model mean flow. Viola et al.[108] have carried out a two-dimensional stability analysis in the cross-planes close to the rotor of a model wind turbine immersed in an atmospheric boundary layer, finding once again unstable modes with frequencies typical of the hub-vortex instability. More recently, Ferrer et al.[27] used stability and sensitivity analysis on a wall-parallel plane passing through the hub center of a wind turbine rotor to design a passive way to control the primary wake destabilization at low Reynolds number. Restraining the analysis to a two-dimensional configuration, they showed that adding a localized control force in flow regions identified by the sensitivity analysis is able to stabilize the wake. Although based on a simplified flow configuration at low Reynolds number, this work indicates that, for controlling the wake, one should modify the velocity gradient

close to the turbine in a non trivial way, as predicted by sensitivity analysis. Linear stability eigenmodes, together with their adjoint counterparts [31], are thus able to provide valuable information on the shape and location of active or passive means to control the spatial structure, recovery rate, and frequency content of the wake behind a wind turbine.

Despite the importance of linear stability analysis for the identification and control of coherent structures, only a few stability studies, mostly focused on the hub-vortex instability, have been carried out on this peculiar flow. A detailed analysis of the main flow features found by modal and non-modal instability methods, and on their relevance with respect to the coherent structures that populate the turbulent flow, is still lacking in the literature. In fact, apart from the hub-vortex instability recovered by Iungo et al. in the immediate vicinity of the rotor, the correspondence of other linear instabilities to energetic coherent structures extending towards the far wake region has not been investigated yet. Moreover, the possible relevance of non-modal stability mechanisms, able to provide a strong amplification of some particular perturbations, in the development of coherent structures in wind turbine wakes, has not been assessed yet. Non-modal mechanisms such as the amplification of harmonic forcing at particularly receptive frequencies, can have a strong relevance in the development of coherent structures within the wake. In fact, non-modal amplification mechanisms may allow a fast transfer of energy from the meanflow to some waves having particularly receptive frequencies, allowing the displacing of energy among different regions of the wake and strongly affecting wake recovery. The capability of resolvent (optimal forcing) analysis to identify the most energetic flow structures in asymptotically stable flows has been recently proven for different flow configurations [61, 32, 92], and the importance of reynolds stresses modeling and forcing statistics has been highlighted [68, 103]. For these reasons, in the present thesis, we aim at investigating in detail the modal and non-modal stability of the turbulent meanflow developing downstream of a wind turbine rotor.

Low-dimensional models based on the modal decomposition of complex flows are often sought, also in the wind-energy field. The orthogonality of the resulting modes makes the POD the commonly-chosen basis for the formulation of a Reduced-Order Model (ROM). Very recently, Hamilton et al.[38] applied POD to LES data in order to construct a ROM of turbine wakes using polynomial reconstruction able to quantify the interaction and evaluation of POD modes. Fortes-Plaza et al.[28] realized a ROM base on POD of LES data of yaw-controlled wake-interacting wind turbines. However the most-energetic POD modes may not be dynamically relevant, therefore the selection of a low-dimensional basis for the realization of a reduced-order model is not trivial [45]. Another data-driven modal-decomposition technique that gained popularity in the last ten years is the Dynamic Mode Decomposition (DMD), introduced by Schmid in 2010 [90]. This technique finds eigenvalues and eigenvectors of a linear operator approximating the nonlinear dynamics embedded in the data sequence and it has been recently exploited for the formulation of ROMs of wind-turbine-relevant flows. Iungo et al. [46] realized a reduced-order model of wind turbine wakes, based on the dynamic mode decomposition of LES flow data of wind turbines operating under different operational regimes. Le Clainche et al. [57] used the dynamic mode decomposition of Lidar measurements to build a reduced-order model of the wind velocity upstream of an horizontal-axis wind turbine. DMD modes are usually ranked according to their amplitude at the first snapshot of the data-sequence. Such a criterion for the selection of a limited subset of dynamic modes can lead to poor quality of approximation of numerically generated snapshots and, therefore, to poor predictive capability of low-dimensional models. For this reason different variants of the standard algorithm, aiming at extracting a limited subset of flow features that optimally approximate the original data sequence, have been developed, such as the Optimized DMD [17] or the Sparsity-Promoting DMD [51]. The latter technique is employed in the present thesis to analyze LES data of the wake produced by a utility-scale wind turbine. The results are also compared with the proper orthogonal decomposition of

the same dataset.

1.4 Thesis structure

The present thesis focuses on numerical modeling and analysis of coherent structures characterizing wind turbine wakes. Chapter 2 provides the numerical methods employed for simulations and analyses. In chapter 3 the numerically-simulated flow in the presence and absence of tower and nacelle has been analyzed using the proper orthogonal decomposition technique which allowed us to identify the most relevant coherent structures. The outcomes of the POD analysis in the two different configurations (rotor-only and complete turbine) are compared in order to understand the role of tower and nacelle in wake recovery and meandering. Chapter 4 provides a bilocal stability and resolvent analysis of the wake meanflow obtained in the absence of tower and nacelle. The capability of linear meanflow analysis to model coherent structures arising in a wind turbine wake is assessed by comparison with proper orthogonal decomposition. In chapter 5 the wake produced by a utility-scale wind turbine is analyzed using the proper orthogonal decomposition and the sparsity-promoting dynamic mode decomposition. Results are compared and the main differences are highlighted in order to evaluate which of the two methods is more suitable for dimensionaly reduction. Concluding remarks are drawn in chapter 6.

Chapter 2

Methodology

2.1 Governing equations

The flow developing around wind turbines can be assumed to be incompressible, since even at the blades' tip the Mach number is still farly low ($Ma \leq 0.25$). Therefore the numerical simulations considered in the present thesis are based on the incompressible Navier-Stokes equations together with the continuity constraint,

$$\frac{\partial U_i}{\partial t} + \frac{\partial U_i U_j}{\partial x_j} = -\frac{1}{\rho}\frac{\partial P}{\partial x_i} + \nu \frac{\partial^2 U_i}{\partial x_j \partial x_j} + F_i, \tag{2.1a}$$

$$\frac{\partial U_i}{\partial x_i} = 0. \tag{2.1b}$$

where U_i and F_i are the velocity and the generic force per unit mass along the i direction, P is the pressure, ρ the fluid constant density, ν the kinematic viscosity, x_i the i^{th} spatial coordinate and t the time. The above equations (2.1b) can be rewritten into a nondimensional form by choosing reference length and velocity scales, denoted by L and U_0. The reference scales are chosen by convention and represent a characteristic dimension and velocity of the problem under study. In the context of wind turbines the incoming wind speed U_∞ and the rotor diameter D are usually chosen as reference velocity and length. The nondimensionalization of the Navier-

Stokes equations leads to the following nondimensional equations:

$$\frac{\partial U_i^*}{\partial t^*} + \frac{\partial U_i^* U_j^*}{\partial x_j^*} = -\frac{\partial P^*}{\partial x_i^*} + \frac{1}{Re}\frac{\partial^2 U_i^*}{\partial x_j^* \partial x_j^*} + F_i^*, \tag{2.2a}$$

$$\frac{\partial U_i^*}{\partial x_i^*} = 0, \tag{2.2b}$$

where the nondimensional physical variables, defined in (2.3), are marked with an asterisk (*) and Re is the Reynolds number, defined as $Re = U_0 L/\nu$.

$$U_i^* = \frac{U_i}{U_0} \qquad P* = \frac{P}{\rho U_0^2} \qquad F_i^* = \frac{F_i L}{U_0^2} \qquad x_i^* = \frac{x_i}{L} \qquad t^* = \frac{tL}{U_0} \tag{2.3}$$

The Reynolds number is the only nondimensional parameter which appears in the governing equations. Therefore, according to the dynamic similarity principle, two geometrically-similar flow configurations flows, if characterized by the same Reynolds number, meet also dynamic similarity. This principle is very useful and widely leveraged in experiments and computations. In the following sections the non-dimensional form of the Navier-Stokes equations is used and, for the sake of clarity of notation, the super-script "*" is omitted and lower-case letters are employed for nondimensional variables.

2.2 Large-eddy simulation

It is known that, since Osborne Reynolds' experiments, when the Reynolds number, that is the ratio of inertial and viscous forces within a fluid, exceeds a certain value, characteristic of the specific flow configuration, the flow becomes turbulent. Turbulent flows are characterized by three-dimensional, time-dependent and chaotic velocity fields $\boldsymbol{u}(\boldsymbol{x}, t)$. Moreover a large range of time- and length-scales is present: the energy is generally injected into the system at the largest scales (as large as the characteristic length of the flow L), and is transferred across the scales to the smallest eddies (η), where viscous dissipation stops the cascade. The simplest and more accurate

approach to perform a turbulent-flow simulation is the *Direct Numerical Simulation* (DNS), where the Navier-Stokes equations are solved directly, solving all the length- and time-scales. However the range of scales to be resolved grows as the Reynolds number increases, so that the DNS approach becomes inaccessible for high-Reynolds number flows. Indeed, according to Kolmogorov hypotheses for homogeneous isotropic turbulence, the ratio of the largest and the smallest eddy is defined as:

$$\frac{L}{\eta} \propto Re^{3/4}, \tag{2.4}$$

and the ratio of the characteristic times of the eddies is:

$$\frac{T}{t_\eta} \propto Re^{1/2}. \tag{2.5}$$

The grid-spacing δ for a DNS should be as small as the smallest eddy η. Concurrently the computational domain size Δ has to be large enough to fit the largest scale L. The ratio of the computational domain size and the grid spacing, which gives an estimate of the number of gridpoints in one direction, is proportional to $Re^{3/4}$. Hence, the total number of gridpoints for a three-dimensional computation grows as $Re^{9/4}$. Since the time-interval δT used to advance the solution is limited by considerations of numerical stability (CFL condition), the total number of time-steps to span a given time-interval is also proportional to $Re^{3/4}$. Therefore the computational cost for a DNS grows as Re^3 and for this reason DNS applications are usually limited to flows of low or moderate Reynolds number. For modern utility-scale wind turbines, the Reynolds number $Re = \frac{U_\infty D}{\nu}$ is of the order of 10^8, and the consequent computational requirements for DNS clearly becomes far beyond reach even for the most powerful modern supercomputers. For this reason, in the present thesis the *Large Eddy Simulation* (LES) approach is adopted to study the wake behind wind turbines. This type of computational approach solves in a direct way the large-scale turbulent structures, with shape and wavelength depending on the geometry of the problem, that contain

a large part of the energy of the flow. Whereas, smaller-scale turbulent fluctuations, which do not depend on the geometry of the considered problem and have universal character, are represented by simple models. The universality of the small scale is implied in the local isotropy hypothesis of the Kolmogorov theory: if the directional information of the large scales is lost as the energy passes down the cascade, it is reasonable to assume that the statistics of the small-scale motions are in a sense *universal*, hence similar in every high-Reynolds-number turbulent flow. This assumption holds better as far as the Reynolds number is larger, since the scale separation increases. Modeling small-scales in LES allows to increase the size of the grid δ required to simulate the flow, which results into a reduction of the overall number of gridpoints. Therefore, LES allows one to reduce the computational cost with respect to Direct Numerical Simulation (DNS), achieving at the same time a much higher accuracy with respect to the Reynolds-averaged Navier-Stokes equations (RANS), especially for flows where large-scale motions are significant, such as flows over bluff bodies [77]. Large eddy simulations are based onto a low-pass filtering operation of the flow variables $\phi(\boldsymbol{x}, t)$ which removes all the scales lower than a selected cut-off scale so that the filtered variables can be resolved on a relatively coarse grid. The resolved part $\overline{\phi}(\boldsymbol{x}, t)$ of a flow variable is then defined in physical space by the following relation:

$$\overline{\phi}(\boldsymbol{x}, t) = \int_{-\infty}^{+\infty} \int_{-\infty}^{+\infty} \phi(\boldsymbol{\xi}, t') G(\boldsymbol{x} - \boldsymbol{\xi}, t - t') dt' d^3\boldsymbol{\xi}, \tag{2.6}$$

where the filter kernel $G(\boldsymbol{x}, t)$ is associated with the cutoff scales in space and time, $\overline{\Delta}$ and τ_c, respectively. The filter is required to meet some properties such as linearity, conservation of constants and commutation with derivatives in order to be able to manipulate the Navier-Stokes equations after applying a filter[83]. The residual field is defined as:

$$\phi'(\boldsymbol{x}, t) = \phi(\boldsymbol{x}, t) - \overline{\phi}(\boldsymbol{x}, t), \tag{2.7}$$

so that flow-variable field has the following decomposition:

$$\phi(\boldsymbol{x},t) = \overline{\phi}(\boldsymbol{x},t) + \phi'(\boldsymbol{x},t). \tag{2.8}$$

LESs are carried out by solving the governing equations for the filtered non-dimensional velocity, $\overline{\boldsymbol{u}}$, and pressure, $\overline{p}$, derived by applying a filter on the Navier-Stokes equations for incompressible flows (2.2b):

$$\frac{\partial \overline{u}_i}{\partial t} + \frac{\partial \overline{u}_i \overline{u}_j}{\partial x_j} = -\frac{\partial \overline{p}}{\partial x_i} + \frac{1}{Re}\frac{\partial^2 \overline{u}_i}{\partial x_j \partial x_j} - \frac{\partial \tau_{ij}}{\partial x_j} + \overline{F}_i, \tag{2.9a}$$

$$\frac{\partial \overline{u}_i}{\partial x_i} = 0. \tag{2.9b}$$

The filtered Navier-Stokes equations (2.9a) are very similar to the non-filtered equation; the only exception is the presence of sub-grid scale (SGS) stress tensor τ_{ij} in the filtered equations, which represents the interaction between the large resolved and sub-grid unresolved scales and needs to be modeled in order to obtain the closure of the equations.

2.2.1 Sub-grid scale modeling

The SGS stress tensor is defined as:

$$\tau_{ij} = \overline{u_i u_j} - \overline{u}_i \overline{u}_j, \tag{2.10}$$

and its appearance in (2.9a) is due to the nonlinearity of the convective term. It can be decomposed into an isotropic part, $\frac{1}{3}\delta_{ij}\tau_{kk}$ and an anisotropic part, $\tau_{ij}^r = \tau_{ij} - \frac{1}{3}\delta_{ij}\tau_{kk}$. The isotropic part is included in the modified filtered pressure $\overline{p}^* = \overline{p} + \frac{1}{3}\tau_{kk}$, whereas the anisotropic part is usually modeled following a linear eddy-viscosity approach. This approach relates the residual stress to the filtered rate of strain, $\overline{S}_{ij} = \frac{1}{2}(\frac{\partial \overline{U}_i}{\partial x_j} +$

$\frac{\partial \overline{U}_j}{\partial x_i}$), according to the following equation,

$$\tau_{ij}^r = -2\nu_r \overline{S}_{ij}, \tag{2.11}$$

where the proportionality constant ν_r is the eddy viscosity of residual motions. The latter is, in turn, modeled using the Smagorinsky model as:

$$\nu_r = l_s^2 \mathcal{S} = (C_s \Delta)^2 \mathcal{S}, \tag{2.12}$$

where $\mathcal{S}$ is the characteristic filtered rate of strain, defined as $\mathcal{S} \equiv 2\overline{S}_{ij}\overline{S}_{ij}$, and l_s is the *Smagorinsky lenghtscale* which is defined as the product between the *Smagorinsky constant* C_s and the filter width $\overline{\Delta}$. The filter width is defined as the cube root of the local cell volume. The Smagorinsky constant depends upon the type of flow and usually ranges between $C_s = 0.1 - 0.2$. In this work we set $C_s = 0.09$ on the basis of previous works on wind turbines [21].

The model is local and computationally efficient, and it represents well the globally dissipative nature of turbulence. On the other hand it has few important drawback: (i) the Smagorinsky constant is flow-dependent, (ii) the model introduces an excessive SGS dissipation in attached boundary layers, (iii) it allows only the forward energy cascade, being the subgrid dissipation positive by construction, (iv) the SGS tensor principal axes are parallel to those of the strain rate tensor and this is not the case for many types of flows. However, the Smagorinsky model has been widely used in the field on wind turbines, see, for instance, the work of Martinez-Tossas et al[64]. Ciri et al [21, 19] performed LES of the "Blind test 1" [56] and the "Blind test 4" [10] using the Smagorinsky model varying the value of C_s, the Vreman, the WALE and the $\sigma-$ models. They indicated a weak dependence of the wake dynamics on the particular subgrid-scale model, similarly to Sarlak et al[88] results. In the following section, the overline used to denote LES resolved variables will be omitted and they will be indicated by lower-case letters.

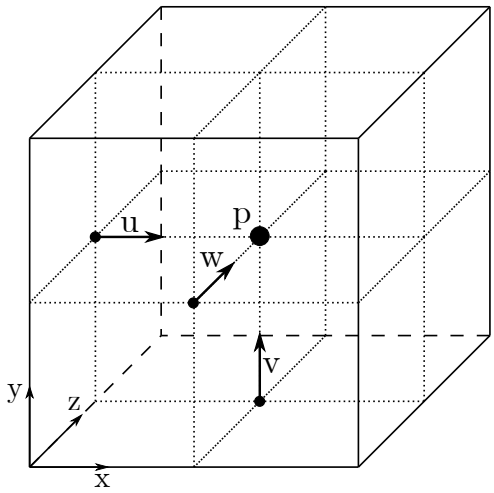

Figure 2.1: Grid cell indicating the flow variables location.

2.3 Numerical method

The governing equations are solved using a central second-order finite-difference scheme on a staggered Cartesian grid, with the velocities defined in the face centers and the pressure in the cell center (Figure 2.1). The staggered arrangement produces compact differential operators and realizes a strong coupling between pressure and velocity, which prevents spurious checkerboard patterns in the pressure distribution. For time-integration an hybrid low-storage third-order-accurate Runge-Kutta scheme originally developed by Wray [109] is employed, in which the nonlinear advective term ares treated explicitly and the linear diffusive terms implicitly . The scheme is said to be low-storage because it requires the same memory storage of a second-order scheme, while being third-order accurate.

The solution is advanced in time from $t = t_n$ to $t = t_{n+1}$ using three substeps. The solution for each substep l is computed according to the following equation:

$$u_i^{l+1} = u_i^l + \rho_l \Delta t \, RHS_i(\boldsymbol{u}^l) + \gamma_l \Delta t \, RHS_i(\boldsymbol{u}^{l-1}) \qquad l = \{0, 1, 2\}, \tag{2.13}$$

where the substep $l = 0$ corresponds to the timestep n ($u_i^{l=0} = u_i^n$), whereas the last substep $l = 2$ corresponds to the timestep $n + 1$ ($u_i^{l=2} = u_i^{n+1}$). The terms $RHS(\boldsymbol{u})$

indicate the right-hand side of the equations and include both linear and nonlinear terms. The coefficients ρ_i and γ_i (2.14) can be obtained comparing the solution after the three substeps with that obtained by a third-order Taylor expansion for u_i^{n+1} centered at the time step n [72].

$$\begin{aligned} \gamma_1 &= \frac{8}{15}, & \gamma_2 &= \frac{5}{12}, & \gamma_3 &= \frac{3}{4}, \\ \rho_1 &= 0, & \rho_2 &= -\frac{17}{60}, & \rho_3 &= -\frac{5}{12}, \\ \alpha_1 &= \frac{8}{15}, & \alpha_2 &= \frac{2}{15}, & \alpha_3 &= \frac{1}{3}. \end{aligned} \tag{2.14}$$

As already mentioned, the linear terms of the Navier-Stokes equations are treated implicitly using a Crank-Nicolson scheme centered at $t_{l+1/2}$ for each substep. The nonlinear and the SGS terms are instead treated explicitly. Therefore the filtered discretized Navier Stokes equations read as follow:

$$\begin{aligned} \frac{u_i^{l+1} - u_i^l}{\Delta t} + \gamma_l \, N_i(\boldsymbol{u}^{\boldsymbol{l}}) + \rho_l \, N_i(\boldsymbol{u}^{l-1}) = -\alpha_l \frac{\partial p^*}{\partial x_i}\bigg|_{l+\frac{1}{2}} + \alpha_l L_{jj}\left(\frac{u_i^l + u_i^{l+1}}{2}\right) + \\ -\gamma_l \frac{\partial \tau_{ij}^r}{\partial x_j}\bigg|_l - \rho_l \frac{\partial \tau_{ij}^r}{\partial x_j}\bigg|_{l-1} + \alpha_l F_i^l, \end{aligned} \tag{2.15}$$

where the term $N(\boldsymbol{u})$ represent the advective nonlinear term, L_{jj} is the Laplacian operator, p^* and τ_{ij}^r are the modified pressure and the deviatoric part of the SGS stress tensor mentioned in section 2.2.1. The coefficient α_l determines the size of the substep $\alpha_l \Delta t$, and since the linear and non-linear terms must be at the same time-step, $\alpha_l = \rho_l + \gamma_l$. The equation (2.15) cannot be solved directly, because the pressure field is known only at time $t = t_l$. In order to overcome this difficulty, the fractional-step method is employed [53]. The method consists in solving the equation (2.15) with the pressure at time $t = t_l$, obtaining a non-solenoidal velocity field $\hat{u}_i$. The latter is then projected onto a solenoidal space enforcing continuity. The pressure is lastly updated at time $t = t_{l+1}$. More precisely, the method develops as follow. Replacing

u_i^{l+1} with $\hat{u}_i$ and introducing the quantity Δu_i, the equation (2.15) becomes:

$$\begin{aligned}\Delta u_i + \frac{\alpha_l \Delta t}{Re} L_{jj}\left(\frac{\Delta u_i}{2}\right) = &- \alpha_l \Delta t \left.\frac{\partial p^*}{\partial x_i}\right|_l - \gamma_l \Delta t\, N_i(\boldsymbol{u}^l) - \rho_l \Delta t\, N_i(\boldsymbol{u}^{l-1}) + \frac{\alpha_l \Delta t}{Re} L_{jj}(u_i^l) + \\ &- \gamma_l \Delta t \left.\frac{\partial \tau_{ij}^r}{\partial x_j}\right|_l - \rho_l \Delta t \left.\frac{\partial \tau_{ij}^r}{\partial x_j}\right|_{l-1} + \alpha_l \Delta t F_i^l,\end{aligned} \tag{2.16}$$

$$\left(\delta_{jj} + \frac{\alpha_l \Delta t}{2Re} L_{jj}\right) \Delta u_i = H_i, \tag{2.17}$$

where H_i denotes all the known terms on the right-hand side. Due to the discretization of spatial derivatives, the matrix on the left-hand side is an $N \times N$ sparse matrix with 7 diagonals, where N is the total number of gridpoints. Solving such a linear system, with standard exact methods, would require a large amount of operations ($\mathcal{O}(N^3)$), and could became unfeasible if a fine resolution is needed, which is often the case when dealing with turbulent flow. For this reason the linear system in (2.17) is solved with the approximate factorization technique as follow:

$$\begin{aligned}\left(\delta_{11} + \frac{\alpha_l \Delta t}{2Re} L_{jj}\right) \Delta u_i^{**} &= H_i, \\ \left(\delta_{22} + \frac{\alpha_l \Delta t}{2Re} L_{jj}\right) \Delta u_i^{*} &= U_i^{**}, \\ \left(\delta_{33} + \frac{\alpha_l \Delta t}{2Re} L_{jj}\right) \Delta u_i &= u_i^{*},\end{aligned} \tag{2.18}$$

where L_{ii} represents the discrete second derivative operator in the i-th direction. These operators are tri-diagonal matrices and can be inverted using the computationally efficient Thomas' algorithm. This approximation of the Laplacian operator is second-order accurate in time (Δt^2). A scalar quantity ϕ (pseudo-pressure) is then introduced in order to project the solution $\hat{u}_i$ onto a solenoidal space:

$$u_i^{l+1} = \hat{u}_i - \Delta t \frac{\partial \phi}{\partial x_i}. \tag{2.19}$$

Taking the divergence of the last equation and enforcing the continuity on $\boldsymbol{U}^{l+1}$, the following Poisson equation is obtained for the scalar ϕ:

$$\frac{\partial}{\partial x_i}\left(\frac{\partial \phi}{\partial x_i}\right) = \frac{1}{\Delta t}\frac{\partial \hat{u}_i}{\partial x_i}. \tag{2.20}$$

Lastly the pressure is updated as follow:

$$p^*|_{l+1} = p^*|_l + \phi - \frac{\Delta t}{2Re} L_{jj}\phi. \tag{2.21}$$

2.3.1 Stability and accuracy of the numerical scheme

The numerical method presented in the above section is known as the Hybrid third-order Runge-Kutta scheme. It is second-order accurate in space and time, therefore the actual advantage of the scheme is not the accuracy, but rather an increased stability. In fact, due to the explicit treatment of the convective terms, the CFL [24] condition applies:

$$C = \frac{\Delta t u_i}{\Delta x_i} \leq C_{max}, \tag{2.22}$$

where C is called the *Courant number*. Tipically the stability of the numerical scheme is guaranteed for $C_{max} = 1$, which limits the distance a fluid particle travel in each time integration to be less or equal to the mesh width. For the three-step Runge-Kutta method, the stability condition is relaxed to:

$$C_{max} \leq \sqrt{3}. \tag{2.23}$$

An additional advantage offered by this method is that $\rho_1 = 0$, which enables you to restart the computation with the latest solution only.

2.4 Turbine blades' modeling

In the present thesis, rotor blades are simulated employing the *Actuator Line Method* (ALM) similar to that proposed by Sørensen & Shen [99]. An external force per unit volume is added in Navier-Stokes equations (the last term in equation (2.9a), $\overline{F}_i$), which models the aerodynamic forces exerted by the turbine blades on the fluid. The forces exerted by the blades on the fluid are computed on the basis of the two-dimensional performance of blade's airfoils at each radius, given by the lift, C_L, and drag, C_D, coefficients. Rotor blades are treated as rotating rigid lines, which are divided into discrete segments, consistently with the computational grid. For each segment, the relative inflow velocity, u_{rel}, and the angle of attack, α, are evaluated, as shown in figure 2.2. Then, knowing the fluid density, ρ, the chord, c, and the twist-angle, ϕ, distributions along the blade radius, it is possible to estimate the lift and drag forces per unit length as follows:

$$F_L = \frac{1}{2}\rho u_{rel}^2 C_L(\alpha) c f, \tag{2.24}$$

$$F_D = \frac{1}{2}\rho u_{rel}^2 C_D(\alpha) c f. \tag{2.25}$$

The coefficient f is a modified Prandtl correction factor [85], which is meant to account for performance degradation due to tip and root vortices. The calculated aerodynamic forces, F_L and F_D, are spread on areas perpendicular to each actuator line with the following Gaussian distribution kernel:

$$\eta = \frac{1}{\epsilon^2 \pi} \exp\left[-\left(\frac{r_\eta}{\epsilon}\right)^2\right], \tag{2.26}$$

where r_η is the radial distance from the actuator line and ϵ is a parameter proportional to the standard deviation of the distribution, which controls forces' spreading. The ALM is an attractive way for simulating rotor blades, because it is computationally less expensive with respect to computing the detailed flow past the blade by a body-

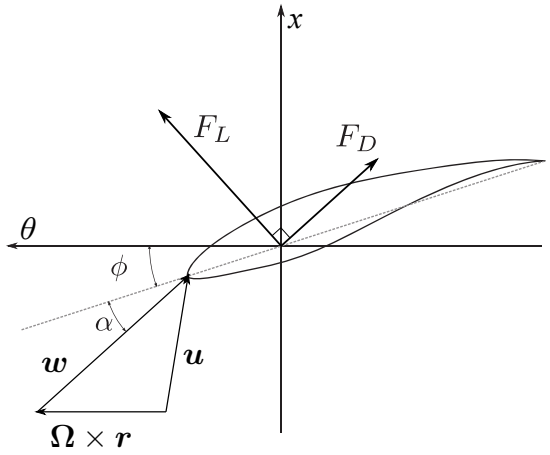

Figure 2.2: Blade cross section: θ and x indicate the tangential and axial directions, respectively, and $\boldsymbol{\Omega} \times \boldsymbol{r}, \boldsymbol{u}, \boldsymbol{w}$ represent the projection in the blade-to-blade plane of the blade speed and of the absolute and relative flow velocity, respectively.

fitted grid, especially when dealing with wind farms, where a large number of turbines have to be simulated. However, it must be considered that the ALM presents some limitations; for example, it cannot reproduce some flow features such as the effect of the blade boundary-layer separation at high angle of attack. A particular care should be taken in the setting of the velocity sampling used to compute angles and forces, since it can significantly affect the overall performance of the turbine [18], thus requiring a thorough validation.

2.5 Immersed boundary method

The tower and nacelle are described using the immersed boundary method (IBM) [25, 72], which avoids the use of a body-fitted grid, reducing the computational cost of the simulations. An approach similar to that proposed by Orlandi & Leonardi [72], has been used. The method involves imposing a zero velocity, $U_i = 0$, in the grid points inside the solid boundary. Then the metrics for the derivatives computation in the Navier-Stokes equations are corrected using the distance between the "immersed" body and points where the velocities are defined (see Figure 2.3). This method has been already applied to a large number of flows, as described in the review article by

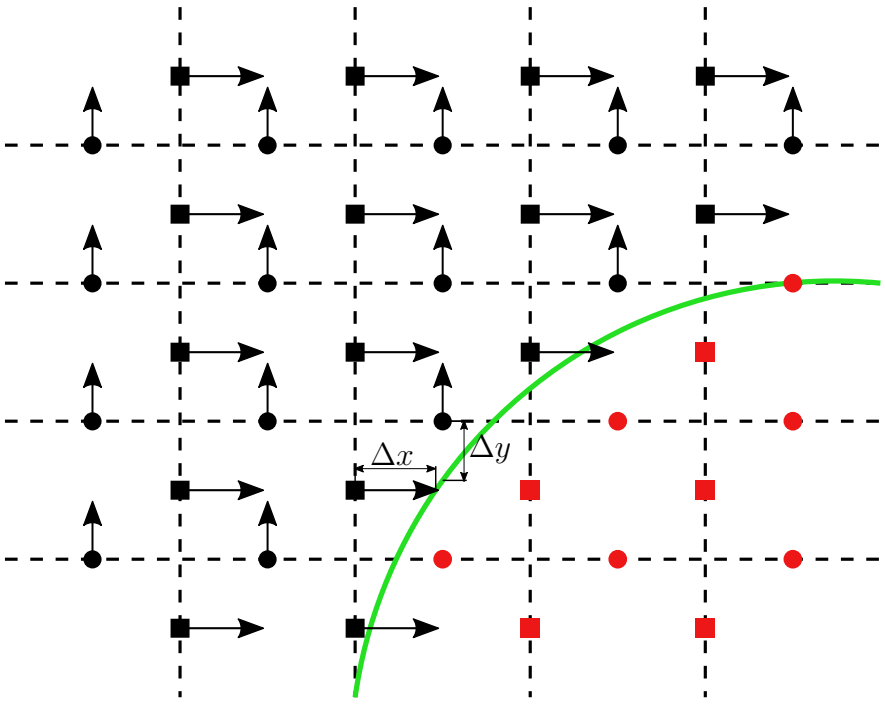

Figure 2.3: Geometrical sketch of the staggered grid around a solid boundary (green curve). The black markers lies within the fluid domain, whereas the red markers lies within the solid domain. The velocity derivatives at the closest points around the boundary are computed using the real distance to the body (Δx and Δy) and not the grid spacing.

Iaccarino & Verzicco [42], and validated in the case of wind turbines by Santoni et al[85]. A comment about the particular choice of the IBM and the ALM for modeling the tower and the blade airfoils, respectively, is in order. The IBM, as implemented in the present paper, is very effective in imposing the impermeability condition and in predicting a realistic value of the drag. However, computing accurately the pressure distribution and the position of the separation point over the surface of streamlined bodies at relatively high Reynolds numbers, as in the present case, requires a high-resolution mesh with the size of the cell much smaller than the chord length. It is, therefore, unfeasible to resolve in a three-dimensional computation the details of the flow using the IBM. Instead, using the ALM, one describes the interaction between the airfoil and the fluid by assigning a lift force (namely, a circulation), which is obtained from lookup tables constructed by accurate simulations of the 2D steady flow around the airfoil. Due to the high mesh resolution one can achieve at the blade tip using a 2D airfoil model, the lift force employed in the ALM is more accurate than that obtained by an "under-resolved" IBM. On the other hand, the IBM is quite accurate when modeling the tower because its diameter is larger and it is possible to have a sufficient number of points inside the body to enforce impermeability and to provide an accurate evaluation of the drag. Instead, using the ALM, a forcing term is added to the Navier-Stokes equations, which represents the time averaged overall force experienced by the body. Such a forcing term is spread (with a Gaussian shape) on a cylindrical region of the mesh which may not resemble the pressure distribution of the "real body". As a consequence, at a generic point, the distributed force of the ALM may not balance the momentum of the incoming flow and the impermeability condition at the body surface cannot be satisfied accurately, as shown in Rocchio et al [81]. Moreover, the ALM applied to the tower would provide a steady symmetric wake. Attempts have been made to impose a force varying in time to provide an oscillation of the tower wake (see Sarlak et al[88]). This approach would however require assuming a priori the shedding frequency, which instead is not needed for the

IBM. For these reasons, the approach used in the present paper combines the two methods. When the dimensions of the solid body are sufficiently larger than the mesh size (6-8 times in each direction), we use the IBM because it is more accurate than the ALM. Otherwise, when the dimensions of the body are too small to be treated with the IBM, the ALM is used to impose the average overall effect of the body on the fluid.

2.6 Proper orthogonal decomposition

Turbulent flows are often characterized by the presence of coherent spatio-temporal structures. The *Proper Orthogonal Decomposition* (POD) is a statistically-based method for extracting these organized structures from time-dependent experimental or numerical (DNS, LES) data.

The method is based on finding a deterministic function $\boldsymbol{\phi}(\boldsymbol{z})$ that is, on average, *an optimal approximation* of a stochastic variable $\boldsymbol{q}(\boldsymbol{z}, \xi)$, where $\boldsymbol{z}$ is a set of independent variables and ξ is a point in the sample space [62].

The space-only variant of the POD [104] applied to fluid flows described by space-time fields $\boldsymbol{q}(\boldsymbol{x}, t)$, considers the flow at each instant as a realization of a stochastic process. Therefore, the basic objective of the method is formalized by finding the spatial mode $\boldsymbol{\phi}(\boldsymbol{x})$ that maximizes the quantity:

$$\lambda = \frac{E\{|\langle \boldsymbol{q}(\boldsymbol{x}, t), \boldsymbol{\phi}(\boldsymbol{x})\rangle|^2\}}{\langle \boldsymbol{\phi}(\boldsymbol{x}), \boldsymbol{\phi}(\boldsymbol{x})\rangle}, \tag{2.27}$$

assuming that the stochastic process belongs to a Hilbert space, $\mathcal{H}$, with inner product $\langle \cdot, \cdot \rangle$ and $E\{\cdot\}$ is the expectation operator. In the case of space-only POD, the expectation operator corresponds to a time-average and the inner product is defined as:

$$\langle \boldsymbol{u}, \boldsymbol{v} \rangle = \int_{\Omega} \boldsymbol{v}^*(\boldsymbol{x}, t) \boldsymbol{W}(\boldsymbol{x}) \boldsymbol{u}(\boldsymbol{x}, t) d\boldsymbol{x}, \tag{2.28}$$

where $\boldsymbol{u}$ and $\boldsymbol{v}$ are two elements in $\mathcal{H}$; Ω is the spatial flow domain; $\boldsymbol{W}(\boldsymbol{x})$ is a positive-definite Hermitian weight tensor; the asterisk superscript indicates the Hermitian transpose. The maximization problem in equation (2.27) can be reformulated, using a standard variational method, such as the Fredholm eigenvalue problem:

$$\int_{\Omega} \boldsymbol{C}(\boldsymbol{x}, \boldsymbol{x}')\boldsymbol{W}(\boldsymbol{x}')\boldsymbol{\phi}(\boldsymbol{x}')d\boldsymbol{x}' = \lambda\boldsymbol{\phi}(\boldsymbol{x}), \tag{2.29}$$

where $\boldsymbol{C}(\boldsymbol{x}, \boldsymbol{x}') = E\{\boldsymbol{q}(\boldsymbol{x}, t)\boldsymbol{q}^*(\boldsymbol{x}', t)\}$ is the two-point spatial correlation tensor. The latter is a compact, self-adjoint, positive operator and $\int_{\Omega} \boldsymbol{C}(\boldsymbol{x}, \boldsymbol{x})d\boldsymbol{x} < \infty$, and, as such, it carries some properties that characterize the eigenvalue problem (2.29):

- Hilbert-Schmidt theory guarantees that there exists a countably infinite set of eigenpairs $\{\lambda_j, \boldsymbol{\phi}_j\}$.
- All the eigenvalues λ_j are real and non-negative so that they can be ordered as $\lambda_1 \geq \lambda_2 \geq \cdots \geq 0$. The largest eigenvalue λ_1 of equation (2.29) with its associated eigenfunction $\boldsymbol{\phi}_1(\boldsymbol{x})$ constitute the mode that maximizes equation (2.27).
- The eigenfunctions are orthonormal, $\langle\boldsymbol{\phi}_j, \boldsymbol{\phi}_k\rangle = \delta_{jk}$, providing a complete basis for each realization of the stochastic process $\boldsymbol{q}(\boldsymbol{x}, t)$.

Consequently, the unsteady flow field can be expanded as a sum of these orthonormal eigenfunctions:

$$\boldsymbol{q}(\boldsymbol{x}, t) = \sum_{j=1}^{\infty} a_j(t)\boldsymbol{\phi}_j(\boldsymbol{x}), \tag{2.30}$$

where the weighting functions are represented by the time coefficients $a_j(t)$, which can be shown to be uncorrelated at zero time-lag:

$$E\{a_j(t)a_k(t)\} = \lambda_j\delta_{jk}. \tag{2.31}$$

In most cases, when considering either experimental or numerical dataset, one deals

with discretized flow fields, both in space and time. In order to perform the space-only POD of these data, a sufficiently large number (M) of instantaneous snapshots of the flow field is required. Usually the three velocity components (u_1, u_2, u_3) are considered so that each snapshot can be stored as a N vector $\mathbf{q}^i$, where $N = 3 \times S$ and S is, in turn, the number of gridpoints. One can build, then, a matrix $\mathbf{Q} \in \mathbb{R}^{N \times M}$ representing all dataset, in which each column is a single snapshot,

$$\mathbf{Q} = \begin{bmatrix} | & | & | & & | \\ \mathbf{q}^1 & \mathbf{q}^2 & \mathbf{q}^3 & \dots & \mathbf{q}^M \\ | & | & | & & | \end{bmatrix}. \tag{2.32}$$

The two-point correlation tensor can be then approximated by the matrix $\mathbf{C} \in \mathbb{R}^{N \times N}$ according to the following equations:

$$\mathbf{C} = \frac{1}{M}\mathbf{Q}\mathbf{Q}^T, \tag{2.33}$$

$$\mathbf{C}_{ij} = \frac{1}{M}\sum_{k=1}^{M} \mathrm{q}_i^k \mathrm{q}_j^k \approx E\{q_i q_j\}. \tag{2.34}$$

The Fredholm eigenvalue problem (2.29) is therefore approximated by the following eigenvalue problem:

$$\mathbf{C}\mathbf{W}\mathbf{\Phi} = \mathbf{\Phi}\mathbf{\Lambda}, \tag{2.35}$$

$$\mathbf{\Phi}^T\mathbf{W}\mathbf{\Phi} = \mathbf{I}, \tag{2.36}$$

where the positive-definite symmetric (Hermitian) matrix $\mathbf{W} \in \mathbb{R}^{N \times N}$ accounts for both the weight $\boldsymbol{W}(\boldsymbol{x})$ and the numerical quadrature on a discrete grid, the columns of $\mathbf{\Phi}$ represent the eigenvectors, i.e. the POD modes, whereas the diagonal entries of $\mathbf{\Lambda}$ are the eigenvalues λ_j.

There are two main alternatives to solve the discrete counterpart of the eigenvalue problem in equation (2.29): i) computing the singular value decomposition (SVD)

of the snapshot matrix $\mathbf{Q}$; 2) using the so-called "snapshot POD"[96], based on the solution of a smaller eigenvalue problem. In the present work the first method is employed and, since the grid used for the discretization of the data is uniform, the weight matrix is considered unitary. Therefore the POD is performed by computing the singular value decomposition of the snapshot matrix $\mathbf{Q}$, divided by the square root of the number of snapshots M,

$$\frac{\mathbf{Q}}{\sqrt{M}} = \mathbf{U}\mathbf{S}\mathbf{V}^T, \tag{2.37}$$

where the left singular vectors $\mathbf{U}$ correspond to the right eigenvectors of $\mathbf{C}$, namely to the POD modes, and $\mathbf{S}$ is the matrix of the singular values, such that $\mathbf{S}\mathbf{S}^T = \mathbf{\Lambda}$. The time coefficients of each POD mode, a_k, are given by the rows of the matrix $\sqrt{M}\mathbf{S}\mathbf{V}^T$. The method has been implemented in Fortran90 using tools from the `LAPACK` libraries.

2.7 Sparsity Promoting Dynamic Mode Decomposition

The dynamic mode decomposition (DMD), introduced in [90], is a data driven technique which allows one to extract relevant flow features, namely the DMD modes, whose dynamics is governed by correspondent eigenvalues. Despite the fact fluid flows dynamics is nonlinear, DMD analysis assumes a linear mapping between successive snapshots. It was shown, in fact, that DMD can be thought as a numerical approximation to Koopman spectral analysis [82, 7]. The DMD has been used in the last decade to study a wide variety of flows [93, 69, 100] and different variants of the original algorithm have been developed, aimed at improving certain aspects as noise sensitivity or memory-efficiency [39, 40]. The variant we employed in the present study has been developed by Jovanovic et al.[51] and is called Sparsity Promoting Dynamic Mode Decomposition (SP-DMD), because it selects a limited number of

modes which optimally reconstruct the flow field time series. This makes more sense than selecting the ones that carry most of the energy at the first time instant, which is the common reference quantity for ranking DMD modes, because they could be strongly damped.

As for the POD, a series of snapshots is collected from a numerical simulation or a physical experiment at a constant sampling frequency,

$$\{\mathbf{q}^0, \mathbf{q}^2, \ldots, \mathbf{q}^M\}. \tag{2.38}$$

Each snapshot $\boldsymbol{q}^i$ can include one or multiple flow variables or even derived observables and has dimension $N = O \times S$ ($\mathbf{q}^i \in \mathbb{C}^N$), where O is the number of observables considered, whereas S represents the number of measurements points. We assume that a linear time-invariant mapping $\boldsymbol{A}$, connects every pair of successive snapshots,

$$\mathbf{q}^{i+1} = \boldsymbol{A}\mathbf{q}^i, \qquad i = \{0, \ldots, M-1\}. \tag{2.39}$$

Using the relation 2.39 we can write:

$$\mathbf{Q}^1 = \boldsymbol{A}\mathbf{Q}^0, \tag{2.40}$$

where $\mathbf{Q}^0$ and $\mathbf{Q}^1$ are:

$$\mathbf{Q}^0 = \left[\mathbf{q}^0\, \mathbf{q}^1\, \ldots\, \mathbf{q}^{M-1}\right] \tag{2.41}$$

$$\mathbf{Q}^1 = \left[\mathbf{q}^1\, \mathbf{q}^2\, \ldots\, \mathbf{q}^{M}\right] \tag{2.42}$$

The linear operator $\boldsymbol{A}$, as suggested by [90], can be projected onto the POD basis $\mathbf{U}$ of the snapshots matrix $\mathbf{Q}^0$, calculated using a Singular Value Decomposition (SVD)

or the snapshot method [96],

$$\mathbf{Q}^0 = \mathbf{U}\mathbf{S}\mathbf{V}^* \tag{2.43}$$

$$\boldsymbol{A} \approx \mathbf{U}\boldsymbol{F}\mathbf{U}^*. \tag{2.44}$$

The matrix $\boldsymbol{F}$ can be therefore obtained by minimizing the Frobenius norm of the difference between $\mathbf{Q}^1$ and $\boldsymbol{A}\mathbf{Q}^0$, with $\boldsymbol{A} = \mathbf{U}\boldsymbol{F}\mathbf{U}^*$ and $\mathbf{Q}^0 = \mathbf{U}\mathbf{S}\mathbf{V}^*$,

$$\min_{\boldsymbol{F}} \ \left\|\mathbf{Q}^1 - \mathbf{U}\boldsymbol{F}\mathbf{S}\mathbf{V}^*\right\|_F^2. \tag{2.45}$$

The optimal solution to 2.45 is:

$$\boldsymbol{F} = \mathbf{U}^*\mathbf{Q}^1\mathbf{V}\mathbf{S}^{-1}. \tag{2.46}$$

This projection ensures a more robust calculation of the low dimensional representation of $\boldsymbol{A}$ algorithm and it allows also to account for a rank-deficiency of the snapshots matrix $\mathbf{Q}^0$, restricting the basis $\mathbf{U}$ to those vectors associated to non-zero singular values, or singular values above a prescribed threshold. The dynamics in the low-dimensional subspace defined by the POD modes $\mathbf{U}$ is governed by

$$\boldsymbol{x}^{i+1} = \boldsymbol{F}\boldsymbol{x}^i. \tag{2.47}$$

Dynamic modes are then extracted by computing the eigendecomposition of the matrix $\boldsymbol{F}$:

$$\boldsymbol{F} = \underbrace{\begin{bmatrix}\boldsymbol{y}_1 & \dots & \boldsymbol{y}_r\end{bmatrix}}_{\boldsymbol{Y}} \underbrace{\begin{bmatrix}\mu_1 & & \\ & \ddots & \\ & & \mu_r\end{bmatrix}}_{\boldsymbol{D}_\mu} \underbrace{\begin{bmatrix}\boldsymbol{z}_1^* \\ \vdots \\ \boldsymbol{z}_r^*\end{bmatrix}}_{\boldsymbol{Z}^*} \tag{2.48}$$

where $\boldsymbol{y}_i$ and $\boldsymbol{z}_1^*$ are the right and left eigenvectors of $\boldsymbol{F}$, which are scaled such that $\boldsymbol{y}_i^*\boldsymbol{y}_i = 1$ and $\boldsymbol{z}_i^*\boldsymbol{y}_j = \delta_{ij}$. Therefore, the solution to (2.47) can be calculated as

follows:

$$\boldsymbol{x}^n = \boldsymbol{Y}\boldsymbol{D}_\mu^n\boldsymbol{Z}^*\boldsymbol{x}^0 = \sum_i^r \boldsymbol{y}_i\mu_i^n\boldsymbol{z}_i^*\boldsymbol{x}^0 = \sum_i^r \boldsymbol{y}_i\mu_i^n\alpha_i, \tag{2.49}$$

where $\alpha_i = \boldsymbol{z}_i^*\boldsymbol{x}^0$ represents the component of the initial condition $\boldsymbol{x}^0$ in the $\boldsymbol{z}_i^*$ direction. The snapshots can be approximated by mapping $\boldsymbol{x}^i$ of the higher dimensional space $\mathbb{C}^N$,

$$\mathbf{q}^n \approx \mathbf{U}\boldsymbol{x}^n = \sum_i^r \mathbf{U}\boldsymbol{y}_i\mu_i^n\alpha_i = \sum_i^r \boldsymbol{\phi}_i\mu_i^n\alpha_i, \tag{2.50}$$

and can be seen, therefore, as a linear combination of the DMD modes $\boldsymbol{\phi}_i = \mathbf{U}\boldsymbol{y}_i$ where α_i is the amplitude of the corresponding DMD mode. The equation (2.50) can be written also in matrix form:

$$\underbrace{\begin{bmatrix}\mathbf{q}^0 & \mathbf{q}^1 & \dots & \mathbf{q}^{M-1}\end{bmatrix}}_{\mathbf{Q}^0} \approx \underbrace{\begin{bmatrix}\boldsymbol{\phi}_1 & \boldsymbol{\phi}_2 & \dots & \boldsymbol{\phi}_r\end{bmatrix}}_{\boldsymbol{\Phi}} \underbrace{\begin{bmatrix}\alpha_1 & & & \\ & \alpha_2 & & \\ & & \ddots & \\ & & & \alpha_r\end{bmatrix}}_{\boldsymbol{D}_\alpha} \underbrace{\begin{bmatrix}1 & \mu_1 & \dots & \mu_1^{M-1} \\ 1 & \mu_2 & \dots & \mu_2^{M-1} \\ \vdots & \vdots & \ddots & \vdots \\ 1 & \mu_r & \dots & \mu_r^{M-1}\end{bmatrix}}_{\boldsymbol{V}_{and}} \tag{2.51}$$

which highlights that the temporal evolution of the dynamic modes is governed by the Vandermonde matrix $\boldsymbol{V}_{and}$. Once the eigendecomposition of (2.48) is computed, the calculation of the amplitudes vector $\alpha = [\alpha_1 \dots \alpha_r]^T$ is performed solving the following optimization problem.

$$\underset{\alpha}{\text{minimize}} \ \left\|\mathbf{Q}^0 - \boldsymbol{\Phi}\boldsymbol{D}_\alpha\boldsymbol{V}_{and}\right\|_F^2 \tag{2.52}$$

The latter, using equation (2.43) and the definition of the matrix $\boldsymbol{\Phi} := \mathbf{U}\boldsymbol{Y}$, can be rewritten as:

$$\underset{\alpha}{\text{minimize}} \ J(\alpha) = \left\|\mathbf{S}\mathbf{V}^* - \boldsymbol{Y}\boldsymbol{D}_\alpha\boldsymbol{V}_{and}\right\|_F^2 \tag{2.53}$$

The superposition of all the DMD modes, weighted by their amplitudes and evolving according to their frequency and growth rate, optimally approximates the data sequence. However, the sparsity promoting DMD aims at finding a low dimensional representation of the snapshots' sequence in order to capture the most relevant dynamic structures. This objective is achieved in two steps: firstly, a sparsity structure is sought, which achieves a user-defined trade-off between the number of modes and the approximation error; then the sparsity structure of the amplitudes' vector is fixed and the optimal values of the non-zero amplitudes is calculated. The first step is tackled by augmenting the objective function $J(\alpha)$ in (2.53) with an additional term, $\mathbf{card}(\alpha)$, the penalizes the number of non-zero elements in the amplitudes' vector α,

$$\underset{\alpha}{\text{minimize}} \;\; J(\alpha) + \gamma\, \mathbf{card}(\alpha). \tag{2.54}$$

In the sparsity promoting optimization problem (2.54), γ is a parameter that influences the sparsity level, with higher values of the parameter promoting sparser solutions. In general, finding a solution to (2.54) amounts to a combinatorial search that quickly becomes intractable for any problem of interest. For this reason a relaxed version of (2.54) is introduced by replacing the cardinality function of α with its ℓ_1-norm,

$$\underset{\alpha}{\text{minimize}} \;\; J(\alpha) + \gamma \sum_{i=1}^{r} |\alpha_i|. \tag{2.55}$$

The sparsity-promoting DMD problem (2.55) is a convex optimization problem, solved using the Alternating Direction Method of Multipliers (ADMM) [51]. Then, the sparsity structure of the amplitudes' vector is fixed and the amplitudes of the non-zero entries are recomputed by solving the following optimization problem:

$$\begin{aligned} &\underset{\alpha}{\text{minimize}} \;\; J(\alpha) \\ &\text{subject to} \;\; E^T \alpha = 0, \end{aligned} \tag{2.56}$$

where the matrix $E \in \mathbb{R}^{r \times m}$ encodes the sparsity structure of the amplitudes' vector α. The columns of E are unitary vectors whose non-zero elements correspond to zero components of α. For example, for $\alpha \in \mathbb{C}^4$ with:

$$\alpha = \begin{bmatrix} \alpha_1 & 0 & \alpha_3 & 0, \end{bmatrix}^T \tag{2.57}$$

the matrix E will be:

$$E = \begin{bmatrix} 0 & 0 \\ 1 & 0 \\ 0 & 0 \\ 0 & 1 \end{bmatrix}. \tag{2.58}$$

The numerical method employed for the solution of the optimization problem (2.56) is the one proposed in [51].

2.8 Linear mean flow analysis

The interpretation of linear analysis of perturbations around a mean flow is not straightforward as that of the linear analysis around steady solutions of the Navier-Stokes equations. Nevertheless, the following argument provides a mathematical and physical interpretation of linear analyses around mean flows. We consider a linearization of the Navier-Stokes equations obtained by plugging a triple decomposition of the flow field following Reynolds & Hussain (1972)[80]

$$\mathbf{u}(\mathbf{x}, t) = \overline{\mathbf{u}} + \widetilde{\mathbf{u}} + \mathbf{u}'. \tag{2.59}$$

The first term of the decomposition $\overline{\mathbf{u}}$ is the meanflow obtained by time averaging the snapshots resolved in time, while the remaining two terms describe the turbulent fluctuations; in particular, within the context of the triple decomposition, using a phase average, we make a distinction between organized wave containing all coherent

time-periodic large-scale motions $\widetilde{\mathbf{u}}$ and the remaining incoherent turbulent fluctuation with zero phase average $\mathbf{u}'$. In particular time average and phase average of a fluctuating quantity $f(\mathbf{x},t)$ are defined as follows:

$$\overline{f(\mathbf{x})} = \lim_{T\to\infty}\int_{t=0}^{t=T} f(\mathbf{x},t)dt \tag{2.60}$$

$$\langle f(\mathbf{x},t)\rangle = \lim_{N\to\infty}\frac{1}{N}\sum_{n=0}^{N} f(\mathbf{x},t+n\tau) \tag{2.61}$$

where τ is the period of the wave. The wave component $\widetilde{f}$ is then defined as $\widetilde{f} = \langle f\rangle - \overline{f}$. Substituting the triple decomposition into the Navier-Stokes equation and taking the time average, the following equation for the mean flow is obtained:

$$\overline{\mathbf{u}}\cdot\boldsymbol{\nabla}\overline{\mathbf{u}} = -\boldsymbol{\nabla}\overline{p} + \boldsymbol{\nabla}\cdot\left(\frac{2}{Re}\overline{\mathbf{S}} - \overline{\widetilde{\mathbf{u}}\widetilde{\mathbf{u}}} - \overline{\mathbf{u}'\mathbf{u}'}\right) \tag{2.62}$$

while the organized wave satisfies the phase-averaged Navier-Stokes equations, with equation (2.62) subtracted:

$$\frac{\partial\widetilde{\mathbf{u}}}{\partial t} + \overline{\mathbf{u}}\cdot\boldsymbol{\nabla}\widetilde{\mathbf{u}} + \widetilde{\mathbf{u}}\cdot\boldsymbol{\nabla}\overline{\mathbf{u}} = -\boldsymbol{\nabla}\widetilde{p} + \boldsymbol{\nabla}\cdot\left(\frac{2}{Re}\widetilde{\mathbf{s}} - \widetilde{\widetilde{\mathbf{u}}\widetilde{\mathbf{u}}} - \widetilde{\mathbf{u}'\mathbf{u}'}\right), \tag{2.63}$$

where $\overline{\mathbf{S}} = \dfrac{\boldsymbol{\nabla}\overline{\mathbf{u}} + \boldsymbol{\nabla}\overline{\mathbf{u}}^T}{2}$ is the mean flow shear stress tensor and $\widetilde{\mathbf{s}}$ the stress tensor of the organized wave. The Reynolds stress tensors $\widetilde{\mathbf{u}'\mathbf{u}'}$ and $\overline{\mathbf{u}'\mathbf{u}'}$ are modeled using the Boussinesq hypothesis. Moreover, we assume that the eddy-viscosity field is not oscillating with the perturbation, $\widetilde{\nu}_t = 0$, and similarly for the turbulent kinetic energy, $\widetilde{k} = 0$. With these assumptions, we obtain (see [102]):

$$\overline{\mathbf{u}'\mathbf{u}'} = \frac{2}{3}\overline{k}\mathbf{I} - 2\overline{\nu}_t\overline{\mathbf{S}} \tag{2.64}$$

$$\widetilde{\mathbf{u}'\mathbf{u}'} = -2\overline{\nu}_t\widetilde{\mathbf{S}} \tag{2.65}$$

This means that the eddy viscosity $\overline{\nu}_t$ can be determined from the averages using (2.64) and used as it is for the oscillating Reynolds stresses (2.65), as usually done in Newtonian eddy models. In particular $\overline{\nu}_t$ is determined by taking the Frobenius product between (2.65) and $\overline{\mathbf{S}}$:

$$\overline{\nu}_t = -\frac{\overline{\mathbf{u}'\mathbf{u}'} : \overline{\mathbf{S}}}{2\overline{\mathbf{S}} : \overline{\mathbf{S}}}. \tag{2.66}$$

Thus, the following phase-averaged equations, governing the dynamics of the organized wave $\widetilde{\boldsymbol{u}}$, are derived:

$$\frac{\partial \widetilde{\mathbf{u}}}{\partial t} = -\overline{\mathbf{u}} \cdot \boldsymbol{\nabla}\widetilde{\mathbf{u}} - \widetilde{\mathbf{u}} \cdot \boldsymbol{\nabla}\overline{\mathbf{u}} = -\boldsymbol{\nabla}\widetilde{p} + \boldsymbol{\nabla} \cdot \left[Re_{eff}^{-1}(\boldsymbol{\nabla}\widetilde{\mathbf{u}} + \boldsymbol{\nabla}\widetilde{\mathbf{u}}^T)\right] + \boldsymbol{f} \tag{2.67a}$$

$$0 = \boldsymbol{\nabla} \cdot \widetilde{\mathbf{u}} \tag{2.67b}$$

where an effective Reynolds number defined as $Re_{eff} = \left(\frac{1}{Re} + \nu_t\right)^{-1}$, is introduced, and $\boldsymbol{f}$ corresponds to the nonlinear remaining terms. The term accounting for diffusion in (2.67) is expanded in order to isolate the molecular and turbulent contributions. Using the property that $\boldsymbol{\nabla}\cdot\left(\boldsymbol{\nabla}\mathbf{u}^T\right) = \boldsymbol{\nabla}(\boldsymbol{\nabla} \cdot \mathbf{u}) = 0$ for incompressibility, the diffusive term in the equation (2.67a) can be rearranged as follow:

$$\begin{aligned} \boldsymbol{\nabla} \cdot \left[Re_{eff}^{-1}(\boldsymbol{\nabla}\mathbf{u} + \boldsymbol{\nabla}\mathbf{u}^T)\right] &= \boldsymbol{\nabla} \cdot \left[\left(\frac{1}{Re} + \nu_t\right)(\boldsymbol{\nabla}\mathbf{u} + \boldsymbol{\nabla}\mathbf{u}^T)\right] = \\ &= \underbrace{\frac{1}{Re}\nabla^2\mathbf{u}}_{1} + \underbrace{\boldsymbol{\nabla} \cdot \left[\nu_t(\boldsymbol{\nabla}\mathbf{u} + \boldsymbol{\nabla}\mathbf{u}^T)\right]}_{2}. \end{aligned} \tag{2.68}$$

The first term on the second line is the classical diffusive term due to molecular diffusivity, and the second term represents, instead, the contribution of turbulent motion to the momentum diffusion.

2.8.1 Bilocal stability analysis

The equations (2.67a) are linear, except for the last term $\boldsymbol{f}$, which contains the remaining nonlinearities. However, if nonlinear terms are considered to be negligible (i.e. $\widetilde{\widetilde{\boldsymbol{u}}\widetilde{\boldsymbol{u}}} \approx 0$), $\boldsymbol{f}$ can be discarded and the phase-averaged equations are linearized. These equations are then projected onto a divergence-free vector space to provide the linear problem

$$\frac{\partial \mathbf{u}}{\partial t} = \boldsymbol{L}\mathbf{u} \tag{2.69}$$

with $\boldsymbol{L}$ the projection of the linearized phase-averaged Navier-Stokes operator onto a solenoidal vector space. The asymptotic time evolution of an infinitesimal perturbation $\boldsymbol{u}$ is then governed by the eigenspectrum of $\boldsymbol{L}$. Due to the very large dimensions of $\boldsymbol{L}$ after discretization of the linearized phase-averaged Navier-Stokes equations, its leading eigenvalues cannot be easily obtained using direct eigenvalue solvers. Thus, for making the eigenvalue problem computationally affordable, we make use of the quasi-parallel hypothesis, for which the mean flow is supposed to be slowly varying in the streamwise direction. This choice is appropriate where the non-parallel effects due to the presence of the rotor are weak. Therefore we carry out our stability (and POD) analysis in cross-sectional planes relatively far from the rotor. Thus, we analyze the fate of infinitesimal perturbations of the two-dimensional base flow $\overline{\mathbf{u}}(y,z)$, which are sinusoidal in the streamwise direction as:

$$\mathbf{q}(\mathbf{x},t) = \hat{\mathbf{q}}(y,z)e^{i(\alpha x - \omega t)} + c.c., \tag{2.70}$$

where $\hat{\mathbf{q}}$ is the Fourier-Laplace transform of $\mathbf{q}(\mathbf{x},t) = (\mathbf{u},p,T)(\mathbf{x},t)$, $c.c.$ is its complex conjugate, ω is the complex pulsation, and α is the (real) wave number in the x direction. Replacing the mean flow profiles and the fluctuation form (2.70) in the linearized system (2.69), the equation to be solved are obtained:

$$i\omega\hat{\mathbf{u}}(y,z) = \mathbf{A}\hat{\mathbf{u}}(y,z) \tag{2.71}$$

where the linear operator $\mathbf{A}$ is a $(N_y \times N_z \times 4) \times (N_y \times N_z \times 4)$ matrix with eigenvectors $\hat{\mathbf{u}}_k(y.z)$ and eigenvalues $\omega = \omega_r + i\omega_i$, ω_r and ω_i being the growth rate and pulsation of the eigenvalue. A spectral collocation method is used for the discretization of the problem in the primitive-variables formulation. In particular a Chebyshev collocation method is employed in the y-direction, where Dirichlet boundary conditions are imposed; whereas a Fourier collocation method is adopted in the $z-$direction, along with periodic boundary conditions.

2.8.2 Optimal forcing analysis

While linear stability analysis allows us to identify the flow structures and frequencies subject to exponential amplification, resolvent analysis establishes which kind of harmonic disturbances are amplified within the flow due to non-modal or quasi-resonance mechanisms, despite the system being asymptotically stable. We consider again the problem in Eq. (2.67), but this time, the term including the non-linearities $\boldsymbol{f}$ is retained and the following input-output linear problem arise:

$$\frac{\partial \mathbf{q}}{\partial t} = \mathbf{L}\mathbf{q} + \mathbf{f} \qquad \text{with} \qquad \mathbf{f} = \hat{\mathbf{f}} e^{i\omega t} \quad \omega \in \mathbb{R}. \tag{2.72}$$

The general solution to this problem consists of the sum of a homogeneous and a particular solution

$$\mathbf{q}(t) = \exp(t\mathbf{L})\mathbf{q_0} + (i\omega\mathbf{I} - \mathbf{L})^{-1}\hat{\mathbf{f}} e^{i\omega t} \tag{2.73}$$

which, assuming that the eigenvalues of $\mathbf{L}$ are confined to the stable half-plane, has the asymptotic long-time response

$$\mathbf{q}(t) = (i\omega\mathbf{I} - \mathbf{L})^{-1}\hat{\mathbf{f}} e^{i\omega t}. \tag{2.74}$$

The quantity $(i\omega\mathbf{I} - \mathbf{L})^{-1}$ is known as the resolvent. We can define the maximum response of the system due to a forcing at a frequency ω as

$$R(\omega) = \max_{\hat{\mathbf{f}}} \frac{\|(i\omega\mathbf{I} - \mathbf{L})^{-1}\hat{\mathbf{f}}\|_E}{\|\hat{\mathbf{f}}\|_E}. \tag{2.75}$$

Restricting ourselves to the space $\mathbb{S}^N$ spanned by the first N eigenfunctions of $\mathbf{L}$,

$$\mathbb{S}^N = \text{span}\{\tilde{\mathbf{q}}_\mathbf{1}, \tilde{\mathbf{q}}_\mathbf{2}, \ldots, \tilde{\mathbf{q}}_\mathbf{N}\}, \tag{2.76}$$

and expanding the vector functions $\mathbf{q}, \mathbf{f} \in \mathbb{S}^N$ in the basis $\{\tilde{\mathbf{q}}_\mathbf{1}, \tilde{\mathbf{q}}_\mathbf{2}, \ldots, \tilde{\mathbf{q}}_\mathbf{N}\}$,

$$\mathbf{q} = \sum_{n=1}^{N} \kappa_n(t)\tilde{\mathbf{q}}_\mathbf{n} \qquad \text{and} \qquad \mathbf{f} = \sum_{n=1}^{N} \kappa_n^f(t)\tilde{\mathbf{q}}_\mathbf{n}, \tag{2.77}$$

we can restate the forced problem in (2.72) as

$$\frac{d\kappa}{dt} = \mathbf{\Lambda}\kappa + \kappa^f(t) \qquad \kappa^f(t) = \kappa^f e^{i\omega t} \tag{2.78}$$

$$\kappa = (i\omega\mathbf{I} - \mathbf{\Lambda})^{-1}\kappa^f \tag{2.79}$$

with

$$\kappa = (\kappa_1, \kappa_2, \ldots, \kappa_N)^T \tag{2.80}$$

$$\kappa^f = (\kappa_1^f, \kappa_2^f, \ldots, \kappa_N^f)^T \tag{2.81}$$

$$\mathbf{\Lambda} = diag\{\lambda_1, \lambda_2, \ldots, \lambda_N\}. \tag{2.82}$$

The operator $\mathbf{\Lambda}$ represents the linear evolution operator $\mathbf{L}$, projected onto the space $\mathbb{S}^N$. The resolvent norm in (2.75) requires the calculation of the energy norm of the state vector $\mathbf{q}$ that can be performed as

$$\|\hat{\mathbf{q}}\|_E = \hat{\mathbf{q}}^*\mathbf{M}\hat{\mathbf{q}} \tag{2.83}$$

$$= \kappa^*\mathbf{V}\mathbf{e}^*\mathbf{M}\mathbf{V}\mathbf{e}\,\kappa \tag{2.84}$$

$$= \kappa^*\mathbf{M}_\mathbf{1}\kappa = \|\kappa\|_E \tag{2.85}$$

where $\mathbf{M}$ is a suitable energy weight matrix, $\mathbf{Ve}$ is a matrix whose columns are N eigenvectors of $\mathbf{L}$, $(\tilde{\mathbf{q}}_\mathbf{1}, \tilde{\mathbf{q}}_\mathbf{2}, \ldots, \tilde{\mathbf{q}}_\mathbf{N})$, and $\mathbf{M_1}$ is the weight energy matrix to be used if we need to calculate energy related to the coefficient vector κ. We also observe that $\mathbf{M_1}$ is both Hermitian and positive definite; we can therefore compute its Cholesky factorization, $\mathbf{M_1} = \mathbf{F_1^* F_1}$, so that

$$\|\kappa\|_E = \kappa^* \mathbf{F_1^* F_1} \kappa = \langle \mathbf{F_1}\kappa, \mathbf{F_1}\kappa \rangle = \|\mathbf{F_1}\kappa\|_2. \tag{2.86}$$

Using the relations in (2.83)-(2.86) and the equation (2.72) we can rewrite the resolvent norm as

$$\begin{aligned}
R &= \max_{\hat{\mathbf{f}}} \frac{\|(i\omega\mathbf{I} - \mathbf{L})^{-1}\hat{\mathbf{f}}\|_E}{\|\hat{\mathbf{f}}\|_E} && (2.87)\\
&= \max_{\kappa_f} \frac{\|\kappa\|_E}{\|\kappa^f\|_E} && (2.88)\\
&= \max_{\kappa_f} \frac{\|\mathbf{F_1}(i\omega\mathbf{I} - \mathbf{\Lambda})^{-1}\kappa^f\|_2}{\|\mathbf{F_1}\kappa^f\|_2} && (2.89)\\
&= \max_{\kappa_f} \frac{\|\mathbf{F_1}(i\omega\mathbf{I} - \mathbf{\Lambda})^{-1}\mathbf{F_1}^{-1}\mathbf{F_1}\kappa^f\|_2}{\|\mathbf{F_1}\kappa^f\|_2} && (2.90)\\
&= \|\mathbf{F_1}(i\omega\mathbf{I} - \mathbf{\Lambda})^{-1}\mathbf{F_1}^{-1}\|_2 = \sigma_1\{\mathbf{F_1}(i\omega\mathbf{I} - \mathbf{\Lambda})^{-1}\mathbf{F_1}^{-1}\} && (2.91)
\end{aligned}$$

with σ_1 denoting the principal singular value.

Most responsive disturbances and responses

By indicating $\mathbf{B} = \mathbf{F_1}(\mathbf{\Lambda} - \omega\mathbf{I})^{-1}\mathbf{F_1}^{-1}$, the singular values decomposition lead to

$$\mathbf{BV} = \mathbf{U\Sigma}, \tag{2.92}$$

where $\mathbf{V}$ and $\mathbf{U}$ are unitary matrices and Σ is a diagonal matrix consisting of singular values ordered in size $\sigma_1 \geq \sigma_2 \geq \cdots \geq \sigma_N$. Concentrating only on the column vectors of $\mathbf{V}$ and $\mathbf{U}$ corresponding to σ_1, which are referred to as the principal right and left

singular vectors respectively, one obtains

$$\mathbf{B}v_1 = \sigma_1 u_1. \tag{2.93}$$

This describes a mapping $\mathbf{B}$ of an input vector v_1 onto an output vector u_1 that is also stretched by a factor of σ_1 equal to the 2-norm of $\mathbf{B}$. Therefore, v_1 describes the most responsive disturbance that will be amplified by a factor of $\sigma_1 = \|\mathbf{B}\|$ and u_1 represents the corresponding response. The optimal forcing and response in spatial coordinates, $\hat{\mathbf{f}}$ and $\hat{\mathbf{q}}$, normalized by their energy norm, are given by

$$\hat{\mathbf{f}} = \mathbf{VeF_1^{-1}F_1}\kappa^f = \mathbf{VeF_1^{-1}}v_1, \tag{2.94a}$$

$$\hat{\mathbf{q}} = \mathbf{VeF_1^{-1}}\sigma_1^{-1}\mathbf{F_1}\kappa = \mathbf{VeF_1^{-1}}u_1. \tag{2.94b}$$

Chapter 3

Analysis of the wake coherent structures using POD

3.1 Introduction

In this chapter the wake produced by a model wind turbine is investigated using proper orthogonal decomposition (POD) of numerical data obtained by large eddy simulations at a diameter-based Reynolds number $Re = 6.3 \times 10^5$. The blades are modeled employing the actuator line method and an immersed boundary method is used to simulate tower and nacelle. Two simulations are performed: one accounts only for the blades effect; the other includes also tower and nacelle. The two simulations are analyzed and compared in terms of mean flow fields and POD modes that mainly characterize the wake dynamics. An analysis of the mean kinetic energy entrainment provided by each POD mode is then performed, which highlights the effect of different flow structures on wake recovery.

3.2 Simulation layout

The simulation layout is based on the experiments performed by Krogstad & Eriksen[56] using a turbine model with a three-bladed rotor of diameter $D = 0.894\ m$ and hub height $y_h = 0.817\,m$. Detailed information about the blade design is given in Krogstad & Eriksen[55].The tower is modeled as a cylinder with diameter equal to one-tenth of the rotor diameter, namely $d_t = 8.94\ cm$. The nacelle is modeled as a capsule with the same diameter of the tower having an axial length of $0.298\ m$ $(0.3D)$. The computational domain has dimensions $12.5D \times 5D \times 3D$ in the streamwise (x), wall-normal (y) and spanwise (z) directions, respectively. The rotor is located at $4D$ from the inlet section and it is centered in the spanwise direction (see Figure 3.1). A uniform velocity profile aligned with the rotor axis with $U_\infty = 10\ m/s$ is imposed at the inlet points, whereas a radiative boundary condition is employed at the outlet points with uniform convection velocity $C = 9\ m/s$ [73]. The no-slip condition is imposed at the bottom wall, whereas free slip is prescribed at the top wall. The lateral boundaries are periodic. Since the working fluid is air at atmospheric pressure and 10°C, the Reynolds number is $Re = 6.3 \times 10^5$. The computational domain is discretized using $2048 \times 512 \times 512$ grid-points in x, y and z directions, respectively. The grid-point distribution is uniform along the streamwise and spanwise directions, whereas it is stretched in the wall-normal direction, with finer (uniform) spacing in the rotor-wake region. The value of the smearing factor ε we use is 0.025 in diameter units. Since $c_R = 0.0905$ and $c_T = 0.0288$ (c_R and c_T being the chord at the root and at the tip, respectively), we have $\left(\frac{\epsilon}{c}\right)_R \approx 0.276$ and $\left(\frac{\epsilon}{c}\right)_T \approx 0.868$, which are a bit beyond the optimal values suggested by Martinez-Tossas et al.[65] $(0.14 < \frac{\epsilon}{c} < 0.25)$. However, decreasing this value would have lead to a grid too heavy for our computational resources. Martinez-Tossas et al. also reported that ε must be larger than $2\Delta x$ to avoid numerical spurious oscillations. In our case we have $\frac{\epsilon}{\Delta} \approx 2.41$, where $\Delta = \sqrt{\Delta x^2 + \Delta y^2 + \Delta z^2}$. Following the experimental data[56], the tip-speed ratio considered in this study is $\lambda = 3$, which implies a constant dimensionless angular

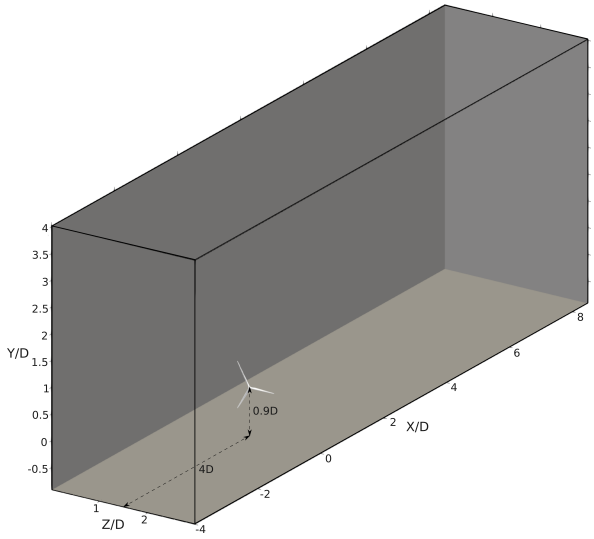

Figure 3.1: Computational domain.

frequency of the rotor:

$$\Omega = \frac{2\lambda U_{ref}}{U_\infty} = 6, \tag{3.1}$$

since we have chosen the inlet velocity U_∞ as reference velocity U_{ref}. The corresponding Strouhal number is $St_r = \Omega/2\pi = 0.9549$. It has to be pointed out that the chosen flow configuration does not reproduce exactly that of the reference case [56]. In particular, we have reduced the blockage effect by removing lateral walls and extending the domain in the wall-normal direction up to five diameters, and we have decreased the dimensions of tower and nacelle, in order to render the setup more similar to that of utility-scale wind turbines.

3.2.1 Mesh convergence

The convergence of the numerical results with respect to the mesh has been assessed with respect to several time-averaged velocity profiles: Figure 3.2 shows the streamwise velocity distributions along the y direction, at 7 locations ($x = \{1, 2, 3, 4, 5, 6, 7\}$) along the midline of the computational domain. Three different computational grids have been employed with $1000 \times 250 \times 250$, $1600 \times 400 \times 400$, and $2048 \times 512 \times 512$

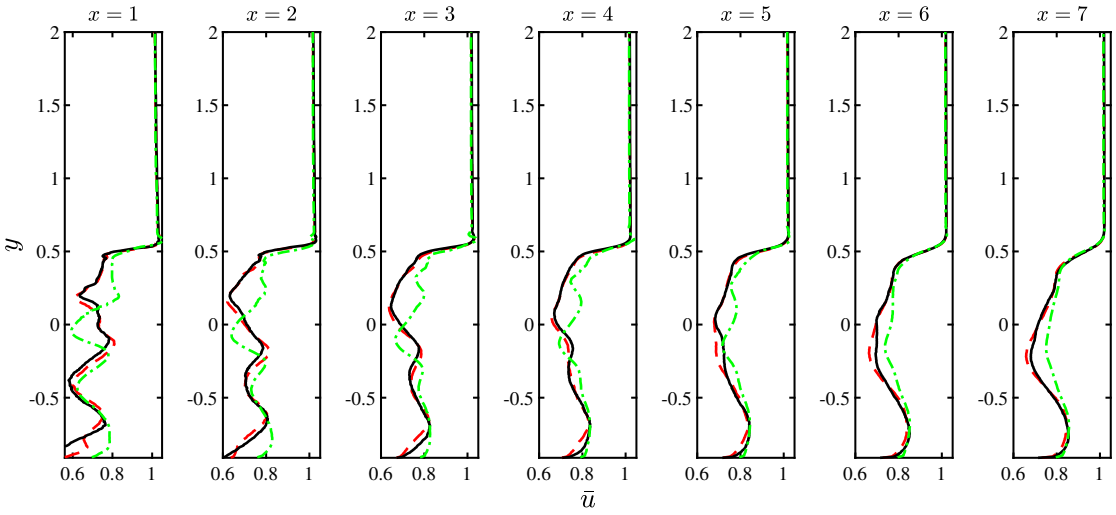

Figure 3.2: Time-averaged streamwise velocity profiles at 7 locations along the midline of the computational domain for three different computational grids: the coarsest grid (-·-·-) consists of $1000 \times 250 \times 250$ gridpoints in x,y and z directions, respectively; the intermediate grid (- - - -) consists of $1600 \times 400 \times 400$ gridpoints; the finest grid (———) consists of $2048 \times 512 \times 512$ gridpoints.

gridpoints in x, y and z directions, respectively. The solutions obtained using the two finest grids, being very close to each other, indicate that grid convergence is achieved. According to the Kolmogorov's hypotheses, the Kolmogorov length scale $\eta \equiv (\nu^3/\epsilon)^{1/4}$, for the present case, is equal to $4.64 \cdot 10^{-5}$ (in rotor diameter units), where the dissipation rate ϵ has been estimated as U_∞^3/D. Therefore, the resulting size of the finest mesh, being approximately equal to 0.006 in each direction, is approximately 130 times the Kolmogorov length scale and, according to existing literature on turbulent flows, lies in the inertial subrange[77]. Moreover, the fine-mesh size is similar to that employed in previous computations and validations using the same numerical approach for solving problems involving wind turbine flows[85, 26].

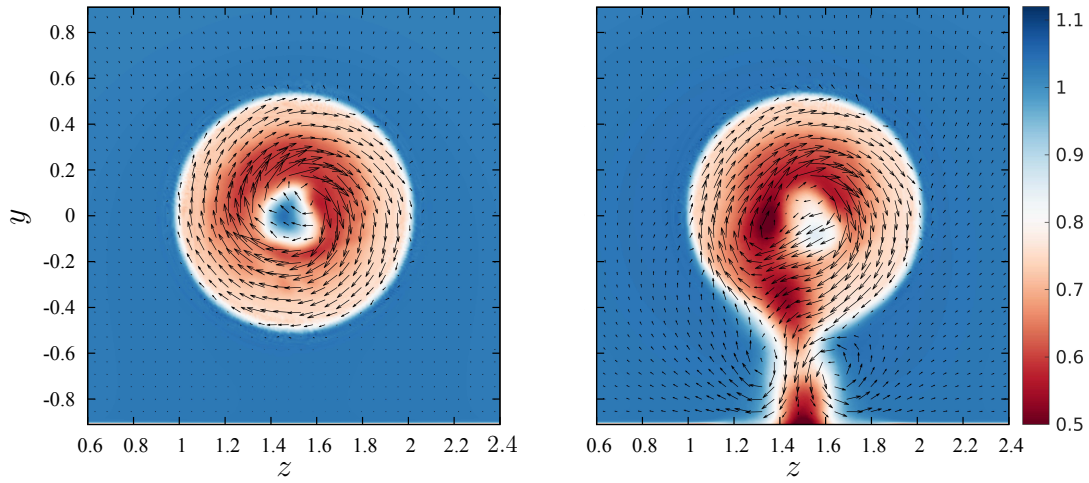

(a) (b)

Figure 3.3: Time-averaged streamwise velocity contours at $x = 1$ for the RO case (a) and the TN case (b).

3.3 Mean flow fields

3.3.1 Time-averaged velocity fields

In the present section the time-averaged flow fields computed for the two flow configurations, the first considering only the rotor and the second taking into account tower and nacelle, are discussed and compared. In the remainder of the paper we will refer to the Rotor-Only case and the Tower and Nacelle flow configurations as the RO and the TN cases, respectively. As shown in figure 3.3, in the $x = 1$ plane, for both configurations, the wake is asymmetric in the vertical (y, z) plane, and the near-wake flow rotates in the direction opposed to that of the rotor. When the nacelle is neglected, an unphysical jet develops at the center of the rotor, whose strength increases with the tip-speed ratio [85]. The presence of the tower and nacelle increases the asymmetry of the flow due to the presence of additional wakes behind the tower and at the center of the wake due to the nacelle. One can clearly observe in figure 3.3(b) that the left part of the near-wake flow has a lower velocity than the right one. This is due to the transport of low-momentum fluid from the wake of the tower,

which is lifted up in the near-wake region. Finally, two asymmetric counter-rotating vortical regions can be observed at the two sides of the wake of the tower, which reveal the presence of a horseshoe vortex system, whose vorticity on the right (respectively, left) part of the domain is enhanced (respectively, inhibited) by the wake rotation. Figure 3.4 provides the streamwise velocity contours in the (x, y) and (x, z) planes. In the RO case (Figure 3.4(a)), the presence of the bottom wall induces a shift of the central high-velocity jet towards the upper part of the wake, as clearly shown in the top frame. Moreover, the jet persists for more than 3 diameters behind the rotor. Further downstream, the velocity gradient is smoothed out by the viscosity and the breakdown of the root vortex. Figure 3.4(b) shows that, in the TN case, the velocity jet at the center of the rotor is reduced in intensity and length, and both the asymmetry of the wake and the recovery of the wake, especially in its upper part, are enhanced. The wake asymmetry in the horizontal (x, z) planes (bottom frames), in the RO case is due to the wall blockage effect. In the TN case, the low-momentum fluid is lifted up from the tower wake and captured by the rotor wake in the near-wake region; then, this velocity deficit is transported downstream following the rotation of the flow around the axis of the turbine. Therefore, due to the rotation of the wake the left part of the near wake in figure 3.4(b) shows a lower streamwise velocity and the wake is inclined with respect to the axial direction. In the far-wake region, the recovery of the wake appears enhanced with respect to the rotor-only case.

A qualitative comparison with the experimental data of Krogstad & Eriksen[56] is provided in Figure 3.5, which shows the mean axial velocity and turbulent kinetic energy profiles along a line at $x = 3$ and $y = 0$ calculated by LES in the presence of tower and nacelle, compared with the corresponding measured profiles. Numerical and experimental data are in reasonable agreement, considering that their layout geometry is not perfectly coincident. In fact, we recall that the exact experimental conditions were reproduced with the same numerical code used here by Santoni et al [85], and the numerical results agreed well with measurements. Whereas, in the

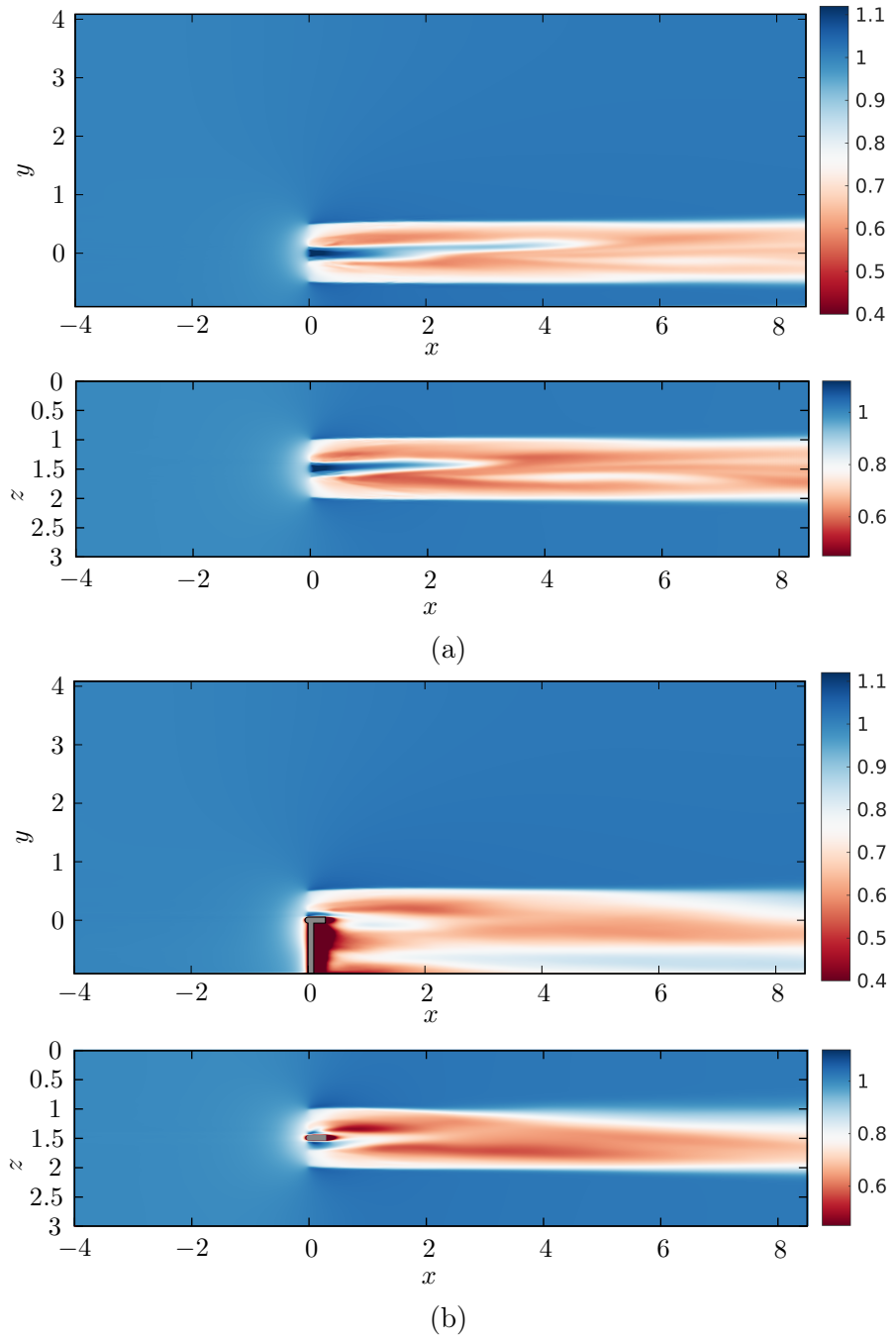

Figure 3.4: Time-averaged streamwise velocity contours in the x-y plane (top frames) and in the x-z plane (bottom frames) passing through the rotor axis for the RO case (a) and the TN case (b).

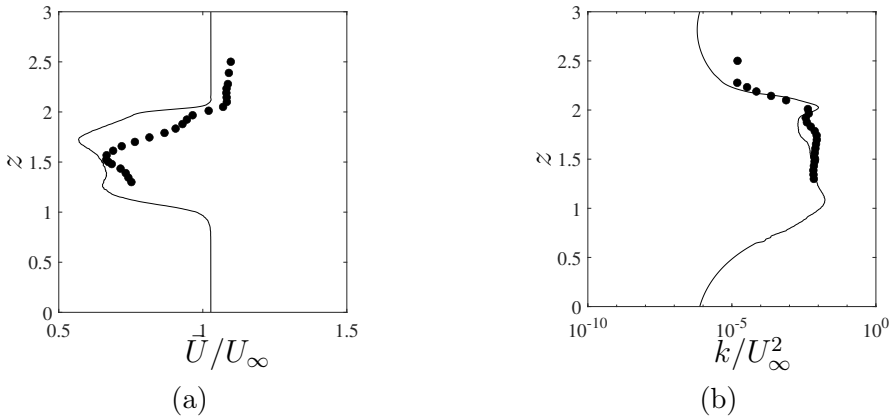

Figure 3.5: Mean streamwise velocity profiles (a) and turbulent kinetic energy profiles (b) at $X/D = 3$ and $Y/D = 0$: experimental results by Krogstad & Eriksen[56] (•) and LES results (——).

present configuration, due to the differences between the numerical and experimental setup (namely, the absence of lateral walls, the increased wall-normal domain and the decreased dimensions of tower and nacelle), the experimental velocity profile shows a lower deficit within the wake and a higher velocity outside it. This depends mainly on the domain cross-sectional area: the blockage ratio of the experiment is quite high (13%), larger than that used in our simulation (5%), and this induces a higher acceleration around the turbine. Instead, the computed turbulent kinetic energy profile is in close agreement with the measured one. Finally, Figure 3.6 shows the averaged velocity distribution in the rotor swept area along the streamwise direction. The averaged velocity drops across the rotor ($x/D = 0$), due to the drag force of the turbine, and further downstream in the wake, the velocity increases (wake recovery). One can observe that the presence of the tower and nacelle (corresponding to the dashed line) on one hand increases the velocity deficit behind the rotor, with respect to the RO case (solid line), and, on the other hand, accelerates the wake recovery by increasing the entrainment of the mean kinetic energy.

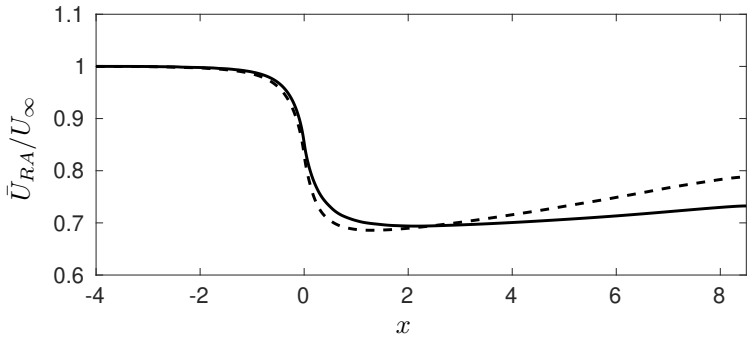

Figure 3.6: Mean streamwise velocity averaged on a disk of radius $R = 0.5$, centered on the rotor axis. Solid line (———) is relative to the rotor-only case, whereas dashed line (- - - -) is relative to the case with tower and nacelle.

3.3.2 Phase-averaged velocity fields

Since the flow under investigation is mainly forced at the frequency corresponding to the rotational speed of the rotor, it is possible to apply a triple decomposition of the turbulent velocity field [80],

$$\boldsymbol{u}(x,y,z,t) = \bar{\boldsymbol{u}}(x,y,z) + \tilde{\boldsymbol{u}}(x,y,z,t_r) + \boldsymbol{u}'(x,y,z,t), \tag{3.2}$$

where $\bar{\boldsymbol{u}}$ is the time-averaged velocity, $\tilde{\boldsymbol{u}}$ is the "coherent" fluctuation with period T dependent on the forcing, $t_r \in [0, T)$ and $\boldsymbol{u}'$ is the "random" fluctuation. We define the coherent fluctuation as $\tilde{\boldsymbol{u}} = \langle \boldsymbol{u} \rangle - \bar{\boldsymbol{u}}$, where $\langle \boldsymbol{u} \rangle$ is the phase-averaged velocity at the Strouhal number of the rotor St_r,

$$\begin{aligned} \langle \boldsymbol{u} \rangle(\mathbf{x}, t_r) &= \frac{1}{N} \sum_{n=0}^{N-1} \boldsymbol{u}(\mathbf{x}, t_r + nT), \\ T &= \frac{1}{St_r}, \end{aligned} \tag{3.3}$$

all the remaining part of the perturbation with respect to the time-average flow being included in the random fluctuation $\boldsymbol{u}'$. In both RO and TN cases, the phase-averaged flow fields provided in figure 3.7 show quite intense coherent vortical structures shed by the turbine, corresponding to tip and root vortices, as expected. For a three-

bladed rotor, the vortical structures oscillate at a characteristic angular frequency, ω_{TV} (where the subscript TV stands for Tip Vortices), equal to three times the rotor angular frequency Ω. Inspecting closely the iso-surfaces of the Q-criterion provided in figure 3.7, one can see that, if tower and nacelle are not taken into account, helical tip vortices are advected downstream, almost undisturbed, up to 6 diameters past the turbine. If, instead, tower and nacelle are included in the simulation, the tip vortices break down earlier, mainly at the bottom and left side of the wake. This is due to the interaction with the vortical structures shed by tower and nacelle, which are advected to the left side of the wake by the rotating flow induced by the blades [85]. Whereas, the tip vortices in the top/right part of the wake are only slightly affected by the presence of tower and nacelle, showing a behaviour similar to the RO case. The analysis of the phase-locked fluctuation $\tilde{\boldsymbol{u}}$ allows us to define a criterion for setting apart the near wake from the far wake, which will be used in the next section for the POD analysis. Usually, the distinction between near and far wake is qualitative: the near wake is the region just behind the rotor where the dynamics of the flow is determined by the geometry and working conditions of the rotor itself, namely, by the number of blades, blade aerodynamics, tip vortices, rotational speed. The far wake is the region beyond the near wake, where the structures linked to the blades' aerodynamics are no longer visible and the flow is dominated by convection and turbulence diffusion[106].

Several criteria have been employed for the discrimination between near and far wake, e.g., the starting location of the wake breakdown [67] or the location where a fully developed Gaussian velocity profile is attained [97]. However, there is not a unified criterion for such a discrimination. The criterion defined and employed in the present work is based on the time-averaged coherent kinetic energy computed as:

$$\bar{\tilde{k}} = \frac{1}{2}\overline{\tilde{\boldsymbol{u}}^2}, \tag{3.4}$$

averaged on the y-z planes at each streamwise location. Figure 3.8 shows the stream-

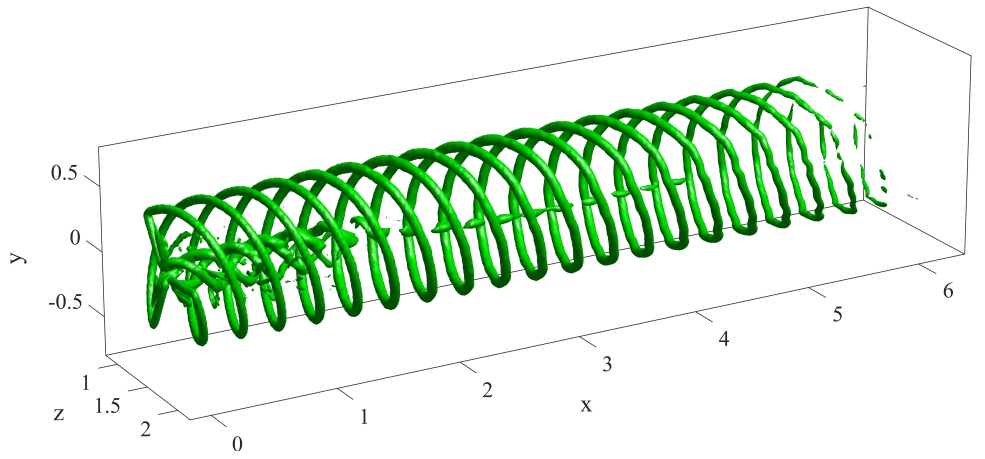

(a)

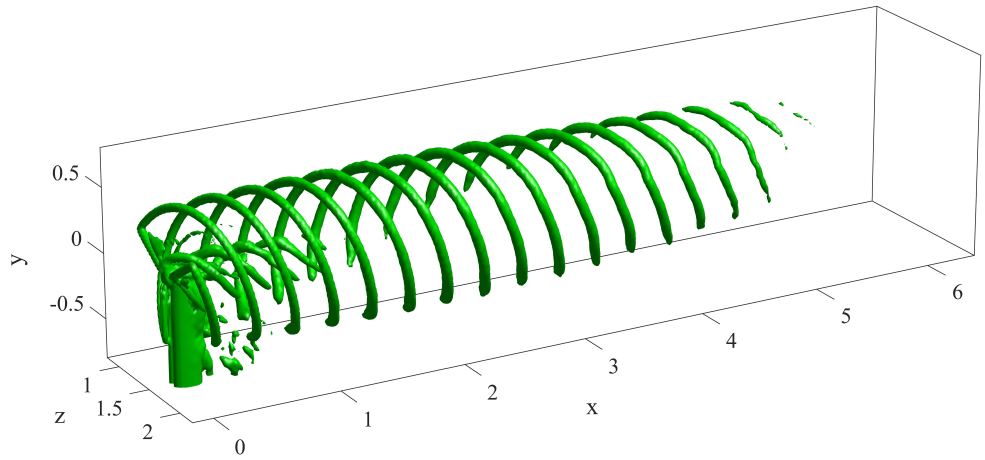

(b)

Figure 3.7: Q-criterion isosurfaces ($Q = 5.1$) of the phase-averaged flow fields for the RO (a) and TN (b) cases.

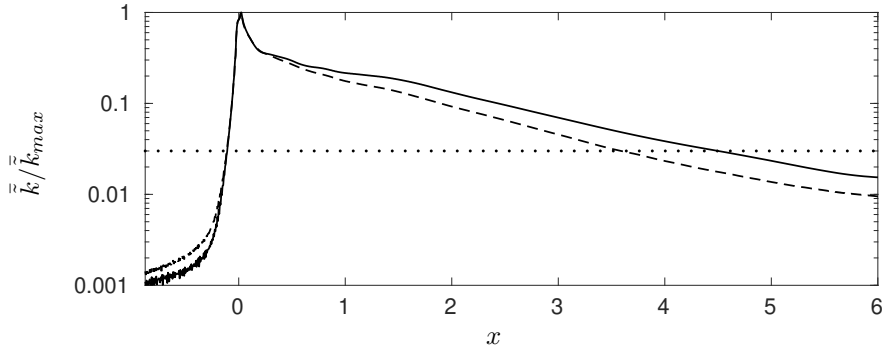

Figure 3.8: Mean kinetic energy of the coherent fluctuation $\tilde{\mathbf{u}}$ averaged in y-z planes for each x location, normalised by its maximum. The solid line (———) refers to the RO case, whereas the dashed line (- - - -) refers to the TN case. The dotted line (·····) at 0.03 is chosen as the threshold to discriminate near-wake and far-wake regions.

wise variation of this quantity (normalized with respect to its maximum value), which decreases in the streamwise direction as the energy passes from coherent to random fluctuations, going from the near to the far wake. The streamwise location at which the value of the coherent averaged kinetic energy drops below 3% of its maximum will be taken hereafter as the threshold between the near- and the far-wake region. Such a criterion, despite being arbitrary by the choice of a threshold value, is closely related to the general definition of near wake, characterized by coherent structures generated by the rotor, in particular by the tip-vortex helices, and has proved to be suitable for separating the two flow regions characterized by a different dynamics.

3.4 Proper Orthogonal Decomposition

The coherent structures developing in the wake of the considered wind turbine are analysed using Proper Orthogonal Decomposition (POD). This technique allows one to decompose the unsteady flow field into a set of orthonormal functions $\boldsymbol{\phi}_j$, providing a complete basis for each realization of the stochastic process $\boldsymbol{q}(\boldsymbol{x}, t)$, which can be expanded as:

$$\boldsymbol{q}(\boldsymbol{x}, t) = \sum_{j=1}^{\infty} a_j(t)\boldsymbol{\phi}_j(\boldsymbol{x}), \tag{3.5}$$

with $a_j(t) = \langle \boldsymbol{q}(\boldsymbol{x}, t), \boldsymbol{\phi}_j(\boldsymbol{x}) \rangle$ being the time coefficients of the expansion. The spatial modes $\boldsymbol{\phi}(\boldsymbol{x})$ are chosen so as to maximize the quantity:

$$\lambda = \frac{E\{|\langle \boldsymbol{q}(\boldsymbol{x}, t), \boldsymbol{\phi}(\boldsymbol{x}) \rangle|^2\}}{\langle \boldsymbol{\phi}(\boldsymbol{x}), \boldsymbol{\phi}(\boldsymbol{x}) \rangle}, \tag{3.6}$$

where $\langle \cdot, \cdot \rangle$ denotes the inner product and $E\{\cdot\}$ is the expectation operator. Further details on the POD method can be found in section 2.6. and convergence of the POD modes has been assessed considering several dataset made by an increasing number of snapshots. Moreover, we have opportunely chosen the frequency threshold for data sampling for it to be sufficiently higher than the frequency of the coherent structures populating the flow. Figure 3.9 shows the Fourier amplitude spectrum of the streamwise velocity signal extracted from a probe located on the rotor axis, at 6 diameters past the turbine. The green and the red lines represent the sampling frequency of the POD snapshots and the related Nyquist frequency, respectively. The Nyquist frequency, being equal to 17.19, is quite high with respect to the recovered flow structures, since it corresponds to the frequency of the 6th harmonic of the tip vortices. Moreover, one can observe that the amplitude decreases exponentially after the red line, meaning that energy-containing structures are those with lower frequencies. Therefore, we believe that further increasing the sampling rate would not change the energy-containing coherent structures we presented in the results.

3.4.1 Rotor-only case

Proper Orthogonal Decomposition of the flow field in the rotor-only (RO) configuration has been carried out over a dataset made of $M = 2575$ snapshots, after validation of the convergence of the POD modes with respect to the number of snapshots. Since the Δt between the different snapshots allows for a 10° rotation of the rotor, 36 snapshots correspond to a complete rotation of the rotor. Therefore, the dataset spans about 71 revolutions. Two different sub-domains have been considered,

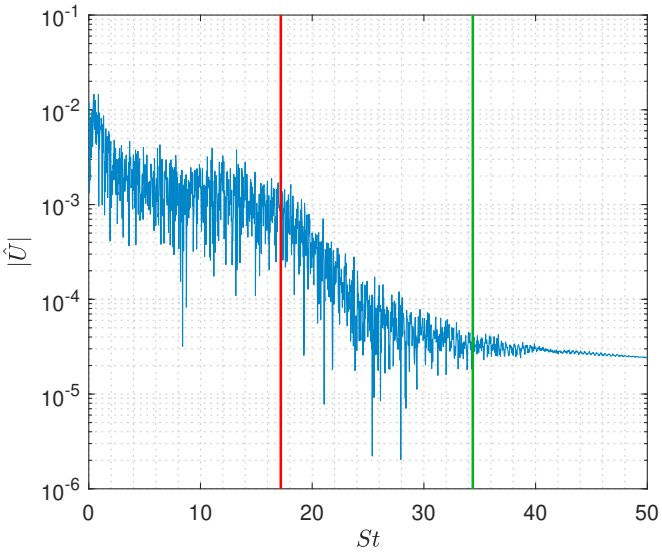

Figure 3.9: Amplitude spectrum of the streamwise velocity signal $U(t)$ from a probe located on the rotor axis at 6 diameters past the wind turbine. The green and red line represent the sampling frequency of the POD snapshots and the related Nyquist frequency, respectively.

namely a near-wake (NW) domain and a far-wake (FW) domain. According to the criterion established in the previous section for the near/far wake discrimination, the resulting sub-domain extents are $[0\ 4.5] \times [-0.8\ 0.9] \times [0.3\ 2.7]$ for the near wake, and $[4.5\ 8.4] \times [-0.8\ 0.9] \times [0.3\ 2.7]$ for the far wake, in x,y and z directions, respectively. The results of the analyses are nonetheless robust with respect to the choice of the threshold for determining the near- and far-wake regions. In both regions, the velocities have been down-sampled with a 1:5 ratio with respect to the computational grid. The POD method ranks the eigenvectors with respect to their energy content, as shown in figure 3.10. The top frames of this figure show the flow energy captured by each of the main POD modes expressed as a percentage of the reconstructed total turbulent kinetic energy, computed as $\mathcal{E} = \sum_{i=1}^{M} \lambda_k$, in the near- (left) and far-wake (right) region (the bottom frames showing the same quantities for the TN case). Although the snapshots' matrix is full-rank, the POD modes with k greater than those shown in the figure have a slowly decaying energy and an increasingly small-scale disorganized structure, being therefore of little interest for the present study. In all

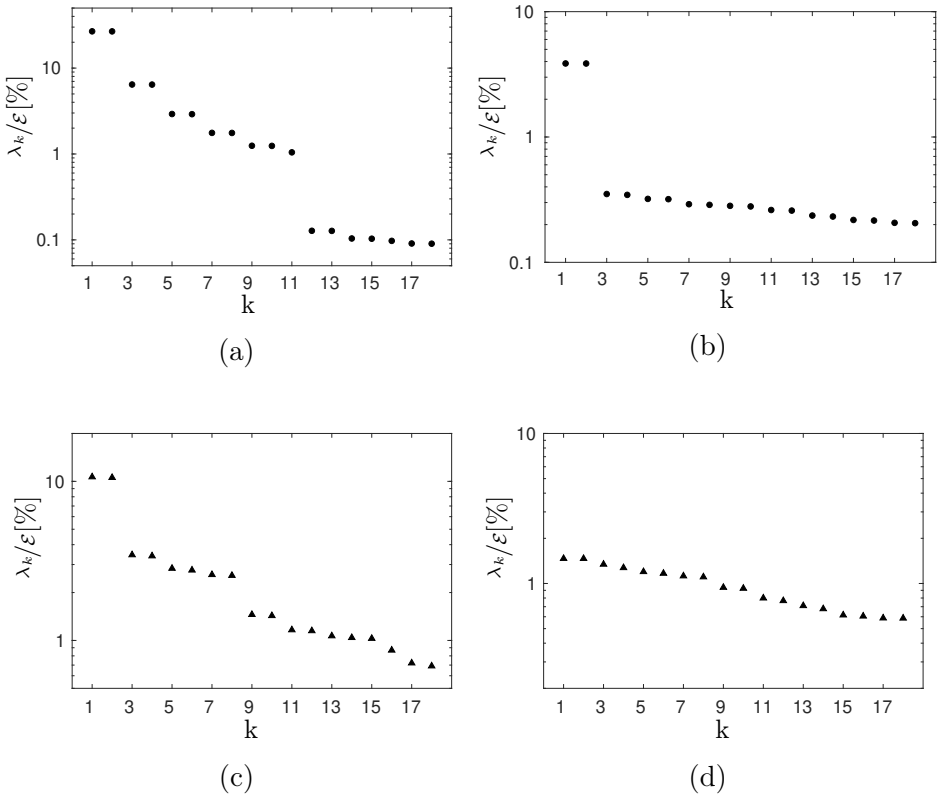

Figure 3.10: Energy of the main POD modes, expressed as a percentage of the total turbulent kinetic energy $\mathcal{E} = \sum_{i=1}^{M} \lambda_k$, for the RO (top) and TN (bottom) configuration in the near wake (left) and in the far wake (right).

cases, the 0^{th} POD modes (see the left columns of table 3.1), are omitted since they simply provide the time average of the instantaneous flow fields.

Near wake

The most energetic POD modes from 1 to 12 are paired as described in table 3.1, since their associated eigenvalues, λ_i, are very close each-other and their time coefficients, $a_i(t)$, have almost identical frequency spectra, as shown in figure 3.11(a). The first pair of modes, labeled RONW1 and containing about 25% of the total energy, represents the root and tip vortices shed by the blades, as shown in figure 3.12 by the combination of the first three POD modes providing the coherent tip- and root-vortex system

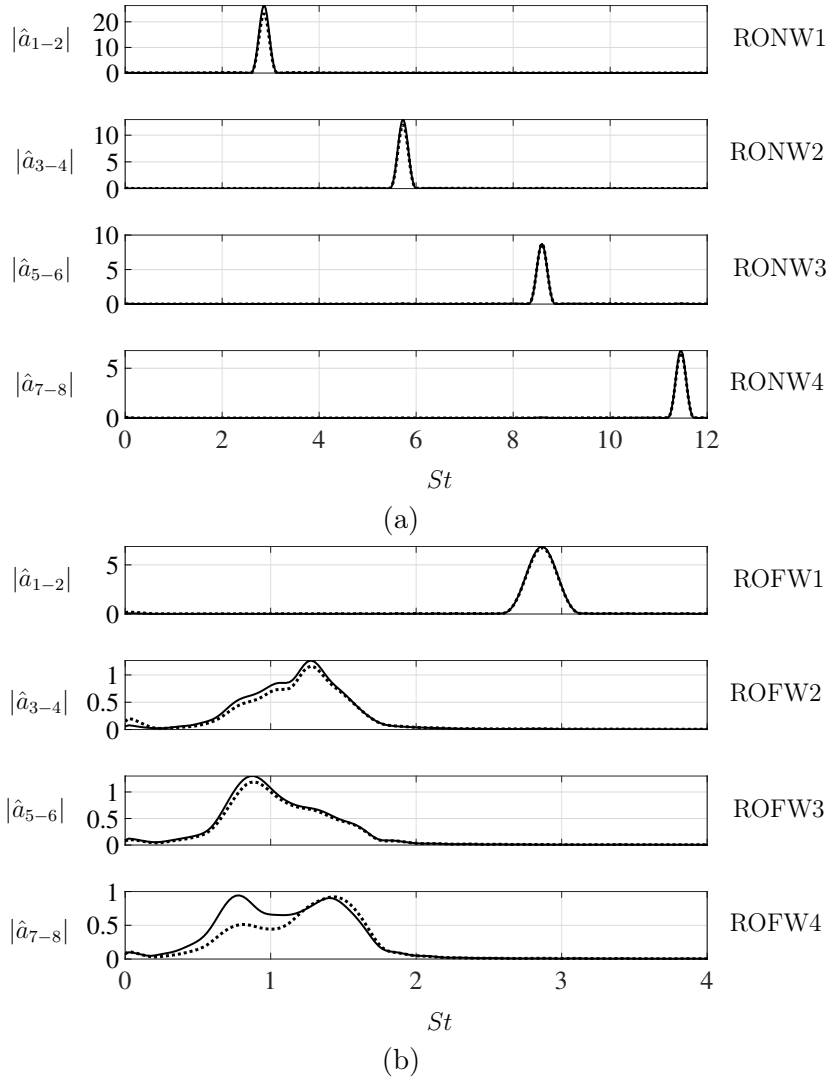

Figure 3.11: Amplitude spectra of time coefficients associated to the first 4 POD pairs for the RO case in the near wake (a) and in the far wake (b). Solid lines (———) represent the first mode of each pair, whereas dotted lines (·····) represent the second mode.

	Near Wake			Far Wake		
	Pair	POD modes	St_l	Pair	POD modes	St_l
Rotor -Only Case	RONW0	0	0	ROFW0	0	0
	RONW1	1-2	2.865	ROFW1	1-2	2.865
	RONW2	3-4	5.73	ROFW2	3-4	1.277
	RONW3	5-6	8.59	ROFW3	5-6	0.883
	RONW4	7-8	11.46	ROFW4	7-8	0.78 - 1.41
Tower and Nacelle Case	TNNW0	0	0	TNFW0	0	0
	TNNW1	1-2	2.865	TNFW1	1-2	0.883
	TNNW2	3-4	1.891	TNFW2	3-4	0.246
	TNNW3	5-6	1.03	TNFW3	5-6	0.662
	TNNW4	7-8	5.73	TNFW4	7-8	0.451
	TNNW5	9-10	1.43 - 0.93	TNFW5	9-10	0.491

Table 3.1: Mode number of the RO (top) and TN (Bottom) cases, according to figure 3.10 and leading Strouhal number St_l of the most energetic POD pairs.

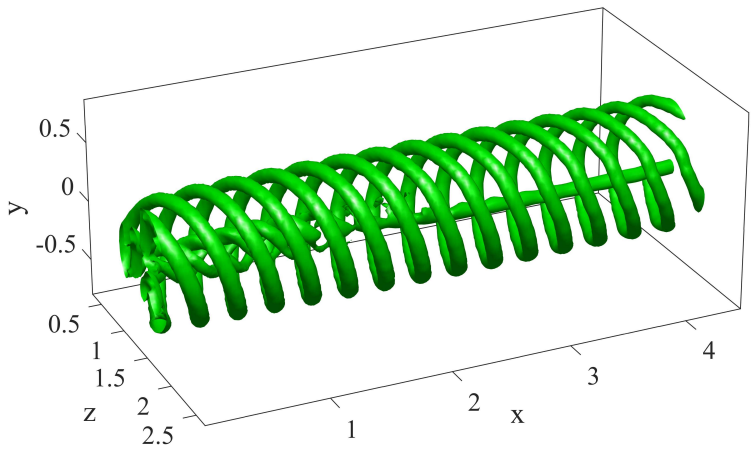

Figure 3.12: Q-criterion isosurface of the velocity field obtained by summing the first three POD modes (RONW0 plus RONW1) multiplied by the corresponding time coefficients at $t = 0$.

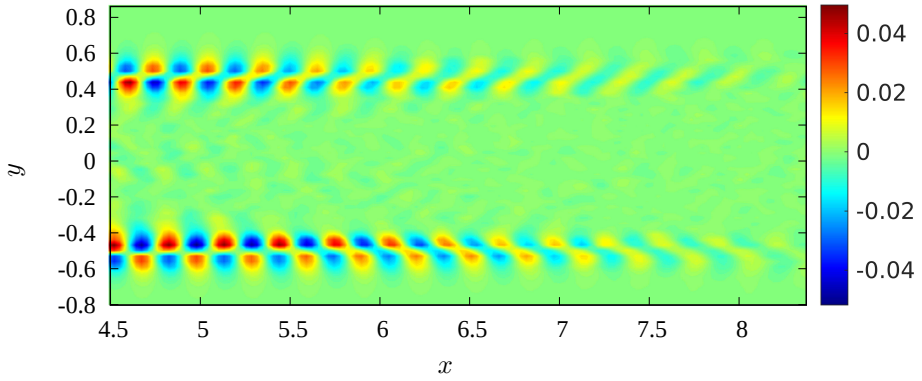

Figure 3.13: Streamwise velocity contours of the ROFW1 pair at $t = 0$ in the x-y plane at $z = 1.5$.

together with the central jet due to the absence of the nacelle. The frequency spectra of the time coefficients $a_{2-3}(t)$ related to these modes show, indeed, a single peak at $St_{TV} = \omega_{TV}/2\pi \approx 2.865$, which is three times the Strouhal number correspondent to the rotor angular frequency St_r. This particular value of the Strouhal number is related to the pitch λ_x of the tip and root vortices by the convection velocity of the vortex system. By measuring the pitch λ_x leading to the streamwise wavenumbers $\alpha_{tip} = 2\pi/\lambda_x \approx 20.92$ and $\alpha_{root} \approx 20.36$, the convection velocities of the tip and root vortices can be estimated as $C_{tip} = 2\pi St_l/\alpha_{tip} \approx 0.861$ and $C_{root} \approx 0.88$, where the slightly larger convection velocity estimated for the root vortices is probably due to the presence of a jet at the centre of the rotor. The successive mode pairs characterizing the near-wake region, are simply harmonics of the first pair. Figure 3.11(a) provides the frequency spectra of pairs RONW2/3/4, all of them showing a single peak at values of the Strouhal number multiple of St_{TV}.

Far wake

In the far-wake region, the first three POD modes are similar to the first three modes found in the near wake. Figure 3.13 provides the streamwise velocity contours of the pair ROFW1 (where both modes, taken at $t = 0$, have been summed up for the sake

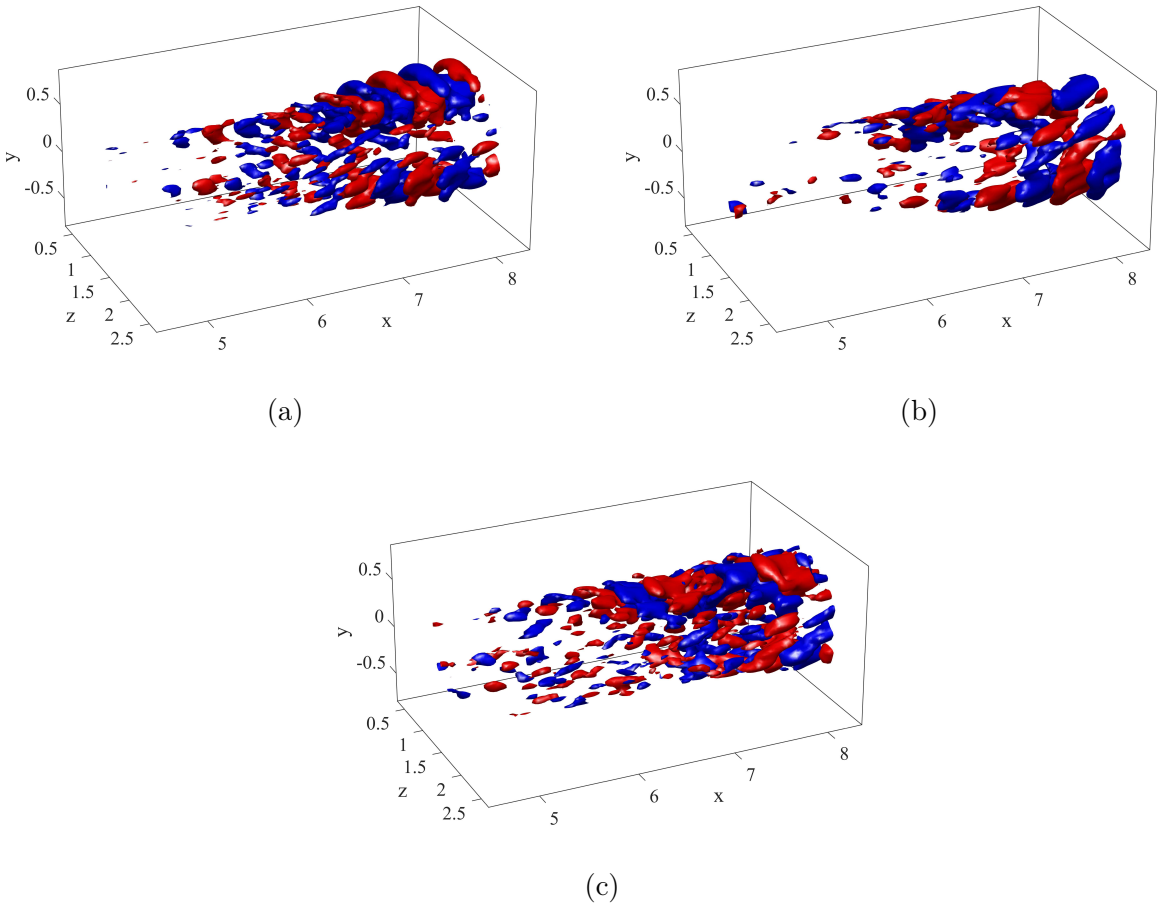

Figure 3.14: Streamwise velocity iso-surfaces of the ROFW2 (a), ROFW3 (b), ROFW4 (c) pairs at $t = 0$ (red for positive, blue for negative values).

of visualization) in the x-y plane containing the rotor axis, showing a clear set of tip vortices fading out towards the end of the domain. The successive pairs of modes, instead, capture the convective instabilities developing in the far wake and have lower frequencies both in space and time, as shown by the spectra in figure 3.11(b). Figure 3.14 provides the streamwise velocity contours of pairs ROFW2/3/4, showing that they are mostly located in the tip-vortex region, and to a lesser extent, in the core of the wake, where radial gradients due to the central jet are present. Looking at the flow field obtained by the combination of the first five POD modes, one can observe a vortex-pairing mechanism (see figure 3.15 at $x > 6$), recalling the mutual inductance

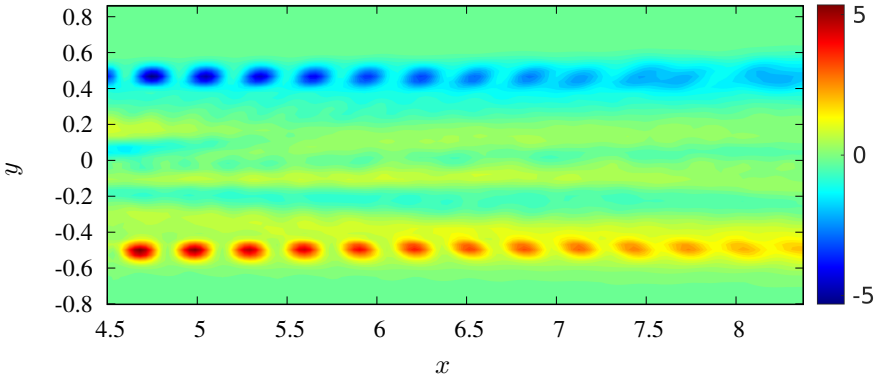

Figure 3.15: Spanwise vorticity contours in the x-y plane at $z = 1.5$ of the flow field obtained by combining the first 5 POD modes of the RO case multiplied by the corresponding time coefficients at $t = 0$.

instability phenomenon investigated extensively by Ivanell et al [49]. These authors studied this phenomenon perturbing a steady (low-Re) wake of a wind turbine using low-amplitude excitations located in the neighbourhood of the blade tips. They found that the most amplified perturbations are those inducing an out-of-phase displacement of two consecutive vortex spirals. It has been also shown by Sarmast et al [89] that the streamwise frequency of the waves responsible for this instability is about half the tip vortices' frequency. Here, the ROFW2 modes have a peak Strouhal number about equal to half the tip-vortex one; assuming that these POD pairs are characterised by the same phase velocity, the relation between temporal frequencies is valid also for the streamwise spatial frequencies. Therefore, the ROFW2 pair produces an out-of-phase displacement of two consecutive tip vortices, leading to vortex pairing. It will be shown in section 3.5 that these modes provide an important contribution to the recovery of the wake through mean kinetic energy entrainment, even though they are about 10 times less energetic than tip vortices, as shown in figure 3.10(b).

3.4.2 Tower and Nacelle case

In this section we discuss the POD results in the flow configuration including the tower and nacelle. The total number of snapshots considered for the POD is $M = 2361$, stored each 10° rotation for about 65 revolutions. Near- and far-wake subdomains have been considered. According to the criterion described in section 3.3.2, the near-wake domain extent is $[0\ 3.5] \times [-0.8\ 0.9] \times [0.3\ 2.7]$ and the far-wake domain extent is $[3.5\ 8.4] \times [-0.8\ 0.9] \times [0.3\ 2.7]$ in x, y and z directions, respectively. Notice that the near-wake region is shorter than in the RO case. The velocity components, as in the RO configuration, have been downsampled with a ratio 1:5 with respect to the computational grid. The energy of the main POD modes obtained for the TN configuration in the near wake and in the far wake is provided in the bottom row of figure 3.10. The 0^{th} mode is omitted being the time-average of the flow, whereas the successive unsteady modes up to the 10^{th} are combined in pairs, according to Table 3.1. As in the RO case, mode pairing is revealed by the frequency analyses of the corresponding time coefficients, which are provided in figure 3.16.

Near wake

The most-energetic POD modes in the near wake for the configuration including tower and nacelle allow us to uncover several important features of the flow. The TNNW1 pair is related to tip and root vortices, as shown in figure 3.17(a), and oscillates at the characteristic Strouhal number of the tip vortices St_{TV}, as in the RO case. However, in the present case, these coherent vortical structures are detected by POD mainly on one side of the wake, corresponding to the region where the phase-averaged velocity gradient field discussed in section 3.3.2 is stronger. Notice that in this case the presence of the nacelle induces a reduction of the convection velocity of the root vortices ($C_{root} \approx 0.67$), which translates into a smaller pitch of the root vortices.

The TNNW2 pair provided in figure 3.17(b) is related to the von Karman vortices shed by the tower. It is characterised by a Strouhal number $St \approx 1.891$, which, once

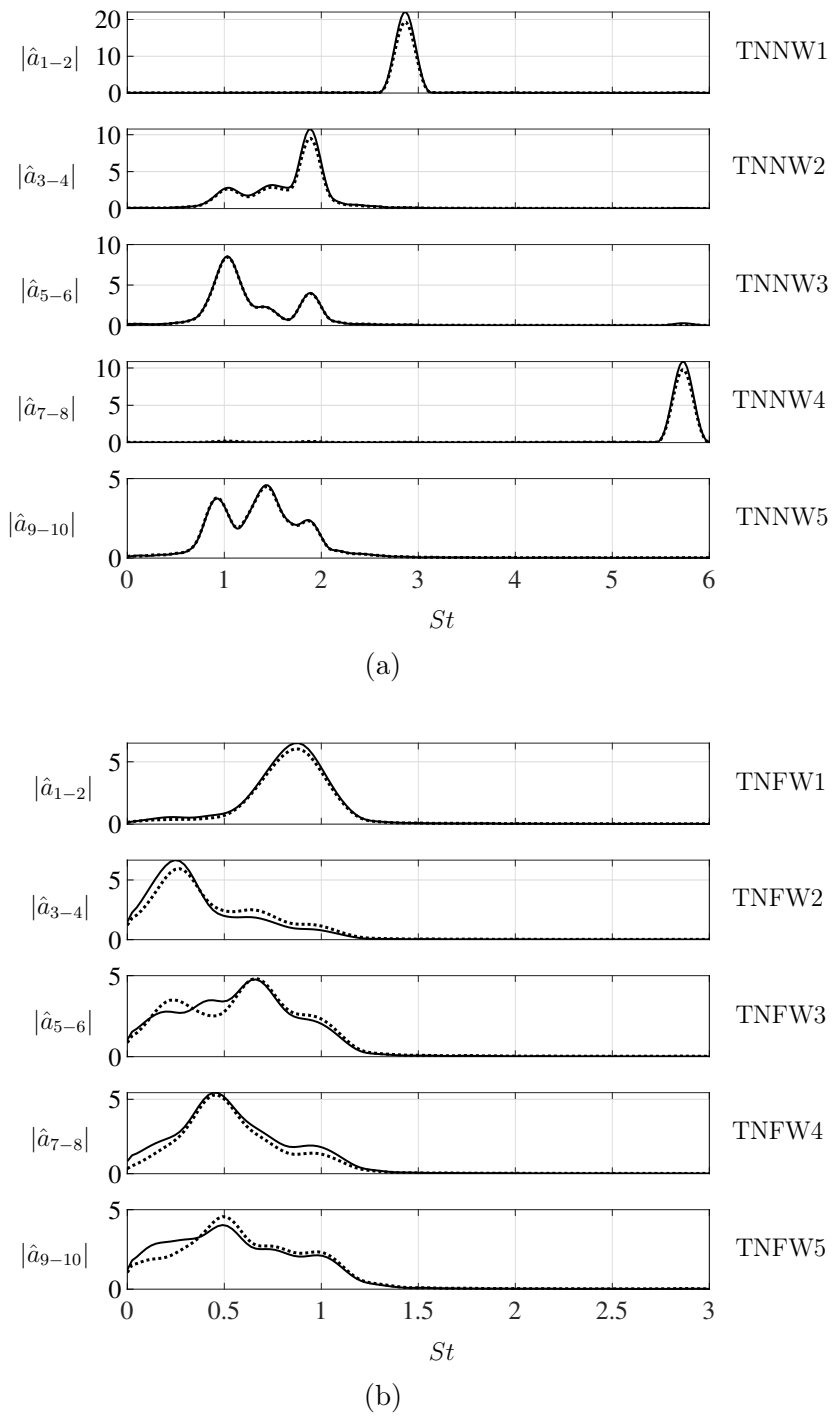

Figure 3.16: Amplitude spectra of time coefficients associated to the first 5 POD pairs for the TN case in the near wake (a) and in the far wake (b). Solid lines (———) represent the first mode of each pair, whereas dotted lines (·····) represent the second mode.

rescaled with respect to the tower diameter d_t ($St^* = St\,(d_t/D) \approx 0.19$), is in close agreement with the value expected for vortices shed by a cylinder of diameter d_t at Reynolds number $Re_t = Re\,(d_t/D) = 6.3 \cdot 10^4$. As shown by the 3D visualization in figure 3.18 (a), these vortices are concentrated behind the lower part of the tower, where the velocity hitting the tower is substantially undisturbed and aligned with the streamwise direction. As expected in the case of the vortex shedding behind a cylinder, these vortices propagate downstream in the streamwise direction, but extending in the spanwise one, although not in a homogeneous way due to the intrinsic asymmetry of the mean flow.

The TNNW3 pair provided in figure 3.17(c) can be ascribed as well to the shedding of a von Karman-like vortex street behind the tower. As shown in figure 3.18 (b), this vortex street occupies also the upper part of the tower, where the velocity investing the tower is influenced by rotor-blades' passage. As already discussed in section 3.3, the mean velocity behind the rotor has a lower magnitude than the undisturbed one, and is characterized by a swirling motion opposite to the rotor direction of rotation. This makes the TNNW3 pair oscillate at a lower Strouhal number ($St \approx 1.03$) and propagate in a direction which is slightly inclined with respect to the axial direction towards the left side of the domain. Approximately 1 to 2 diameters behind the rotor, the vortex street reaches the edge of the wake and interacts with the tip vortices, causing the breakdown of the spirals and producing a large-scale perturbation which can be observed in figure 3.19, where the solid contours of the TNNW3 modes are superimposed on the shaded contours of the TNNW1 pair.

The TNNW4 pair is a harmonic of the first pair, as can be immediately deduced comparing figures 3.17(a) and 3.17(d). Frequency analysis of the relative time coefficients highlights a single peak at $St \approx 5.73$, which is two times the Strouhal number of the tip vortices, St_{TV}. The TNNW5 pair appears less coherent with respect to the first four pairs and it is similar, both in shape and in spectral distribution, to the TNNW3 pair, therefore, it can be related to the same physical mechanism. Despite having a

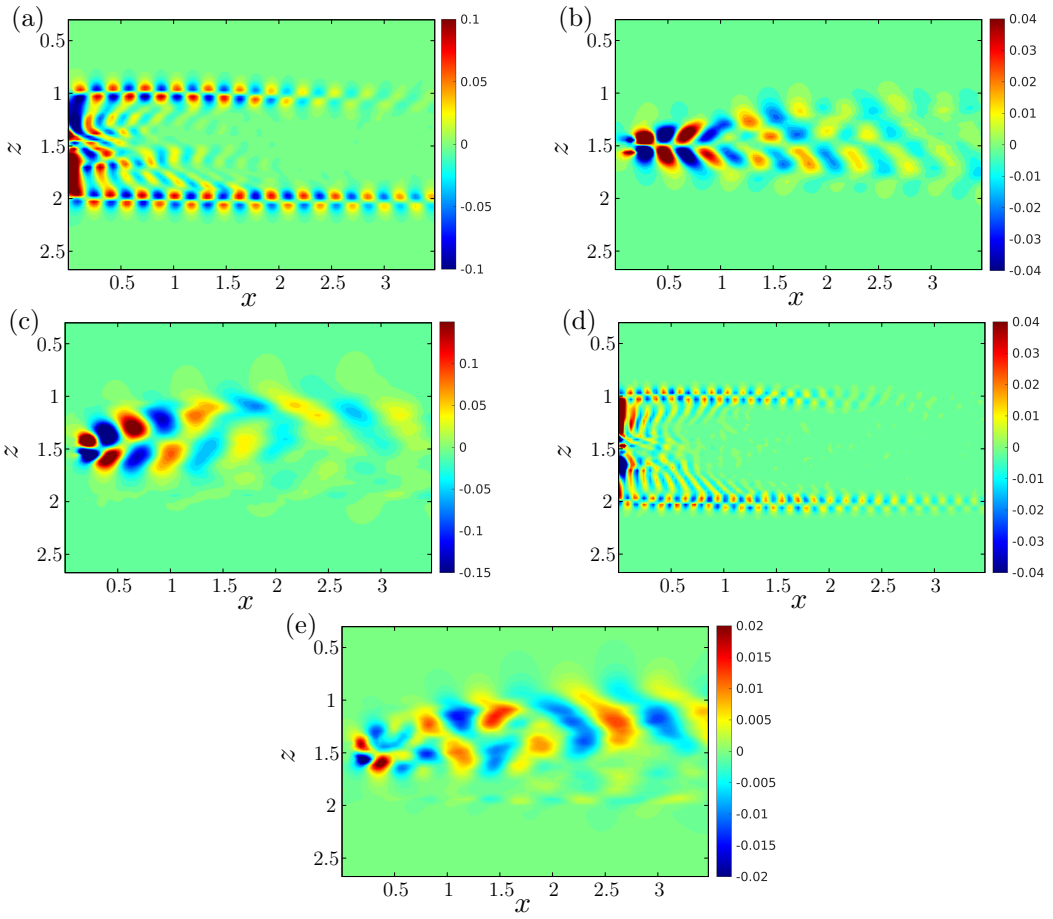

Figure 3.17: Streamwise velocity contours at $t = 0$ of the: TNNW1 pair at $y = 0$ (a), TNNW2 pair at $y = -0.5$ (b), TNNW3 pair at $y = -0.3$ (c), TNNW4 pair at $y = 0$ (d) and TNNW5 pair at $y = -0.3$ (e)

lower energy with respect to preceding pairs, the TNNW5 pair contributes to wake recovery as much as the modes characterized by higher energy, as it will be shown in section 3.5.

Far wake

In contrast to all other cases, POD analysis of the far-wake flow field in the TN configuration shows that the most energetic perturbations are not associated with the tip and root vortices. The TNFW1 pair, provided in figure 3.20(a), is characterized by a structure similar to the TNNW3 pair in the region farther from the turbine. Also their

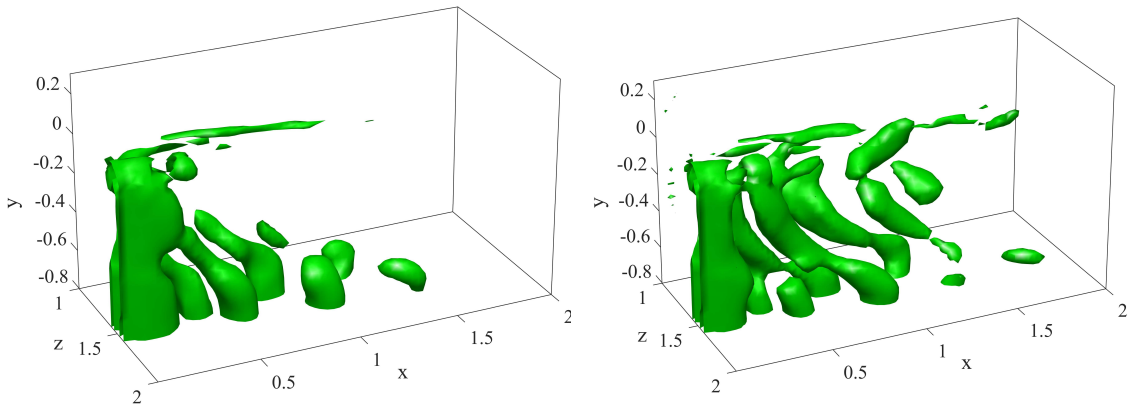

Figure 3.18: Q-criterion iso-surfaces obtained by summing mode TNNW0 to the TNNW2 (a) and the TNNW3 (b) POD pairs in the near-wake region.

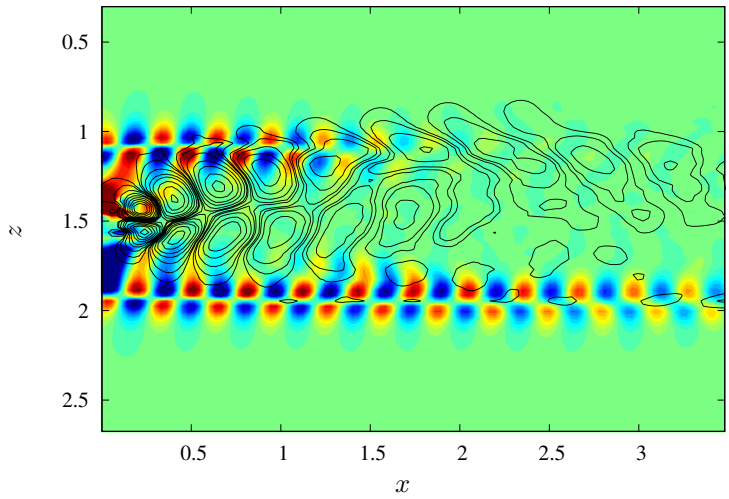

Figure 3.19: Streamwise velocity contours at $t = 0$ for the TNNW3 pair (solid contours) superimposed to the TNNW1 pair at $y = -0.3$ (shaded ones).

Strouhal numbers are similar, although the TNNW3 one is slightly higher, probably due to the presence of higher frequency oscillations close to the turbine. This suggests that these two coherent structures detected in the near and far wake may represent the same perturbation that originates just behind the rotor and reduces its frequency while propagating downstream and interacting with tip-vortex spirals. These highly energetic and dynamically relevant POD modes, together with the TNNW2/5 pairs, were totally undetected in the RO configuration. This indicates the crucial role of the turbine's tower, which strongly influences the wake both in the near- and in the far-wake region as it will be discussed in detail in section 3.5.

The successive pair of modes, TNFW2, is characterized by spatial oscillation of larger wavelength, as shown in figure 3.20(b). Both modes of this pair oscillate at an even lower frequency than the previous ones, having $St \approx 0.246$. This frequency lies within the frequency range typical of the wake meandering [66, 63, 34]. In this case, this low frequency oscillation is clearly not induced by atmospheric eddies. Rather, in the present case, nonlinear interactions between rotor and tower vortices play an important role in their generation. In fact, the TNFW2 pair is mostly concentrated on the left side of the wake, where the vortices shed by the tower hit the tip-vortices spirals leading to their breakdown.

The successive modes have a broader spectrum and a more disorganized spatial structure as can be observed from figures 3.16(b) and 3.20(c-e). The TNFW4/5 pairs might be harmonics of TNFW2, since their peak Strouhal number is approximately two times that of the TNFW2 pair (see table 3.1). One can also notice that they are more concentrated on the left side of the wake. Instead, in the flow region where the tip vortices are not broken (top/right side of the domain), the wake remains substantially straight, without strong oscillations. This confirms the crucial importance of simulating the presence of tower and nacelle for accurately describe the wake dynamics, and suggests that, in the present case, convective linear instabilities of tip-vortices spirals, if present, are energetically less important than the oscillations produced by

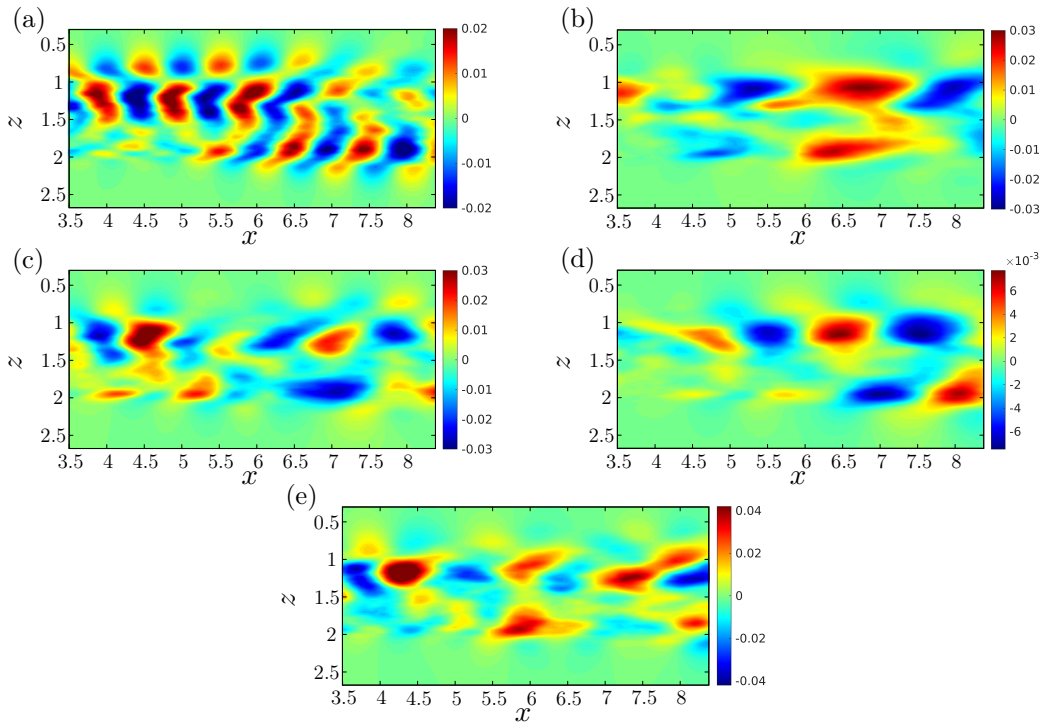

Figure 3.20: Streamwise velocity contours at $y = -0.3$ and $t = 0$ of the: TNFW1 pair (a), TNFW2 pair (b), TNFW3 pair (c), TNFW4 (d), and TNFW5 (e).

tower and nacelle.

3.4.3 Comparison of the RO and TN cases

As a summary of the presented results, figure 3.21 provides a bar plot of the Strouhal numbers of the main POD modes in the four considered cases, RONW, ROFW, TNNW and TNFW. One can notice that POD modes characterised by Strouhal number $St_l \approx 2.865$ and composed by tip and root vortices (RONW1, ROFW1 and TNNW1) are found in all considered cases but the TNFW one. In fact, in the near wake, the tip- and root- vortex system appears to be only slightly affected by the presence of the tower and nacelle. Whereas, in the far wake, the presence of tower and nacelle is found to promote the breakdown of the tip vortices, enhancing wake recovery (as it will be further discussed in section 3.5), explaining why the frequency typical of tip vortices is not found amongst the most energetic ones in the TNFW case. Similar

conclusions can be drawn for all the POD modes that are dynamically linked to the tip and root vortices, for instance the RONW2 and TNNW4 modes which represent the first harmonic of the tip vortices ($St = 5.73 \approx 2 \times 2.865$). The robustness of the modes linked to the tip vortices with regard to the presence or absence of tower and nacelle explains most of the consistencies between frequencies in the different considered cases. Only exception being the ROFW3 and TNFW1 modes, which are associated to very similar Strouhal number by mere coincidence, since these modes have a very different spatial support being connected to different physical mechanisms. In particular, the ROFW3 pair develops symmetrically throughout the azimuthal direction in the region of the tip vortices, being connected to their convective instability. Whereas, the TNFW1 is mostly located in the bottom-left region of the wake, with a pronounced asymmetry, being attributed to nonlinear interaction between the tip vortices and the wake of the tower. Figure 3.21 clearly shows that the energy is differently distributed between the modes depending on the presence (or not) of tower and nacelle. For instance, in the TN case, the first harmonic of the tip vortices (mode pair 4) has a lower energetic content with respect to other emerging modes. Moreover, new low-frequency POD modes emerge that overtake in energy those connected with the tip-vortices dynamics. These modes characterised by very low frequencies typical of wake meandering (TNFW2), remained completely undetected by the POD analysis in the rotor-only cases. In the next section, these modes will be shown to have a positive impact on wake recovery. Thus, the direct comparison of the energy and frequency content of the coherent structures in the RO and TN cases clearly indicates that despite a few similarities, several important differences can be detected in the POD modes recovered in these two cases. These results point out that for accurately describing the flow dynamics, POD analysis of coherent structures should be made in the presence of tower and nacelle, as well as on sufficiently long computational domains, in order to capture the low-frequency POD modes typical of the far wake.

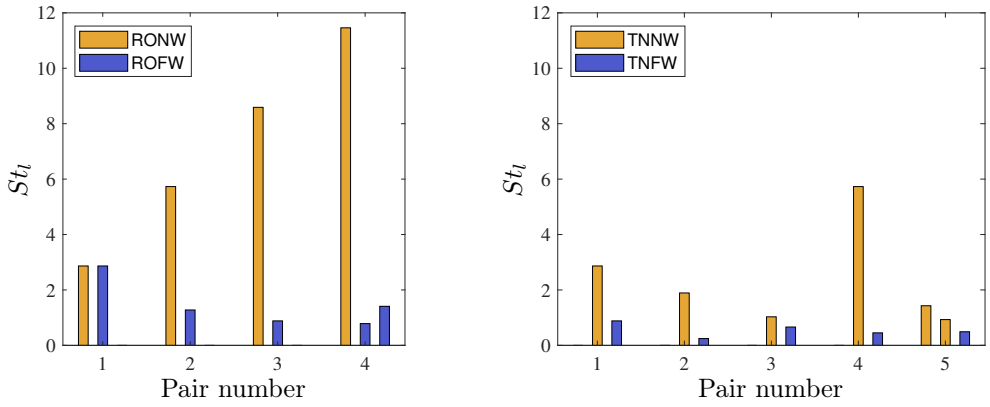

(a) RO (b) TN

Figure 3.21: Leading Strouhal numbers St_l of the most energetic POD pairs of the RO (left) and TN (right) cases.

3.5 Mean kinetic energy entrainment

It is well established that the larger the turbulence intensity of the flow approaching the turbine, the higher the wake recovery rate. In fact, the transport of mean kinetic energy within the wake is enhanced by the diffusion provided by the turbulent fluctuations. However, through quadrant analysis, Lignarolo et al[60] showed that tip vortices do not provide any contributions to the overall turbulent mixing. Medici[66] reported even a shielding effect of the tip vortices, which prevent the near-wake shear layer to recover. To assess this hypothesis, we evaluate the contribution of each POD mode to wake recovery using the following transport equation for the mean kinetic energy (M.K.E.):

$$\begin{aligned} 0 = &- \bar{u}_j \frac{\partial}{\partial x_j}\left(\frac{1}{2}\bar{u}_i\bar{u}_i\right) - \frac{\partial}{\partial x_i}(\bar{u}_i p^*) + \bar{u}_i\bar{F}_i + \frac{1}{Re}\nabla^2\left(\frac{1}{2}\bar{u}_i\bar{u}_i\right) - \frac{1}{Re}\frac{\partial\bar{u}_i}{\partial x_j}\frac{\partial\bar{u}_i}{\partial x_j} + \\ &\underbrace{-\frac{\partial}{\partial x_j}\left(\bar{u}_i\overline{u'_i u'_j}\right) - \frac{\partial}{\partial x_j}\left(\bar{u}_i\overline{\tau^r_{ij}}\right)}_{\text{Turbulent M.K.E. flux}} + \overline{u'_i u'_j}\frac{\partial\bar{u}_i}{\partial x_j} + \overline{\tau^r_{ij}}\frac{\partial\bar{u}_i}{\partial x_j}. \end{aligned} \tag{3.7}$$

It is known that the turbulent M.K.E. flux, highlighted in the equation (3.7), is the term that mostly contribute to wake recovery [85, 105, 16]. Moreover, in the wake

region, the subgrid-scale stresses are negligible with respect to the Reynolds stress terms; therefore, in this analysis, their contribution to the turbulent M.K.E. flux is neglected. The total flux of M.K.E. per unit area due to turbulent fluctuations through a generic closed surface can be evaluated, using the Gauss theorem, by the following equation:

$$\mathcal{F}_T = \frac{1}{S}\int_V -\frac{\partial}{\partial x_j}\big(\bar{u}_i\overline{u_i'u_j'}\big)dV, \tag{3.8}$$

where V is the volume enclosed by the surface S. Note that, by the above definition, the energy flux entering the volume is positive. Given the POD properties described in section 2.6, the Reynolds stress tensor can be decomposed as:

$$\overline{u_i'u_j'} = \overline{\sum_{k=1}^{N}(a_k\phi_i^k)\sum_{l=1}^{N}(a_l\phi_j^l)} = \sum_{k=1}^{N}\sum_{l=1}^{N}\overline{a_ka_l}\phi_i^k\phi_j^l = \sum_{k=1}^{N}\lambda_k\phi_i^k\phi_j^k. \tag{3.9}$$

Therefore, using this decomposition, we can compute the contribution of each POD mode to the turbulent M.K.E. flux as:

$$\mathcal{F}_T^k = \frac{1}{S}\int_V -\frac{\partial}{\partial x_j}\big(\bar{u}_i\lambda_k\phi_i^k\phi_j^k\big)dV. \tag{3.10}$$

The last equation can be rewritten as a surface integral:

$$\mathcal{F}_T^k = \frac{1}{S}\int_S -\bar{u}_i\lambda_k\phi_i^k\phi_j^k dS_j. \tag{3.11}$$

We consider a cylindrical domain of radius R_c and length L_c centered on the rotor axis and we focus on the turbulent M.K.E. flux through its lateral surface. Figure 3.22 shows the cylindrical domain of radius $R_c = 0.5$ and length L_c equal to the size of the far-wake region. The streamwise velocity isosurfaces of the ROFW3 pair are represented in red and blue, for reference. The vector representing the infinitesimal surface element $\boldsymbol{dS}$ is normal to the streamwise direction, therefore it can be expressed

in Cartesian coordinates as:

$$\boldsymbol{dS} = (0, dc_2, dc_3)\, dx, \tag{3.12}$$

where dc_2 and dc_3 are the components in the wall-normal and spanwise directions, respectively, of the vector $\boldsymbol{dc}$ normal to the infinitesimal arc of the cylinder circumference C. The total flux per unit area of turbulent M.K.E. for each POD mode over the lateral surface of the cylinder can be calculated as:

$$\mathcal{F}_T^k = \int_{L_c} f_T^k(x) dx, \tag{3.13}$$

$$f_T^k(x) = -\frac{1}{2\pi R_c L_c} \int_C \bar{u}_i(x) \lambda_k \phi_i^k(x) \phi_j^k(x) dc_j. \tag{3.14}$$

The local fluxes $f_T^k(x)$ are computed for a circumference of radius $R_c = 0.5$, whereas the total fluxes $\mathcal{F}_T^k$ through the entire surface are computed for different radii in the range $R_c \in [0.35\ 0.62]$. For avoiding a direct computation of the integrals over these cylindrical surfaces, the surface integral of equation (3.14) are transformed, using the divergence theorem, into volume integrals which are then numerically evaluated using the midpoint rule on subintervals of length compatible with the grid size. Figure 3.23(a) shows that all the most energetic POD pairs found in the near-wake region in the RO case, which are directly related to the tip and root vortices, provide mostly negative M.K.E. local flux at $R_c = 0.5$, except for some isolated, small positive peak of the RONW1/2 pairs in the vicinity of the turbine. As shown in figure 3.23(b) the total flux of all the considered modes is negative for all $R_c \leq 0.5$. Increasing the cylinder radius to $R_c > 0.5$, the total flux changes sign and becomes positive at $0.5 < R_c < 0.55$, finally decreasing towards zero for $R_c > 0.62$. This indicates that the tip vortices provide positive M.K.E. flux to an annular region with $0.5 < R_c < 0.55$ that contains the wake shear layer, as we can better observe from figure 3.24, showing both the total flux of modes RONW1 and the time-averaged streamwise velocity profile versus

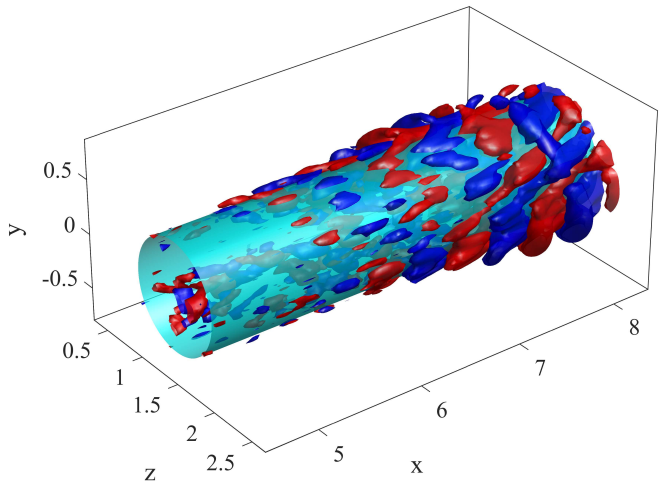

Figure 3.22: Cylindrical domain used for M.K.E. flux evaluation in the far-wake region. The red and blue isosurfaces represent the streamwise velocity component of the ROFW3 pair.

R_c. In particular, the radius at which the M.K.E. flux changes its sign corresponds to the region where the mean streamwise velocity radial profile presents an inflection point, suggesting that the mean flow profile is strongly influenced by these modes, which extract energy from the region inside the wake, feeding the mean flow shear layer. Thus, the tip vortices appear to strongly contribute to the sustainment of the wake, which remains almost unchanged in the streamwise direction (see figure 3.4(a)). Therefore, this analysis clearly indicates that the tip-vortex system in the near-wake region of the RO case does not contribute to the wake recovery, but rather it tends to sustain the velocity gradient, confirming the findings of Lignarolo et al[60]. Although a direct quantitative comparison with the results of Lignarolo et al[60] is not possible since those experiments were performed at a lower Reynolds number and a higher tip-speed ratio, it appears that the overall scenario of the entrainment is qualitatively very similar. In fact, in the near-wake region, they observe positive and negative contributions of similar magnitude to the energy flux into the wake due to the presence of the tip-vortex helix. Further downstream, after the the tip-vortex

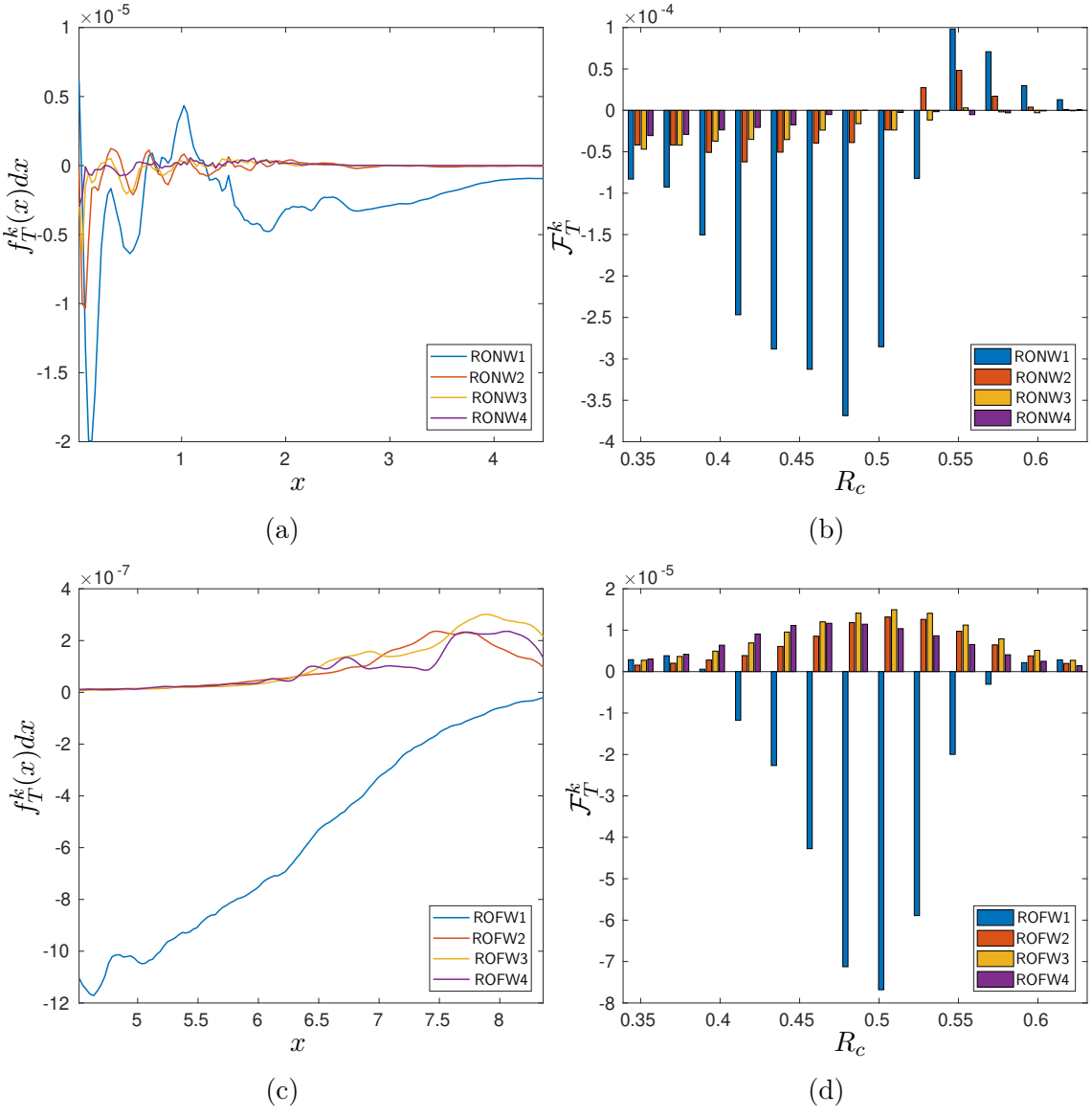

Figure 3.23: M.K.E. entrainment for the RO case: local (a)-(c) and total (b)-(d) fluxes, in the near wake (a)-(b) and in the far wake (c)-(d).

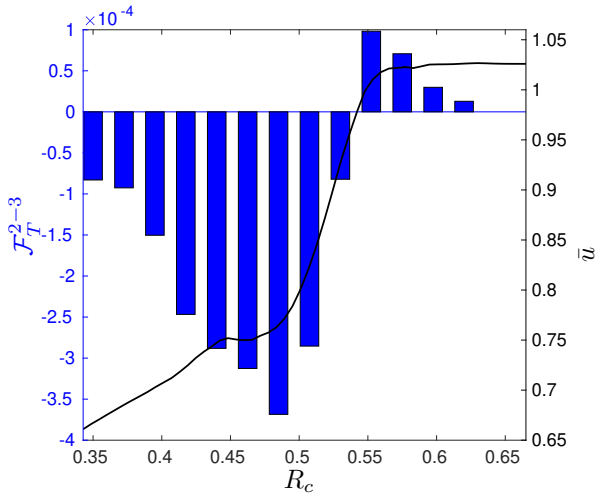

Figure 3.24: Solid line: radial profile of the time-averaged streamwise velocity $\bar{u}$ along an horizontal line at $x = 6.25$, namely at the centre of the near-wake domain for the RO case. Bar chart: total M.K.E. flux for the RONW1 pair versus the radius R_c of the cylindrical surface over which the flux is computed.

breakdown, a positive flux, corresponding to a net entrainment of kinetic energy into the wake, is observed. In our computations, we have decomposed the energy flux contributions among the POD modes. We have found that the contribution to the energy flux into the wake of the modes associated with the tip vortices (pair 1 in figure 3.23(c)) is always negative and it reduces in modulus with the distance from the rotor. At about $x/D = 6.5$, it is counterbalanced by the positive flux contribution of modes 2-4 which give a positive entrainment, starting the recovery process of the wake. The abscissa at which the recovery process starts is strongly dependent on the flow condition (Reynolds number and tip-speed ratio) and on the interaction with the tower and nacelle wake; in the case studied by Lignarolo et al[60], the recovery process starts about at $x/D = 1.5 - 1.7$, depending on the value of the tip-speed ratio. Concerning the far-wake region of the rotor-only case, the first POD pair (ROFW1), being characterized by tip vortices, presents a negative local M.K.E. flux at $R_c = 0.5$ similarly to the near-wake modes (compare figures 3.23 (a)-(c)). Moreover, figure 3.23 (d) shows that the total M.K.E. flux provided by this mode is negative in the region $0.4 < R_c \leq 0.55$, becoming positive for larger radii, as found for near-wake modes.

The other POD pairs, instead, provide a positive local and total flux, the latter reaching its maximum for $0.5 < R_c < 0.55$, but remaining positive for all considered radii. Therefore, in contrast to the tip vortices, these modes appear beneficial to wake recovery, since they transport the mean kinetic energy inside the wake.

The same analysis has been performed for the POD pairs found in the TN case. Figures 3.25(a)-(b) show the M.K.E. local and total fluxes for POD pairs in the near-wake region. The TNNW1 and TNNW4 pairs, which are characterised by tip vortices, behave similarly to the corresponding POD pairs related to tip vortices found in the RO case. The successive modes, as in the far-wake region of the RO case, appear beneficial to wake recovery, providing positive total M.K.E. flux through the cylindrical surfaces for any R_c. In the far-wake region of the TN case, as already observed in section 3.4.2, tip vortices are not recovered among the most energetic POD modes. As a consequence, Figures 3.25(c)-(d) clearly show that all of the POD pairs provide positive flux at every radius, thus positively contributing to the mean flow diffusion and to the wake recovery. This analysis suggests that the oscillations generated by the presence of tower and nacelle play a crucial role on wake recovery for three main reasons. The first one is that high-energy modes generated by tower and nacelle are active in the M.K.E. entrainment mechanism from the very near wake, whereas, the near wake of the rotor-only case is characterised only by modes that do not contribute positively to the wake recovery. The second reason is that, even in the far wake, the most energetic coherent fluctuations found in the presence of tower and nacelle have a stronger impact on wake recovery with respect to those characterising the RO case. Comparing figures 3.23 (d) and 3.25 (d), we can notice that the mean kinetic energy fluxes measured in the TN case are about three times those calculated for the RO case. The third reason is that the presence of tower and nacelle reduces the shielding effect of tip vortices to wake recovery. Tip vortices break down beforehand due to interactions with coherent structures generated by tower and nacelle, as discussed in detail in section 3.4.2, leading to the generation of other low-

frequency modes, some of those linked to the wake meandering, which are instead beneficial to wake recovery.

3.6 Conclusions

This work provides a detailed analysis of the wake produced by a three-bladed wind turbine and of the main embedded coherent structures, which are identified by means of Proper Orthogonal Decomposition (POD). The analysis is based on large eddy simulations of a model wind turbine with an incoming uniform velocity profile at a fixed tip-speed ratio $\lambda = 3$. The turbine is simulated with and without tower and nacelle, for evaluating their effect on the wake dynamics. In both cases, rotor blades are modeled using the actuator line method, whereas tower and nacelle are modeled using an immersed boundary method. Time- and phase-averaged flow fields are computed and analyzed, highlighting and comparing the main flow features in the rotor-only (RO) and tower and nacelle (TN) cases. In the latter case, the far wake is characterized by a higher velocity on the left side of the turbine, related to a faster overall recovery. Analysis of the phase-averaged RO-case flow shows that tip-vortices spirals are advected downstream almost undisturbed until the end of the computational domain. Whereas, in the TN case, breakdown of the tip vortices occurs at the bottom and left side of the wake, suggesting a correlation between the tip-vortices breakdown and the increased wake recovery. Based on the evaluation of the kinetic energy of the phase-averaged flow field, we propose a criterion to discriminate the near- from the far-wake region of the flow. The unsteady flow fields are studied separately in these two subdomains (near and far wake) using POD for capturing the energy-containing structures embedded in the turbulent flow. In the RO case, the most energetic POD modes are characterised by tip and root vortices. In the far wake, lower frequency POD modes are recovered, which appear to be linked to a vortex pairing process. In the TN case, in addition to tip and root vortices, highly

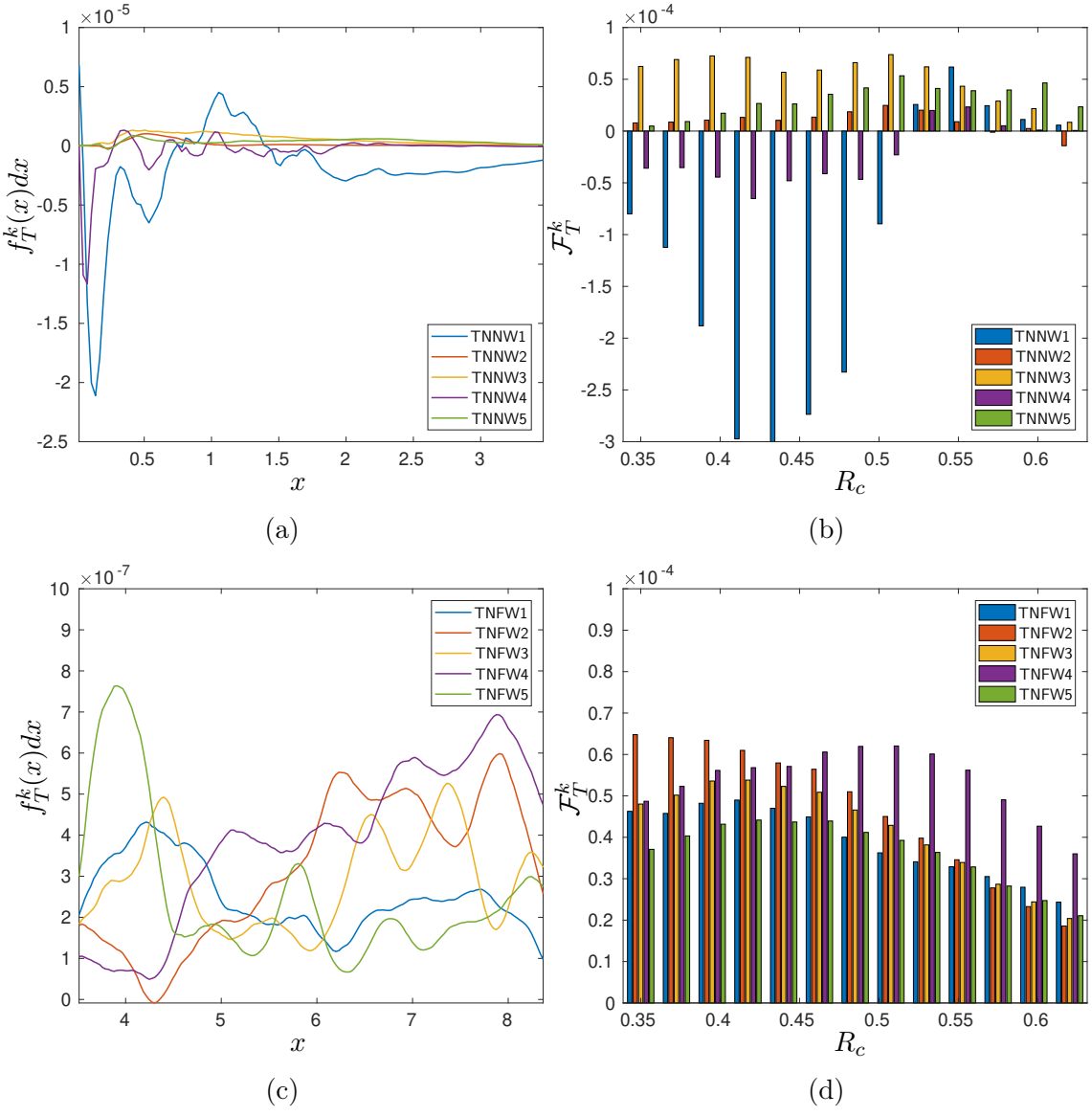

Figure 3.25: M.K.E. entrainment for the TN case: local (a)-(c) and total (b)-(d) fluxes, in the near wake (a)-(b) and in the far wake (c)-(d).

energetic POD modes connected with the Kármán vortex street developing behind the tower are found as well. These vortical structures originate in the near wake just behind the rotor and are advected towards the left side of the wake, until they interact with and break down the tip vortices on the bottom and left side of the wake. This interaction between tip vortices and tower vortices leads to low frequency oscillations also in the far wake. In the same region, POD modes characterized by a very low Strouhal number ($St = 0.246$) lying in the typical range of the wake meandering, are recovered. These coherent structures appear to be linked to non-linear interactions of coherent structures generated in the near wake by the presence of the tower.

POD analysis has also been used to investigate in detail the wake recovery process, where turbulent fluctuations play a fundamental role. The effect of each POD mode on wake recovery is evaluated computing its contribution to the mean kinetic energy entrainment[105]. The mean kinetic energy flux provided by each POD mode through the surface of a cylinder of radius R_c, centered on the rotor axis, is computed. The flux provided by the tip vortices is negative for small radii and then becomes positive for larger radii. Thus, tip vortices provide positive flux into an annular region containing the wake shear layer, sustaining the mean velocity gradient and slowing down the wake recovery. Whereas, a positive flux is observed at each radius for POD pairs related to the tower's wake, compensating the shielding effect of the tip vortices and finally enhancing the wake recovery process. These findings indicate the crucial importance of considering tower and nacelle when simulating the flow behind a wind turbine.

Chapter 4

Mean flow linear analysis of a rotor-only turbine wake

4.1 Introduction

In this section, we perform two-dimensional modal and non-modal stability analysis of the turbulent mean flow developing downstream of a wind turbine rotor. The main objective is to verify to what extent is possible or meaningful to describe the coherent structures extracted via POD as linear coherent waves. The database is numerical and computed by Large-Eddy-Simulation in combination with the actuator line technique to simulate the rotor (chapter 3). The presence of tower and nacelle is, in this case, neglected. The POD modes obtained for the rotor-only case in the far wake and described in section 3.4.1 are recalled here and analyzed in terms of their spectral content in space and time. Linear stability and optimal forcing analyses have been carried out in different cross-sections sufficiently far from the rotor, where non-parallel effects are rather weak. The frequency content and spatial structure of the most amplified perturbations are compared with that of the most energetic coherent structures recovered by POD analysis.

4.2 Spectral characterization of POD modes

In this section the POD modes already discussed in section 3.4.1 are further analyzed in terms of spectral properties.

The frequency content of the first POD mode (see Figure 4.1) in both space and time is provided in figure 4.2, showing the Fourier spectra in time and in the streamwise and azimuthal directions. Since the mode is almost periodic in time (see bottom frame of figure 4.1), the time spectrum has only a sharp peak at $\omega = 18$, corresponding to three times the non-dimensional rotational frequency. The Fourier spectrum in the streamwise direction, resulting from the averaging of the Fourier spectra computed at different wall-normal and spanwise locations within the subdomain, shows a clear peak at $\alpha = 20.92$, corresponding to the tip-vortices pitch. In the azimuthal direction, the Fourier spectrum, resulting from the averaging of different spectra obtained for different radial and streamwise positions, peaks at the azimuthal wavenumber $m = 3$, corresponding to the number of blades of the rotor. The successive pairs of modes have lower frequencies both in space and time, as shown by the spectra in figure 4.3 (left column) for the 3^{rd}, 5^{th} and 7^{th} POD modes (from top to bottom), belonging to the ROFW2, ROFW3, ROFW4, respectively (see Table 3.1). Figure 4.4 provides the streamwise velocity contours of the same POD modes (from top to bottom, respectively), showing that they are mostly located in the tip-vortices region, and to a lesser extent, in the core of the wake, where radial gradients due to the central jet are present. These modes seem to capture the convective instabilities of the tip and root vortices developing in the regions of high shear of the far wake. One of these instabilities is the mutual inductance instability phenomenon investigated extensively by Sarmast et al.[89], which is characterized by a streamwise frequency which is about half the tip vortices' frequency. Here, the 3^{rd} POD mode has the main temporal and streamwise wavenumbers about equal to half the tip-vortex ones, namely $\omega \approx 8$ and $\alpha \approx 9$ (see the top left frame of figure 4.3). An analysis of the radial distribution of the main streamwise wavenumbers of this POD mode, averaged on the azimuthal

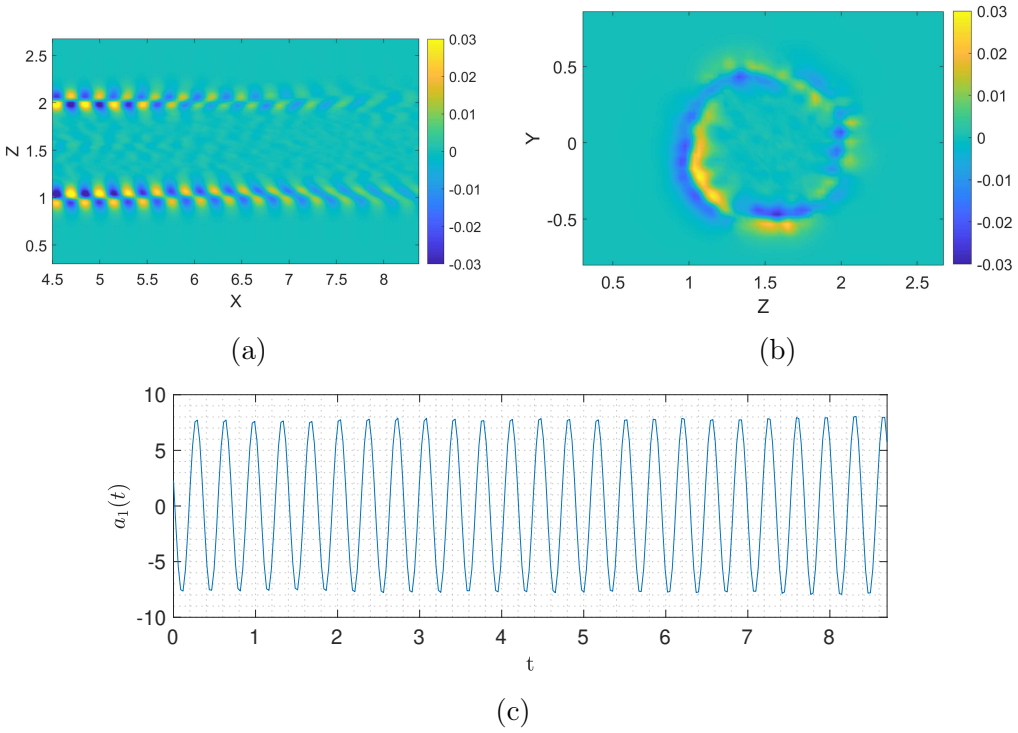

Figure 4.1: Streamwise velocity contours of the 1^{st} POD mode (ROFW1) in different planes and in a three-dimensional visualization. The bottom plot represents the evolution of the associated temporal coefficient.

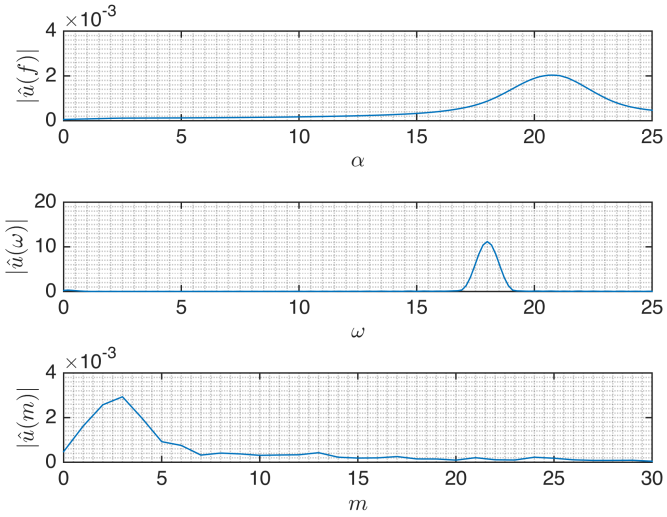

Figure 4.2: Spectra of the 1^{st} POD mode in time (top) and in the streamwise (middle) and azimuthal (bottom) directions.

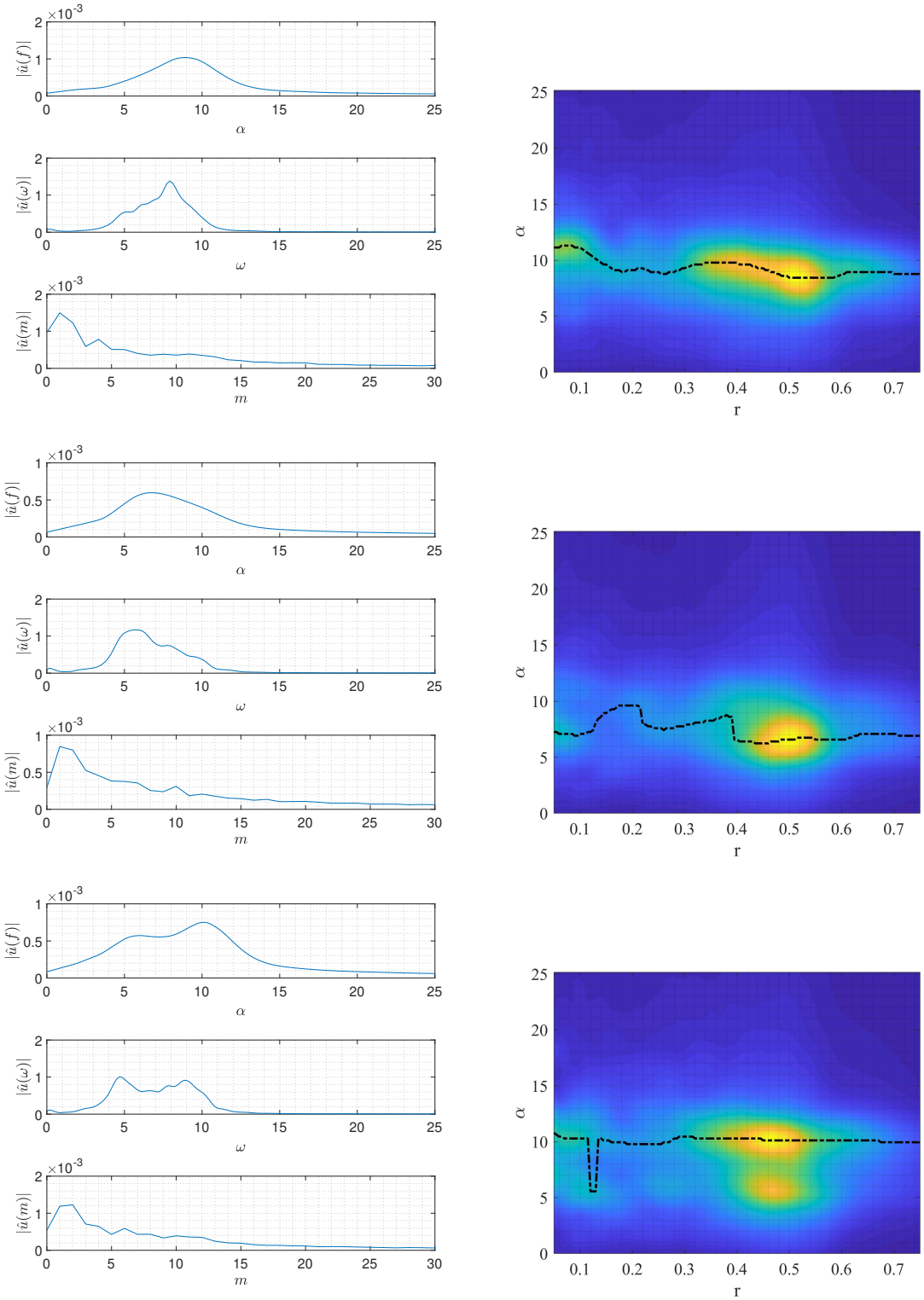

Figure 4.3: ((Left) Fourier transform in time, streamwise and azimuthal directions of the 3^{st} (top), 5^{th} (middle) and 7^{th} (bottom) POD mode in the streamwise, temporal and azimuthal directions. (Right) Streamwise frequency of the mode on the left for different radii, averaged on the azimuthal direction.

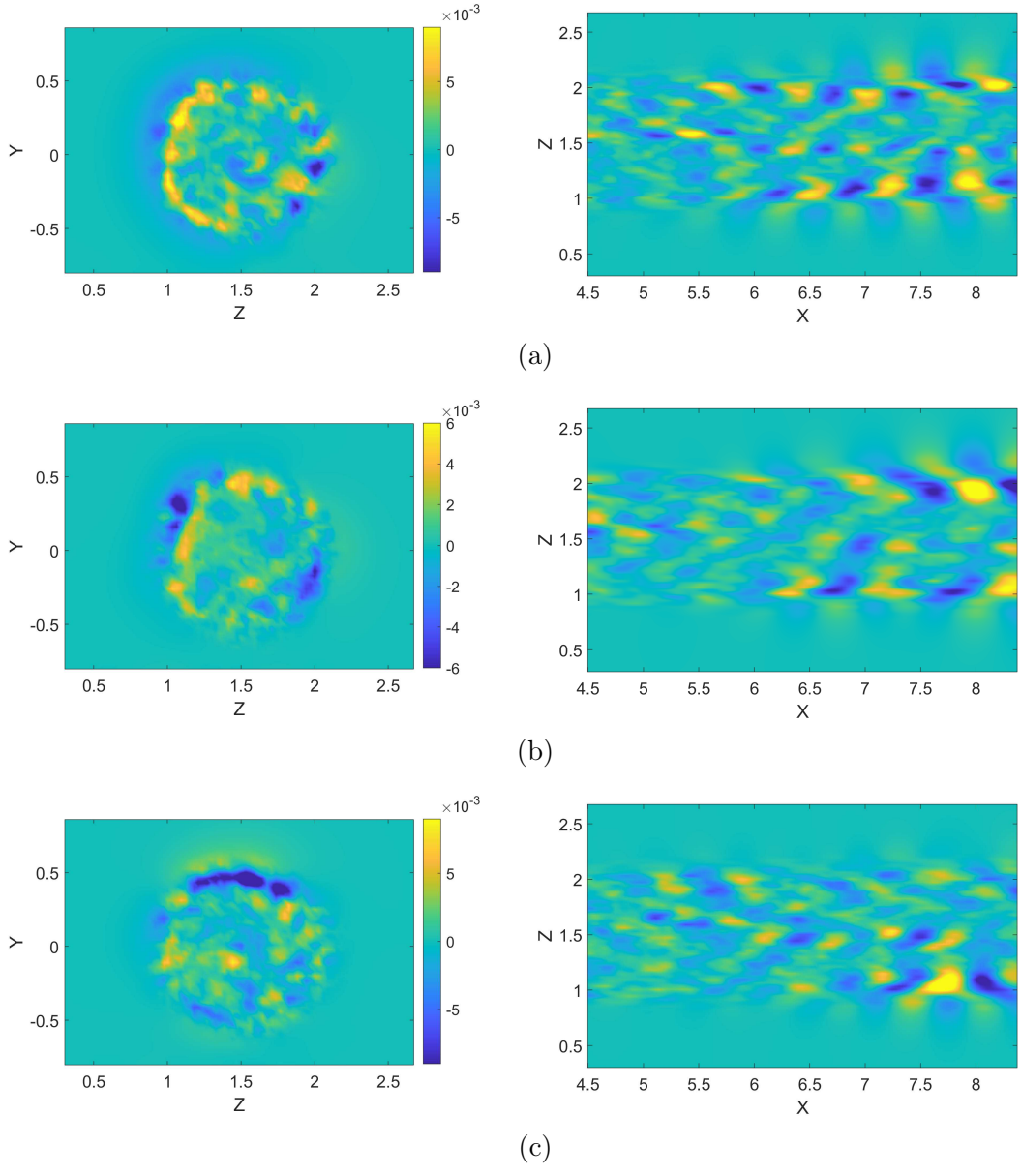

Figure 4.4: Streamwise velocity contours of the 3^{rd} (a) 5^{th} (b) and 7^{th} (c) POD modes in the $x = 6.5$ and $y = 0$ planes.

direction, shows that the main α peak is located at $r \approx 0.5$, in correspondence of the tip vortices. A weaker peak is found also at $r \approx 0$, in correspondence with the root vortex system, associated to a slightly larger value of α. Similarly to the mutual inductance instability discussed by Ivanell et al. [49], these POD modes produce an out-of-phase displacement of two consecutive tip vortices, leading to vortex pairing in the tip vortex system, which promotes its break down.

The 5^{th} POD mode has a spatial structure similar to that of the 3^{rd} mode, but is characterized by slightly lower temporal and streamwise wavenumbers, namely $\omega \approx 6$ and $\alpha \approx 7$. Moreover, the streamwise wavenumber appears to be only slightly dependent on the radial direction, being mostly localized in the outer part of the wake ($r \approx 0.5$), as shown in figure 4.3. As it will be discussed in the following, this POD mode seems to be originated by a convective instability of the mean shear induced by the presence of the wake. The 7^{th} mode presents a more broadband temporal and streamwise spectra, with two peaks at wavenumbers close to those of the previous modes. In particular, the two main streamwise wavenumbers are $\alpha \approx 10.1$ and $\alpha \approx 6$, and two equally strong peaks are recovered in time, with $\omega \approx 4.7$ and 8.9. Moreover, the spatial structure of this mode is very close to that of the previous two ones, suggesting a similar physical mechanism at their origin. Finally, it is important to remark that the main azimuthal wavenumber of all these POD modes is $m = 1$ (although the 7^{th} mode presents also an $m = 2$ peak), indicating a strong similarity of the structure and physical origin of these modes. In the next section, we consider these results as a benchmark for the linear stability analysis; in particular, the most amplified spatial frequencies α in each of the cross-sections $x = x_0$ are considered. The final goal is to verify the extent to which is meaningful to describe the identified coherent structures as governed by linear mechanisms.

4.3 Mean flow stability analysis

In this section, we perform a meanflow stability analysis, described in section 2.8.1, by considering two-dimensional planes at different locations along the streamwise direction. Two considerations are in order. First of all, as a meanflow analysis is considered, the comparisons that we carry out between the linear models predictions and the turbulent flow generated by the wind turbine are mostly qualitative and needs to be assessed a posteriori. From a theoretical viewpoint, the analysis of spectral POD (SPOD) modes would be more appropriate [62, 75]: a single POD mode can contain multiple flow structures with different frequencies, originated from different physical mechanisms. Moreover, recent works have been shown that a relation exists between the spectral POD modes and the frequence response obtained from the decomposition of the resolvent operator [58, 104], under the assumptions that the forcing harmonically drives the system at the different frequencies with equal spectral density (i.e. white noise). However, a larger number of snapshots is required to achieve convergence with respect to POD. Due to this limitation, we still adopt the POD and recover the frequencies information by means of Fourier transform during the post-processing, for a quantitative analysis of the spectral content. The analysis has been performed at three different streamwise location, namely $x = \{3.5, 4.5, 6.5\}$. In figure 4.5 the mean streamwise velocity is shown at three different streamwise locations. The incoherent fluctuations considered for the Reynolds stresses computation clearly correspond to the difference between the instantaneous velocity $\boldsymbol{u}$ and the phase-averaged flow $\langle \boldsymbol{u} \rangle$. Here the phase average is computed according to (2.61), taking the sampling period equal to the period of rotation of the rotor, $\tau = 1/St_r = 1.047$. The eddy-viscosity field, shown in figure 4.6, is then computed according to the (2.66). It can be noted that the eddy-viscosity is concentrated in the wake region and increases moving downstream. The two-dimensional domain employed for the stability analysis has been truncated in the y direction ($y = [0.11\ 2.61]$), in order to discard the wall boundary layer and the far-field. The computational domain comprises $N_y = 75$ and

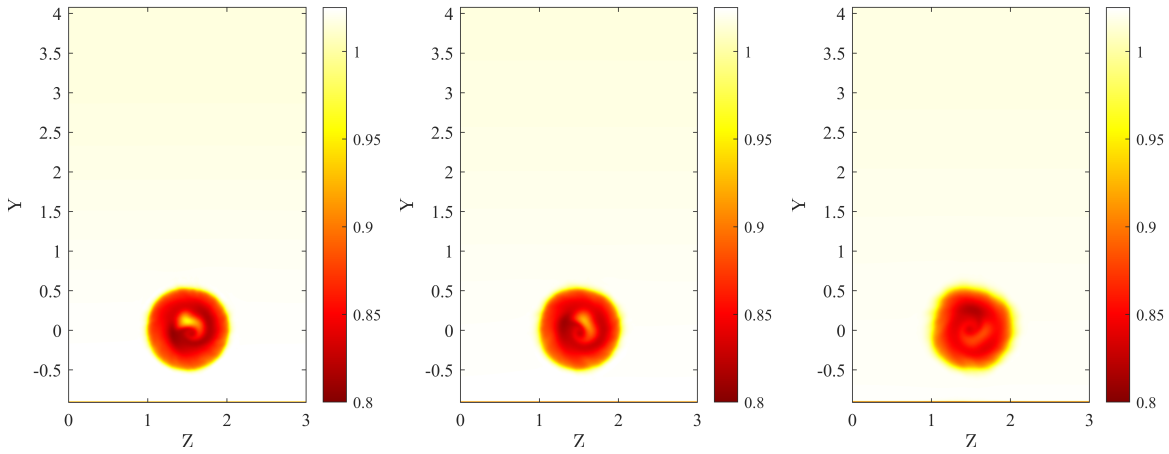

Figure 4.5: Mean streamwise velocity $\overline{u}$, at $x = 3.5$ (a), $x = 4.5$ (b) and $x = 6.5$ (c).

$N_z = 72$ collocation points in the wall-normal and spanwise directions, respectively. Figure 4.7 provides the stability eigenspectra computed for the cross-sections $x = 3.5$ and $x = 6.5$ for different values of α ranging from 3 to 10. At $x = 3.5$, the spectrum shows branches of unstable modes, one for each α considered here. A similar situation is obtained for the $x = 6.5$ plane and $\alpha < 8$, while stable modes are found for larger α. The corresponding growth rates of the most unstable modes as a function of α are shown in Figure 4.8(a) for $x = 3.5$, $x = 4.5$, and $x = 6.5$. It can be noted that by moving downstream of the rotor, the maximum growth rate decreases and attains values of α progressively smaller, going from $\alpha \approx 6$ at $x = 3.5$ to $\alpha \approx 3.5$ at $x = 6.5$. In Figure 4.8(b), we can observe that the angular frequency of the most unstable modes is proportional to the value of α imposed for the stability analysis, with the relation $\omega_r \approx \alpha$ in all cases except at $x = 6.5$ when a change can be observed at $\alpha \gtrapprox 8.25$. We can conclude that, stronger, higher-frequency instabilities are predicted by the linear model in the vicinity of the rotor. The eigenvectors corresponding to the most unstable eigenmodes at $x = 3.5$, $x = 4.5$ and $x = 6.5$ are shown in Figure 4.9a-c. In the two closest planes to the rotor, the most unstable modes are radially modulated as shown by the alternation of positive/negative streamwise disturbances, mostly localized at

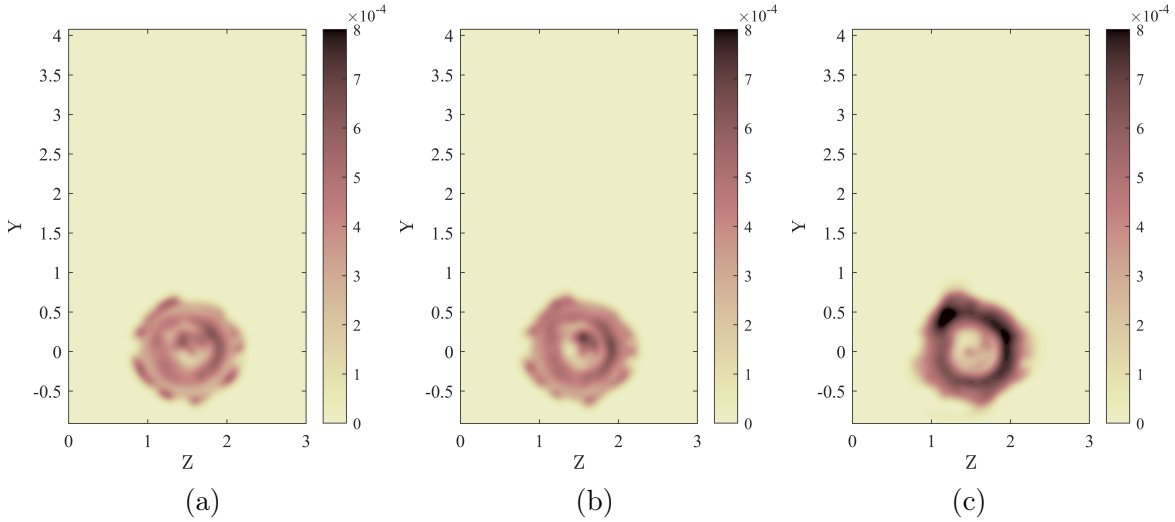

Figure 4.6: Turbulent viscosity ν_t, at $x = 3.5$ (a), $x = 4.5$ (b) and $x = 6.5$ (c).

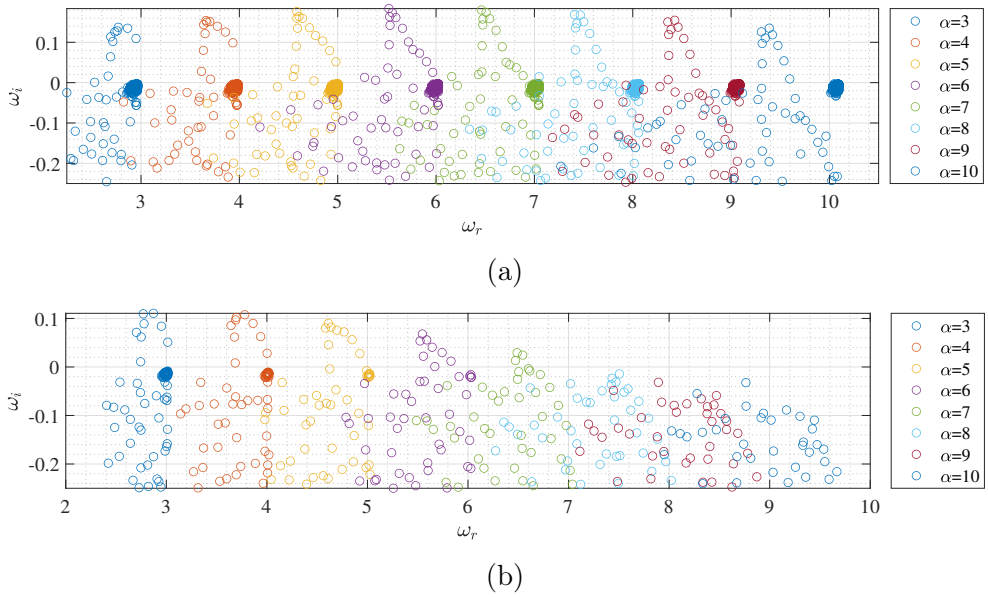

Figure 4.7: Eigenvalues spectra for $x = 3.5$ (a) and $x = 6.5$ (b) for different values of α reported in the legend.

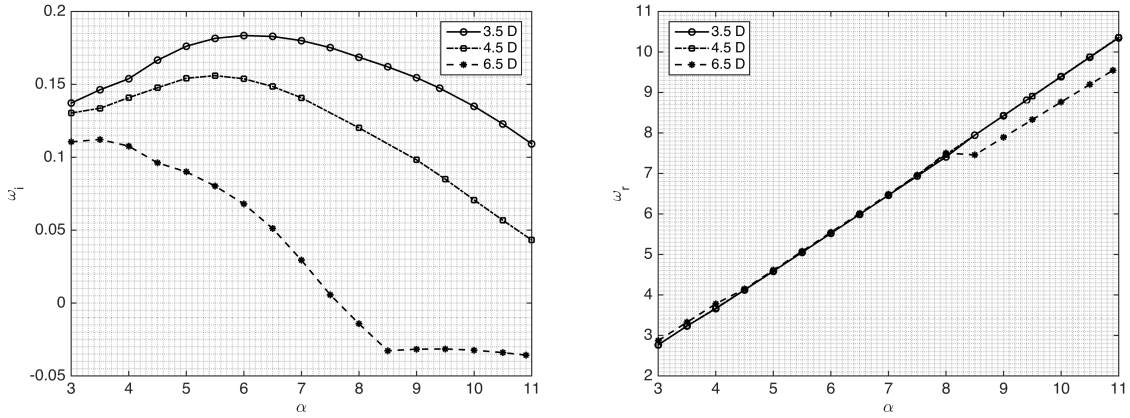

Figure 4.8: (a) Growth rates of the most unstable eigenmodes for different streamwise frequencies α. (b) Temporal frequencies associated to the growth rates in (a)

$r \approx 0.5$ and along the centerline $r \approx 0$. A streamwise view of the u component of these modes is provided in the right frames of Figure 4.9.

Focusing on the most unstable modes at $x = 3.5$ and $x = 4.5$, we observe that their structure is mostly localized on the right region (with respect of an observer looking downstream). This asymmetry is attributed here to the meanflow, characterized by different shear intensities in the azimuthal direction, as shown in Figure 4.10 for four different azimuthal angles $\theta = \{0, \pi/2, \pi, 3\pi/2\}$) at $x = 3.5$ and $x = 6.5$. In particular, Figure 4.10 shows that, in the plane closest to the rotor, the meanflow shear is less pronounced in the left part of the wake, whereas, in this right region of the wake, the streamwise velocity profile presents two inflection points in the radial direction, *i.e.* $\partial^2\overline{u}/\partial r^2 = 0$. This is not the case at $x = 6.5$, due to the mean kinetic energy entrainment: in this case the radial shear is slightly weaker and more uniform in both radial and azimuthal directions. Thus, the unstable mode has almost the same intensity in different azimuthal positions. All these features can be summarised by analysing the three-dimensional rendering of the modes in Figure 4.11*a*-*b*, for $x = 3.5$, $\alpha = 6$ and $x = 6.5$, $\alpha = 3.5$, respectively; here, the most unstable mode at $x = 3.5$ shows streamwise-alternating and azimuthally-elongated patches following the mean-

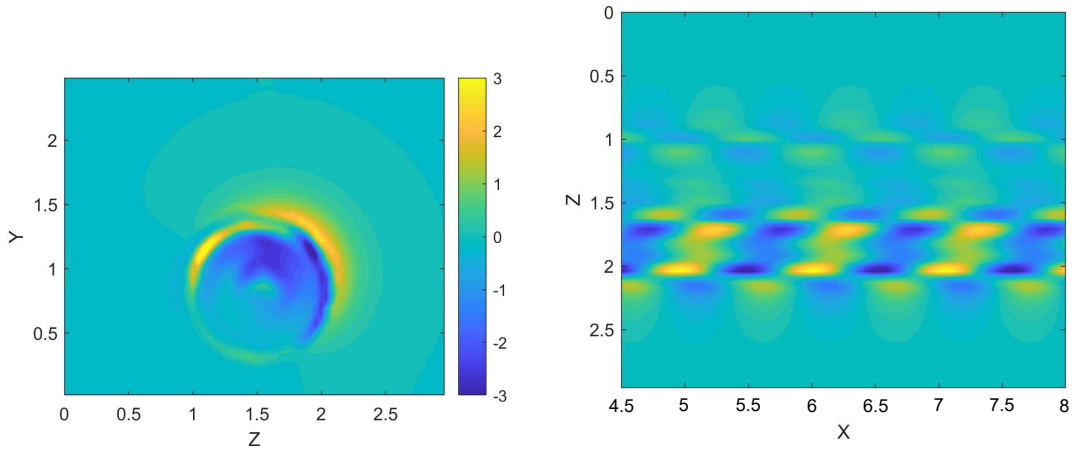

(a)

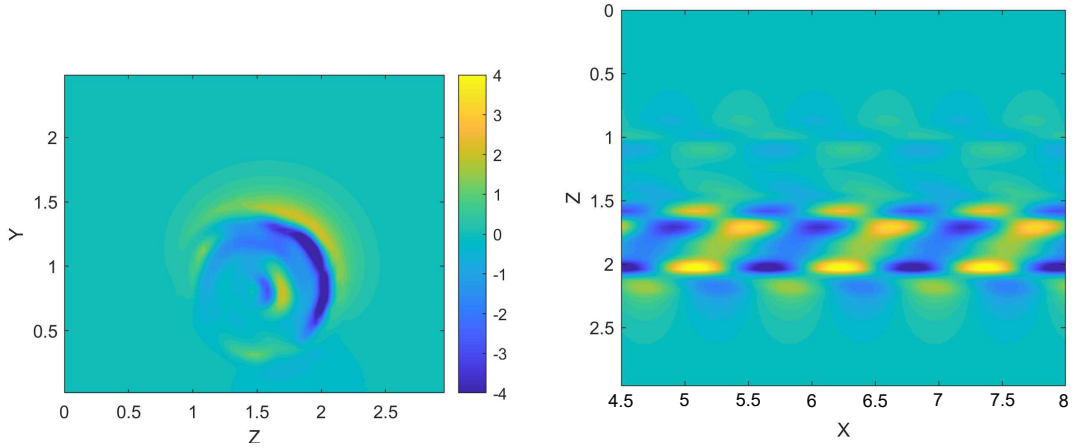

(b)

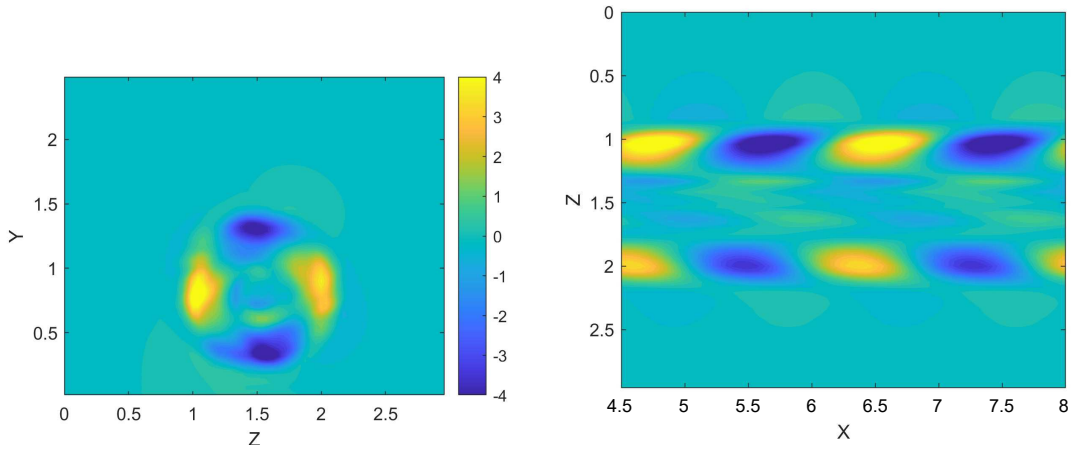

(c)

Figure 4.9: Streamwise component of the most unstable eigenmode for x=3.5 and $\alpha = 6$ (a), x=5.5 and $\alpha = 5.5$ (b), and x=6.5 and $\alpha = 3.5$ (c) in a (Left) z-y and (Right) x-z plane, after reconstruction of the perturbation in the streamwise direction.

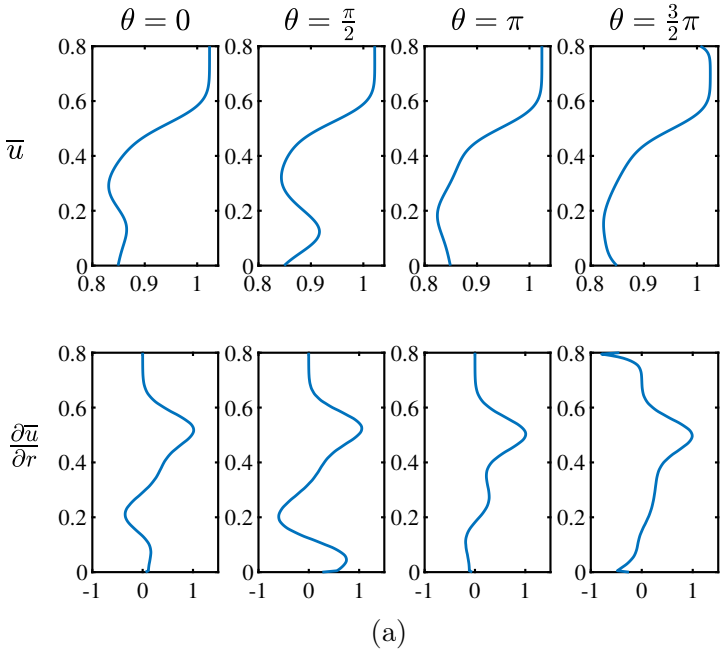

(a)

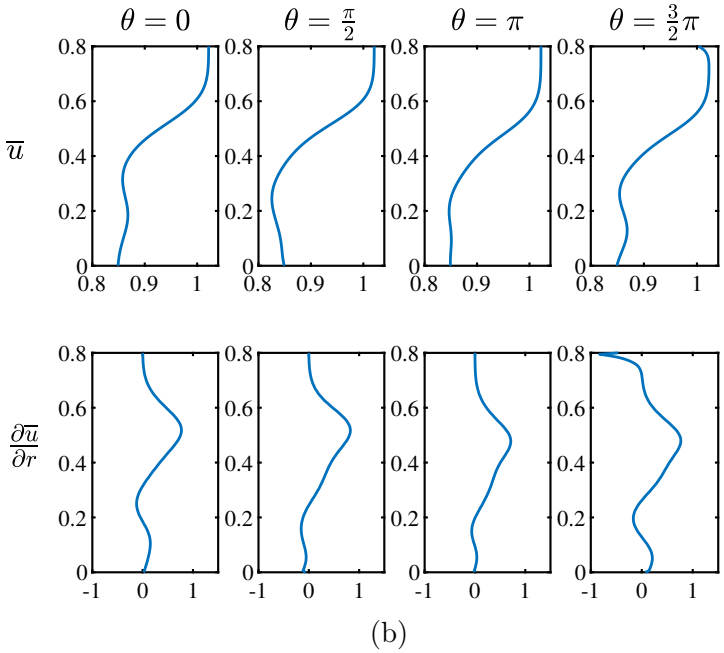

(b)

Figure 4.10: Mean flow profiles at four different azimuthal positions, $\theta = 0, \pi/2, \pi, 3\pi/2$, corresponding to the right, bottom, left and top part of the wake, respectively, in the cross-flow planes at $x = 3.5$ (a) $x = 6.5$ (b).

flow shear in the upper-right part of the wake, while the mode at $x = 6.5$ develops a double-helix structure.

We consider now the POD modes analysed in 4.2, except for the first pair of modes, which capture the tip-vortex helices. In fact, the tip vortices are "forced" by the rotor and do not emerge as an instability of the wake meanflow. By analysing the spectral content of the following POD modes, we observe that the main streamwise angular frequency found in the 5^{th} POD mode and in the second peak of the 7^{th} POD mode (see the bottom frame of Figure 4.3), $\alpha \approx 6$, is very similar to the streamwise frequencies of the most unstable modes found at $x = 3.5$ and $x = 4.5$, namely $\alpha = 6$ and $\alpha = 5.5$, respectively. In fact, the overall spatial structure of the latter, provided in Figure 4.9, resembles the POD modes $5 - 7$. Moreover, a Fourier transform in the azimuthal direction, provided in Figure 4.12 shows that the main azimuthal wavenumber of the most unstable mode found in the plane closest to the rotor, coincides with that of the most energetic POD modes, namely, $m = 1$. Whereas, the most unstable mode for $x = 6.5$, found for $\alpha = 3.5$, is characterized by main azimuthal wavenumber $m = 2$, and by structures of longer wavelength in the streamwise direction. Neither this wavenumber, nor the double-helix structure of this eigenmode, shown in Figure 4.11, is recovered in the main POD modes. This is probably due to an insufficient length of the computational domain in the streamwise direction. In fact, the angular frequency $\alpha \approx 3.5$ corresponds to a wavelength $\lambda_x = \frac{2\pi}{\alpha} \approx 1.8$. Since the unstable mode with $\alpha \approx 3.5$ emerges at $x = 6.5$, only one wavelength can be contained in this portion of the domain, which may be insufficient to capture unambiguously such instability.

4.4 Optimal forcing analysis

In the previous section, we noted that the most unstable mode found at $x = 6.5$ is not identified by the POD. However, at the same location, the meanflow is linearly

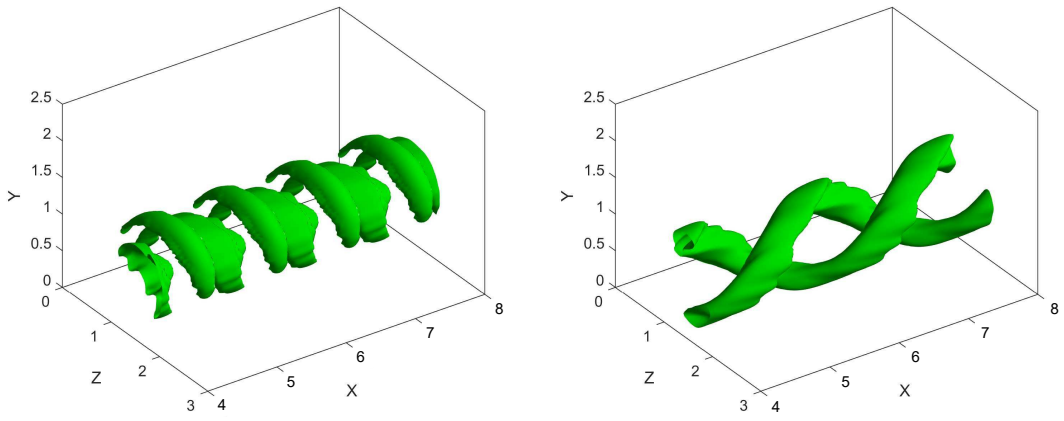

(a) (b)

Figure 4.11: Isosurface of streamwise velocity of the three-dimensional reconstruction of the most unstable mode for (a) $x = 3.5$, $\alpha = 6$, and (b) $x = 6.5$, $\alpha = 3.5$.

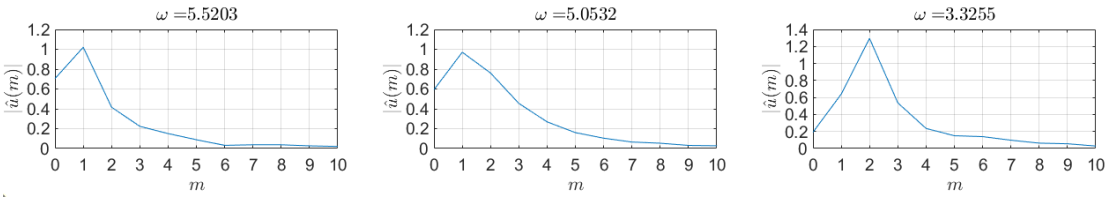

(a) (b) (c)

Figure 4.12: Fourier transform in the azimuthal direction of the streamwise component of the eigenmode at x=3.5 and $\alpha = 6$ (a), x=5.5 and $\alpha = 5.5$ (b), and x=6.5 and $\alpha = 3.5$ (c), all representing the maximum growth rate in the considered plane.

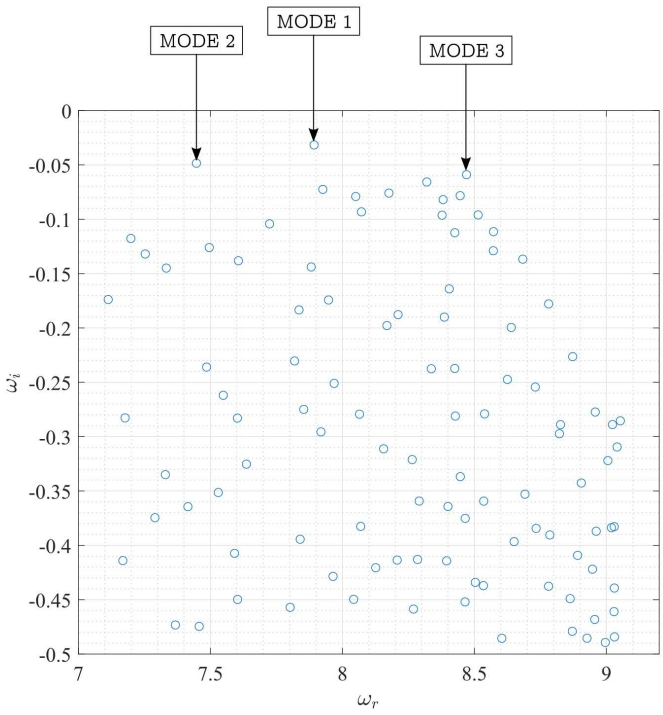

Figure 4.13: Eigenvalues spectrum for $x = 6.5$ and $\alpha = 9$.

stable for $\alpha > 7.5$. This allows us to complement the linear stability analysis with a resolvent analysis, which enables to scrutinize the response of the system when harmonically driven by real frequencies and to identify the corresponding optimal forcing. In order to do so, we consider, in particular, the main streamwise frequency that characterize the third POD mode, namely $\alpha = 9$ (see the top frames of Figure 4.3). Inspecting the corresponding eigenspectrum provided in Figure 4.13, we note that there are three modes lying very close to the neutral axis, whose spatial structure is shown in Figure 4.14. The two of them which are characterized by a (slightly) lower angular frequencies are mostly localized in the region $r \approx 0$, showing positive/negative streamwise disturbances alternating in the azimuthal direction. Whereas, the mode with highest temporal wavenumber is mostly localized in the $r \approx 0.5$ region, showing a more complex flow structure. This correspondence between localization and wavenumber is consistent with what has been observed in the 3^{rd} POD mode, being characterized by slightly larger wavenumbers in the root region

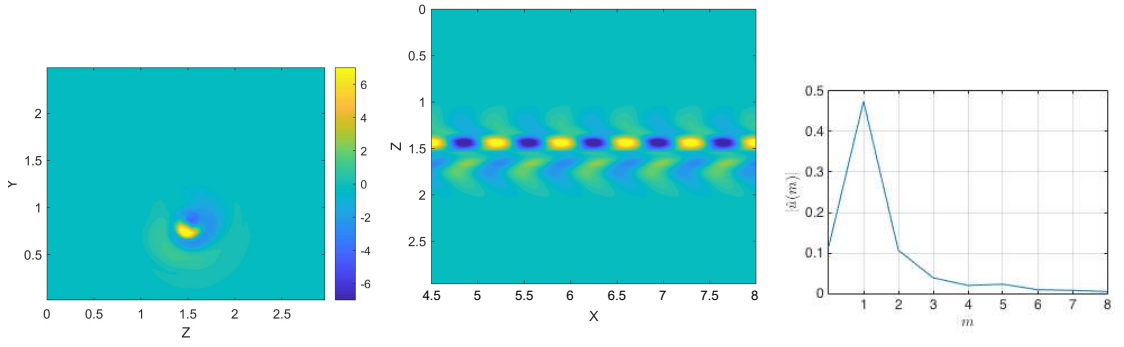

(a)

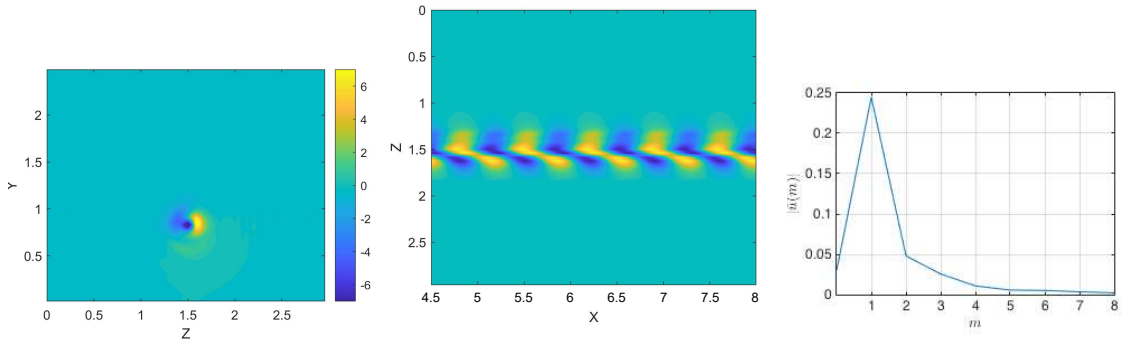

(b)

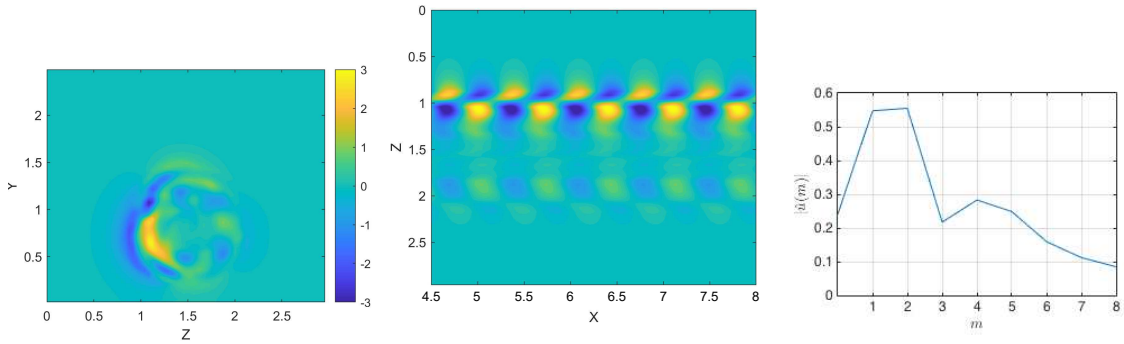

(c)

Figure 4.14: First (a), second (b) and third (c) most unstable modes obtained for x=6.5 and $\alpha = 9$: streamwise disturbance in the z-y (left) and in the x-z plane (middle) and associated Fourier amplitudes in the azimuthal direction (right).

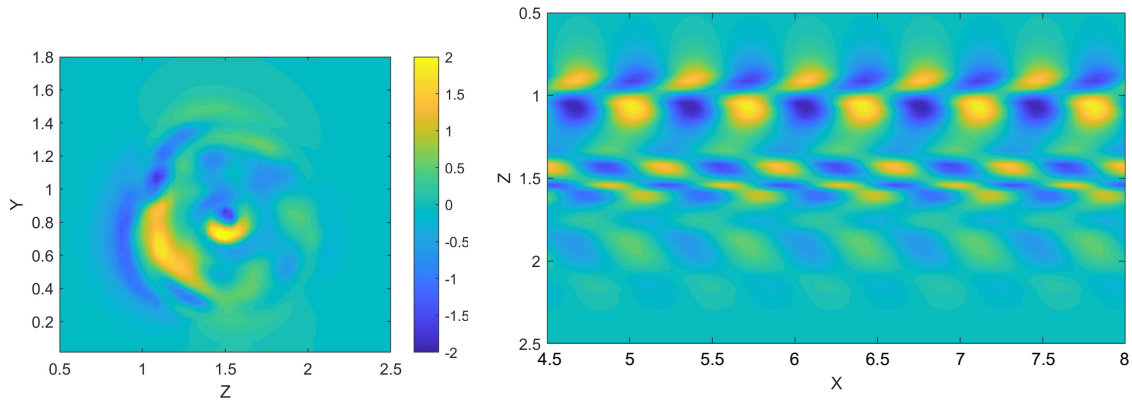

Figure 4.15: Linear superposition of the three main eigenmodes of the energy spectrum at $x = 6.5$ and $\alpha = 9$: streamwise disturbance in the z-y (left) and in the x-z plane (right)

with respect to the tip one (see the right frame of Figure 4.3). Moreover, Fourier transform in the azimuthal direction shows that all of these modes are characterized by main azimuthal wavenumber $m = 1$ (see right frame of Figure 4.14), although the azimuthal Fourier spectrum of mode 3 has a correspondingly high amplitude at $m = 2$ and a weaker peak at $m = 4$. As already noted, the POD mode taken here as reference comprises different structures with a different localization and frequency. Therefore we attempted to reconstruct the POD mode by combining the three least stable modes mentioned above with coefficients $c_1 = 0.25$, $c_2 = 0.15$, $c_3 = 0.6$. Figure 4.15 provides the streamwise velocity contours of this combination, which show a strong resemblance with the overall structure of the third POD mode shown in Figure 4.4.

Figure 4.16 shows the resolvent norm $R(\omega)$, providing the maximum energy gain for a given forcing in the range $6.8 < \omega < 9$. One can notice that the main three peaks correspond to the frequencies of the least stable modes of the eigenspectrum, suggesting a quasi-resonance mechanism at these particular wavenumbers (see [91, 15]). In fact, in some flow cases, the amplification of the external forcing at a given frequency can mostly result from the resonance of a given eigenmode, though other eigenmodes can also contribute to the response, albeit to a lesser extent. In the present case,

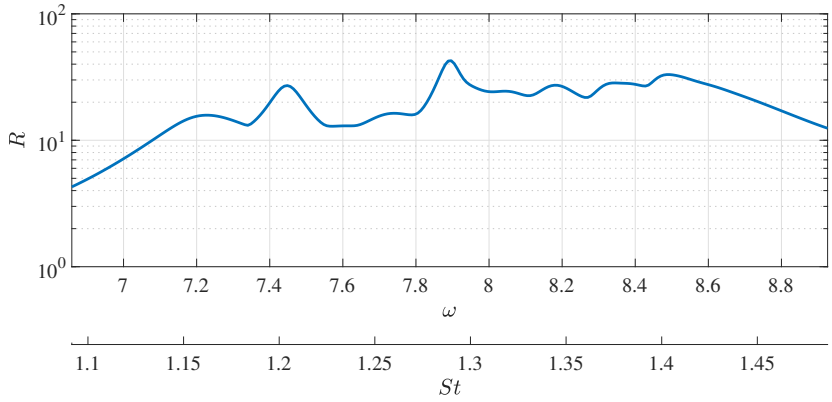

(a) $x = 6.5$

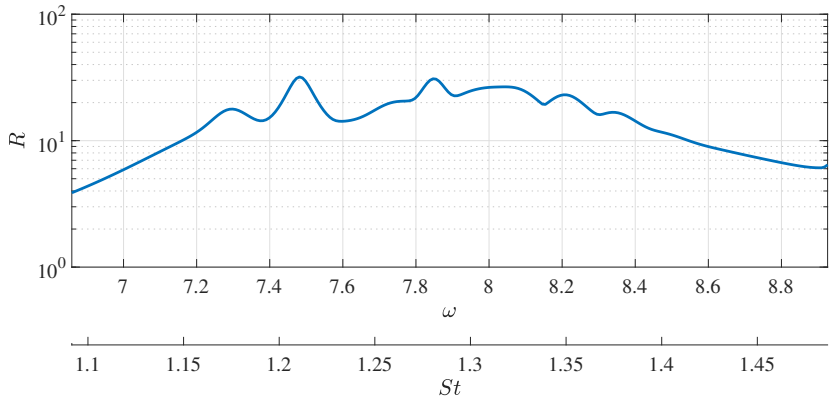

(b) $x = 7.5$

Figure 4.16: Resolvent norm in different cross-sections and $\alpha = 9$.

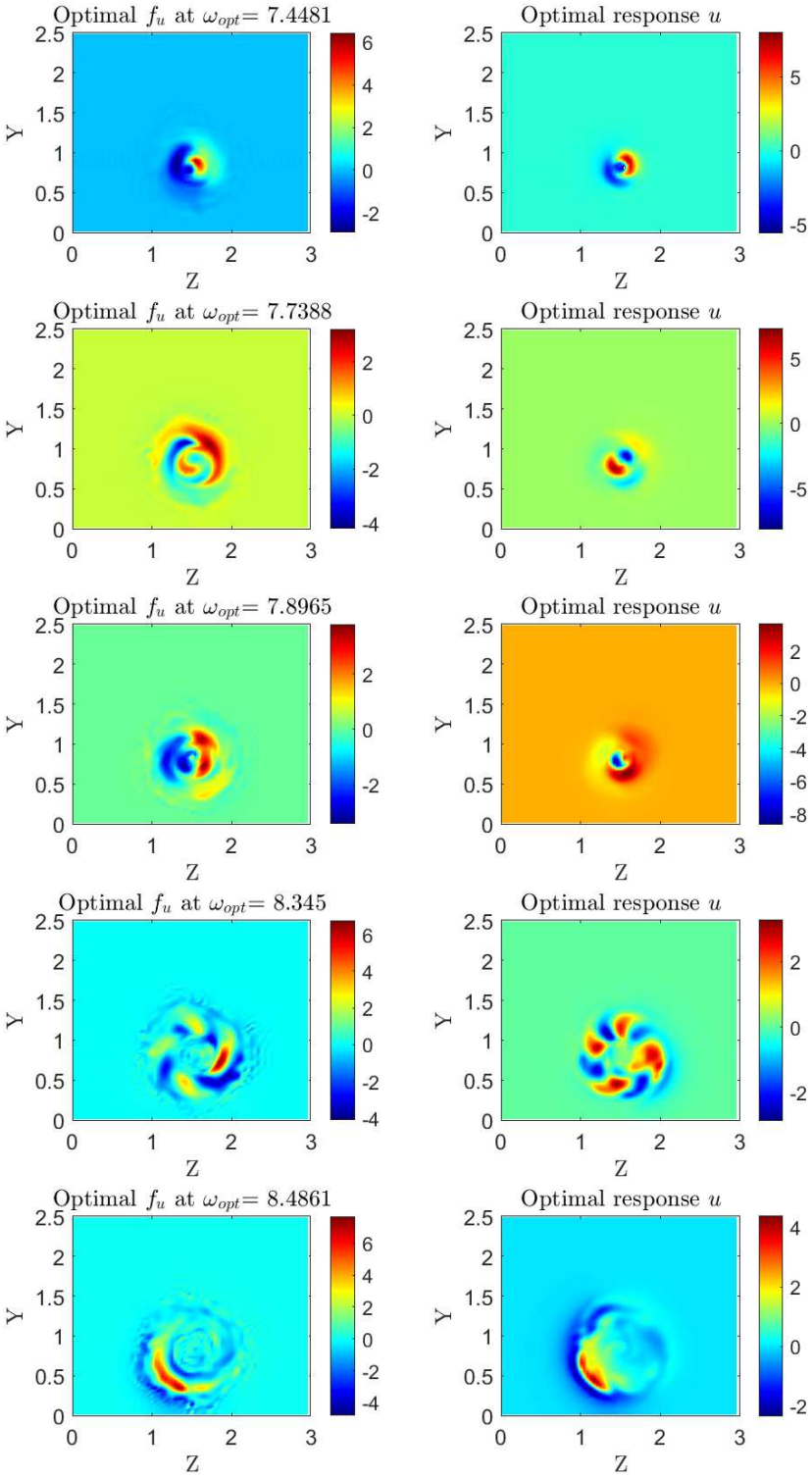

Figure 4.17: Optimal forcing (left) and responses (right) for different frequencies at $x = 6.5$ and $\alpha = 9$.

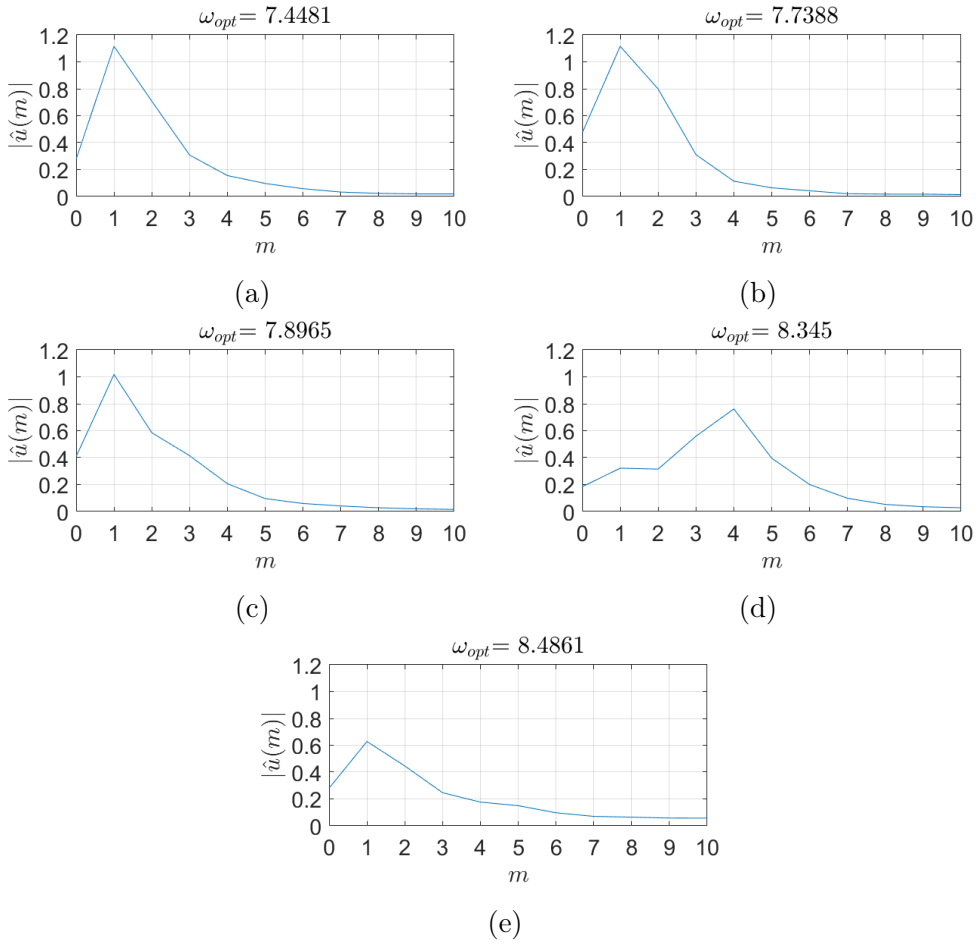

Figure 4.18: Fourier transform in the azimuthal direction for the optimal responses at different frequencies indicated within the plots for $x = 6.5$ and $\alpha = 9$.

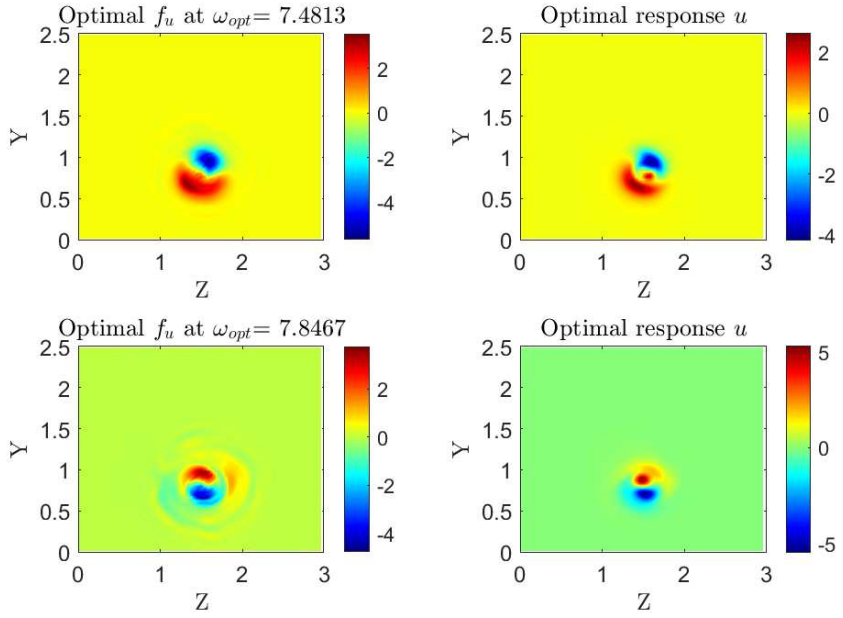

Figure 4.19: Optimal forcing (left) and responses (right) for different frequencies at $x = 7.5$ and $\alpha = 9$

the main resolvent peak is found for $\omega = 7.8$, providing a gain of $R(\omega = 7.8) \approx 40$, although harmonic perturbations with slightly larger or smaller ω are also amplified more than one order of magnitude. Looking at the optimal forcing and responses at the different frequencies corresponding to the several peaks of the resolvent norm, provided in Figure 4.17, one can see that the three most amplified harmonic responses ($\omega = 7.44, 7.89, 8.48$ in the first, third and bottom row) are very similar to the eigenmodes with the same frequencies recovered by stability analysis. This feature is a clear sign of the existence of a quasi-resonance mechanism at those particular frequencies. As shown in Figure 4.18*a-c-e*, all of these responses have main azimuthal wavenumber $m = 1$, which corresponds to the peak wavenumber of the main POD modes. At intermediate forcing frequencies, rather different flow structures are found, with main azimuthal wavenumber ranging from $m = 1$ to $m = 4$ (see Figure 4.18 (b-d)), which are however less amplified. A very similar behaviour is found in different cross-sections further downstream. Figure 4.16 (b) shows the resolvent norm in the cross-section $x = 7.5$ for the same value of α. As before, the resolvent norm

peaks at the frequencies of the least stable modes of the corresponding eigenspectrum (not shown), indicating once again a quasi-resonance mechanism. Moreover, the most amplified optimal responses are similar to those found at $x = 6.5$, characterized by very low azimuthal wavenumber ($m = 1 - 2$, as for the main POD modes) as shown in Figure 4.19.

In conclusion, it appears that the local stability analysis can provide some information about the main wavenumbers and structures within the flow when carried out sufficiently close to the rotor. In that sense those large coherent structures can be approximated by linear modelling, thus enabling - for instance - control design in combination with the information obtained by perusing the localisation of the optimal forcing. We also observe that in the far wake, stability analysis does not predict the main frequency and spatial content of the flow; this can be due to the caveats of the linear model as well as to the limited extent of the domain behind the turbine. We further analyse the linear model by means of resolvent analysis and show that, if forced appropriately, linearly stable modes can be effectively amplified, and detected in the flow. Therefore, it appears that in convective flows as a wind turbine wake, flow structures arising upstream can determine also the most amplified frequencies downstream. This suggests that the frequency content of the nonlinear forcing $\mathbf{f}$ (which is often assumed being a white-noise) may be a key factor in determining the emerging flow structures in this types of flows.

4.5 Conclusions

We carried out a linear analysis of the wake developing past a wind turbine. We considered a numerical snapshots computed by Large-Eddy-Simulation using the actuator line technique to simulate the rotor, at $Re = 6.3 \times 10^5$. Proper orthogonal decomposition analysis is applied for detecting the coherent structures developing in the flow. These modes are applied here for benchmarking the linear modelling. More precisely, two-dimensional linear stability and optimal forcing analyses have been used at different cross-flow planes along the streamwise direction. The resulting spatial structures at each frequency is compared with the most energetic coherent structures recovered by POD analysis.

In the closest planes to the rotor (3 to 6 diameters), the main POD modes are characterized by rather high values of the temporal and streamwise angular frequency $\alpha = 6 - 10$, and azimuthal wavenumber $m = 1$. These structures, mostly located in the root and tip vortices regions, are characterized by slightly different wavenumbers in the inner and in the outer part of the wake. These structures are recovered in the modal stability analysis: close to the rotor, the unstable modes are mostly located in the outer part of the wake and have a frequency content consistent with that of the most energetic POD modes. The growth rate of these modes decreases while moving far from the rotor. In the far wake, however, unstable branches identify structures characterized by lower streamwise wavenumbers and higher azimuthal wavenumbers, losing resemblance with respect of the identified POD. We further explore the spectral content of the POD modes, by considering optimal forcing and response obtained by the resolvent analysis. In particular, we considered a far-wake cross section at the characteristic streamwise frequency of the third POD mode, namely $\alpha = 9$, where the mean flow results linearly stable. The response gain showed three distinct frequencies correspondent to three barely stable modes. The two linear modes with lower ω are localised at the wake core, wheareas the mode with a higher ω is mostly localised of the wake shear layer. Moreover, the combination of these three linear modes re-

sembles the third POD mode, taken as reference. Optimal forcing analysis shows, therefore, that these asymptotically stable modes can be amplified by more than one order of magnitude by means of a quasi-resonance mechanism, being able to bypass the growth of the most unstable modes recovered in the far wake. This suggests a scenario in which the coherent structures within the wake are mostly originated by modal instability mechanisms close to the rotor, generating waves of selected frequencies able to trigger a high flow response downstream. The author aims at verifying this conjecture performing an analysis more tailored to the purpose in future works.

Chapter 5

Data driven modal analysis of a utility-scale wind turbine wake

5.1 Introduction

In this chapter the wake produced by a utility-scale wind turbine invested by a laminar, uniform inflow is analyzed. The turbine considered is the NREL-5MW [50] and its size leads to a Reynolds number of the order of 10^8, which together with a higher tip-speed ratio can lead to a different wake dynamics with respect to that analyzed in the previous chapters. The wake flow is analyzed using both Proper Orthogonal Decomposition (POD) and Dynamic Mode Decomposition in its sparsity-promoting variant (SP-DMD), described in sections 3.4 and 2.7, respectively.

5.2 Simulation setup

The computational box and boundary conditions are the same used for the simulations analyzed in chapter 3. The geometrical characteristics of the turbine considered here are summarized in table 5.1. The turbine is simulated at rated conditions with tip-speed ratio $\lambda = 7$, which implies a constant dimensionless angular frequency of

Table 5.1: Geometrical parameters of the NREL 5MW turbine.

Parameter	Value
Hub height	$h = 87.5$ m
Blade length	$R = 61.5$ m
Rotor diameter	$D = 126$ m
Tower mean diameter	$d_t = 5$ m

the rotor $\omega = 2\lambda = 14$. The reference incoming wind speed at rated conditions is $U_\infty = 11.4$ m/s, therefore the resulting diameter-based Reynolds number is $Re \approx 10^8$.

5.3 Proper orthogonal decomposition

The proper orthogonal decomposition is carried out on a dataset made by M = 3051 snapshots of the velocity field in a subdomain enclosing the wake, whose extent is $[0\ \ 8.4] \times [-0.7\ \ 0.63] \times [0.8\ \ 2.2]$ in x,y and z direction, respectively. The velocity components have been downsampled with a ratio 1:5 with respect to the computational grid and the sampling frequency is such that 36 snapshots correspond to a complete rotation of the rotor. Moreover, the ensemble mean, shown in Figure 5.1, has been subtracted from each snapshot. The latter shows a weaker effect of the tower on the wake, with respect to the case analyzed in Chapter 3. In this case, indeed, the wake does not show a strong asymmetry between the left and the right side, being almost axisymmetric. This behavior can be due to the reduced tower's diameter, but also to the higher tip-speed ratio and Reynolds number, which accelerating the tip-vortices breakdown, prevents the latter to interact with the vortices shed by the tower. The decomposition has been performed using the snapshots' method [96]. In figure 5.2(a) the distribution of the singular values is shown. It can be observed a fast energy decay for the first 2-3 hundreds of modes; then the slope of the curve decreases and a nearly null energy is reached for $k \approx 2500$. A closer look to the singular values for the first 20 POD modes highlights a step-wise distribution, suggesting that successive modes

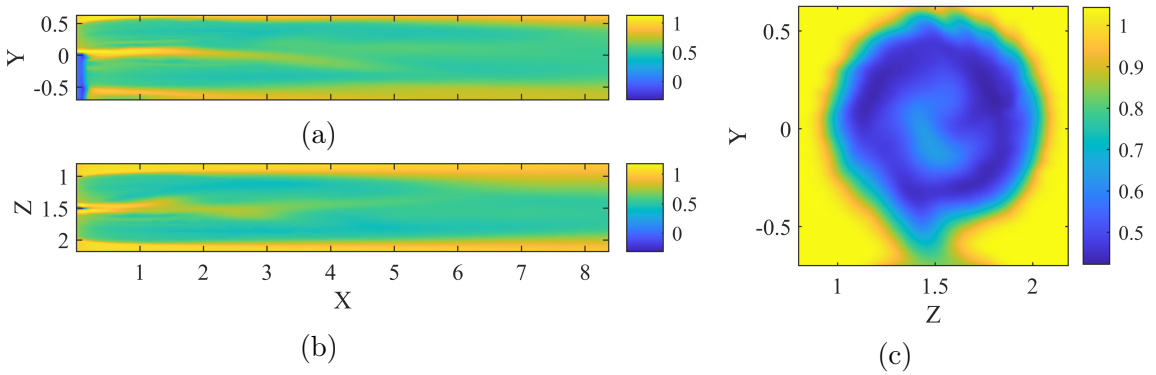

Figure 5.1: Streamwise velocity contours of the snapshots' ensemble mean. (a) x-y plane at $z = 1.5$. (b) x-z plane at $y = 0$. (c) z-y plane at $x = 4$.

characterized by a similar energy are paired, as observed in chapter 3. Figure 5.2(b) shows the cumulative percentage distribution of turbulent kinetic energy against the fraction of POD modes considered, computed as:

$$\overline{k}[\%] = \frac{\sum_{k=1}^{m} s_k}{\sum_{k=1}^{M} s_k} \times 100 \quad m \in \{1, \ldots, M\} \tag{5.1}$$

$$\text{modes}[\%] = \frac{m}{M} \times 100. \tag{5.2}$$

Fifty percent of the turbulent kinetic energy is due to only 15% of POD modes ($\sim$ 457 modes), and 50% of modes ($\sim$ 1525 modes) accounts for about 90% of the turbulent kinetic energy. The most energetic POD modes are shown in figure 5.3. The first pair (figure 5.3(a)) corresponds to the 4th harmonic of the tip vortices (figure 5.3(b)). The second and third pair are harmonics of the tip vortices as well (not shown). Mode 9 in figure 5.3(c) is representative of the fitfh pair and it is mostly concentrated in the region between the near wake and the turbulent far wake. For this reason the fifth pair is possibly related to an instability mechanism, causing tip vortices' breakdown. The vortex shedding caused by presence of the tower is captured in the following three pairs (figures 5.3(d-f)). Many of the remaining modes are very similar to the 13th mode (figure 5.3(e)), with a small-scale and almost featureless structure far from the rotor; however low-frequency large-scale coherent motions, though characterized by

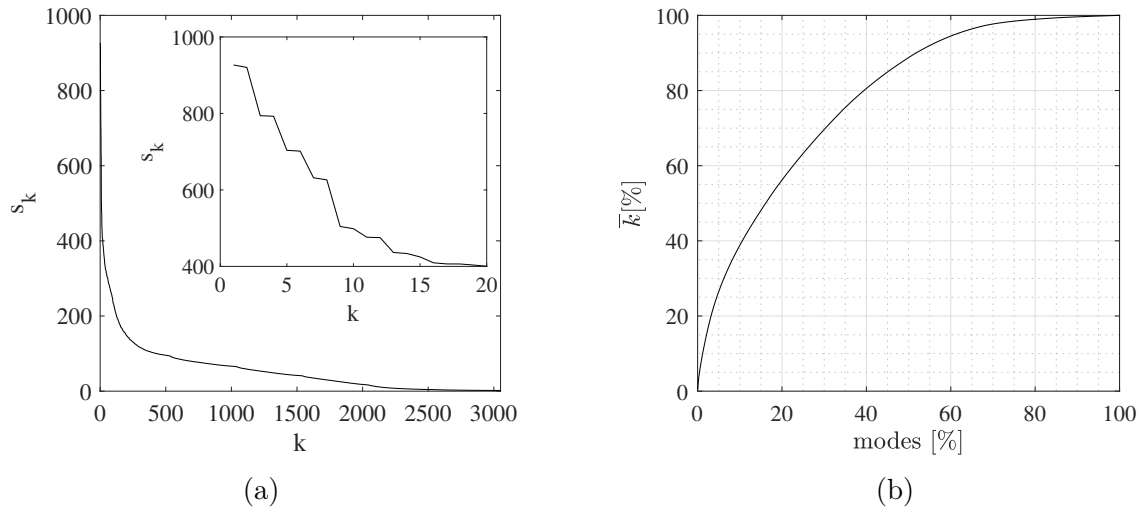

Figure 5.2: (a)Singular values distribution with a close-up for the first 20 modes. (b) Cumulative turbulent kinetic energy distribution against the fraction of POD modes.

low amplitude, are also recovered (see figure 5.4).

5.4 Dynamic mode decomposition

The Dynamic Mode Decomposition is performed on the same dataset analyzed using the POD. The latter, in fact, represents a preliminary step for the computation of dynamic modes, as explained in section 2.7. In particular the dynamic modes are computed onto a low-dimensional subspace consisting of the first 251 POD modes. The selected value of sparsity-promoting parameter is $\gamma = 40000$. This particular choice has led to the nontrivial selection of just 14 relevant dynamic modes. In the left panel of Figure 5.5 the eigenvalues μ of the linear operator $\boldsymbol{F}$ (see equations (2.47) and (2.48)) are shown, along with the unit circle. The selected modes by the sparsity-promoting algorithm are marked with a black circle. As expected for a turbulent statistically stationary flow, all eigenvalues are very close to the unit circle, describing the purely periodic dynamics of the associated modes. It is noticeable, furthermore, an unbalance between high- and low-frequency modes, the high-frequency ones being only the harmonics of tip vortices, since their frequencies are multiples of the tip

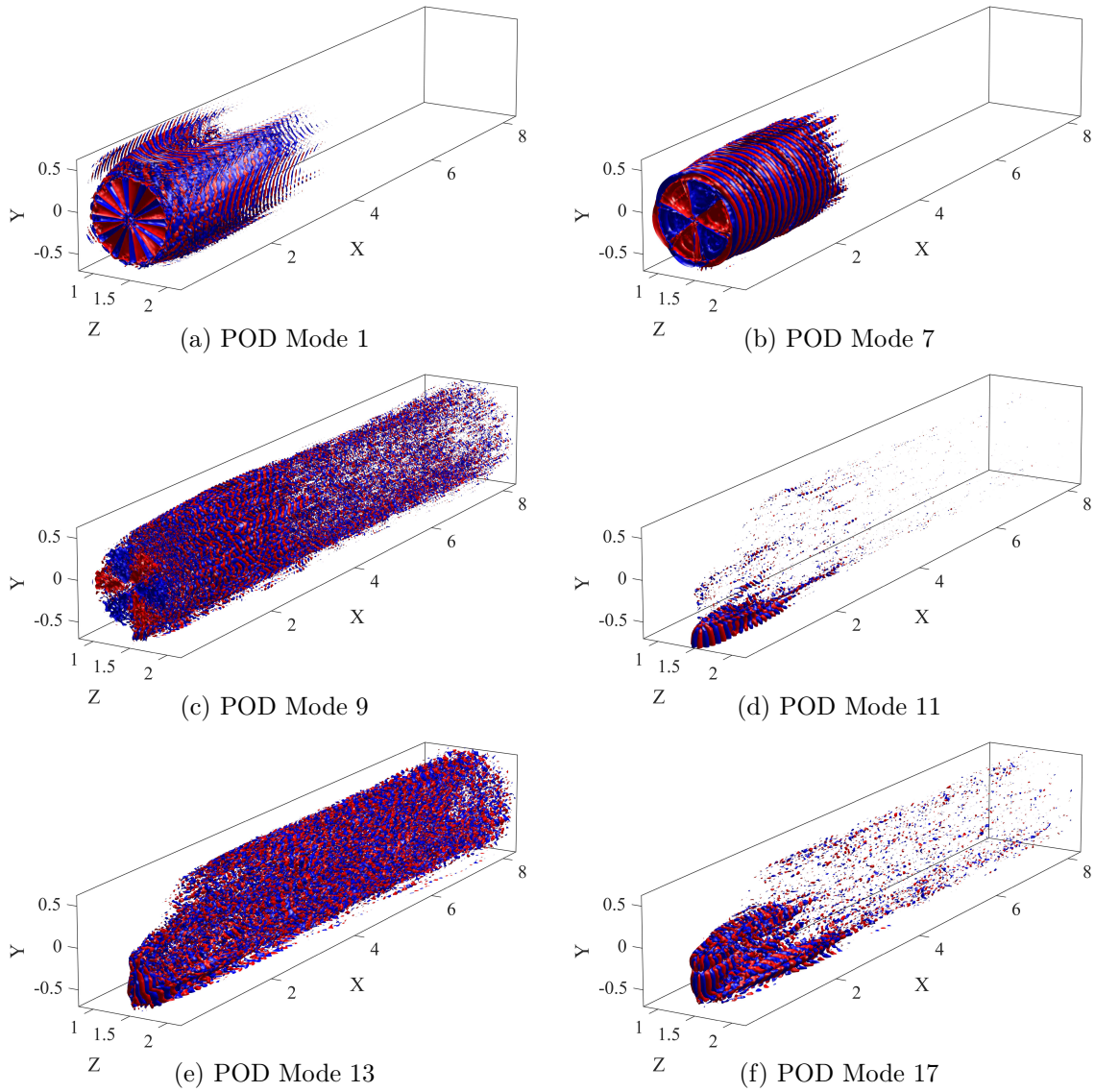

(a) POD Mode 1 (b) POD Mode 7

(c) POD Mode 9 (d) POD Mode 11

(e) POD Mode 13 (f) POD Mode 17

Figure 5.3: Streamwise velocity iso-surfaces of relevant POD modes (red for positive, blue for negative values).

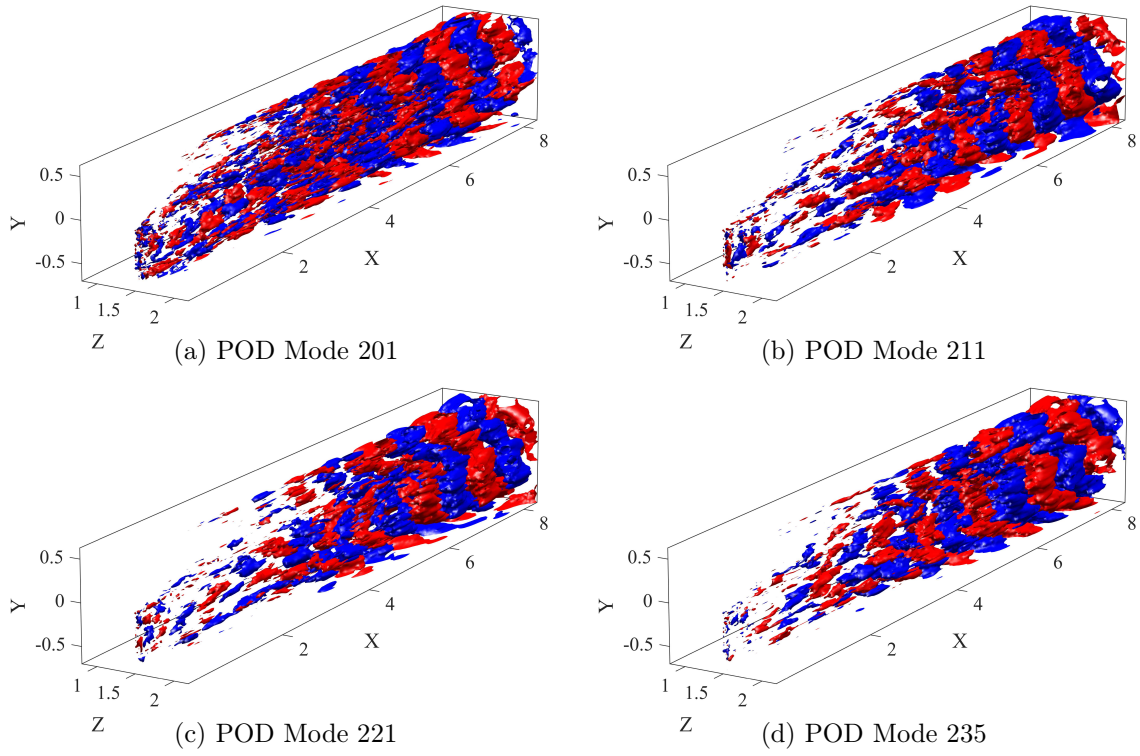

(a) POD Mode 201 (b) POD Mode 211

(c) POD Mode 221 (d) POD Mode 235

Figure 5.4: Streamwise velocity iso-surfaces of POD modes with large-scale structure (red for positive, blue for negative values).

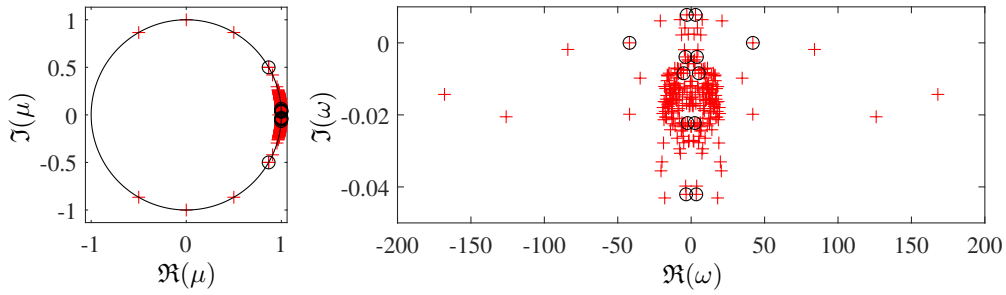

Figure 5.5: Eigenvalues resulting from the standard DMD algorithm (red crosses) and the sparsity promoting algorithm (black circles). The right panel shows the logarithmic mapping of the eigenvalues, $\omega = -\frac{log(\mu)}{i\Delta t}$ where Δt is the temporal separation between two consecutive snapshots and i the imaginary unit.

Table 5.2: Frequencies and amplitudes of the selected complex conjugate dynamic modes' pairs, computed with the standard and sparsity-promoting DMD.

	$\Re(\omega)$	$\|\alpha\|$ (std. DMD)	$\|\alpha\|$ (S-P DMD)
Pair 1	42	178.5	24.01
Pair 2	3.586	340.4	5.875
Pair 3	3.45	353	3.563
Pair 4	3.917	308	3.118
Pair 5	2.96	348.3	2.592
Pair 6	2.472	114.7	2.246
Pair 7	5.205	362.8	0.7402

vortices' frequency. The right panel of Figure 5.5 shows the logarithmic mapping of the eigenvalues, computed according to $\omega = -\frac{log(\mu)}{i\Delta t}$ where Δt is the temporal separation between two consecutive snapshots and i the imaginary unit. Since the analyzed dataset is real, the latter eigenvalues' spectrum is clearly symmetric with respect to the imaginary axis: the eigenvalues with non-zero frequency form complex conjugate pairs, and so do the associated dynamic modes. Therefore, the 14 dynamic modes selected by the sparsity-promoting DMD consist of 7 complex conjugate pairs. Some low-frequency modes seem being slightly unstable; however this behavior is not physical, more likely it is due to the limited time window spanned by the entire dataset, which is insufficient for capturing low-frequency modes accurately. Frequencies and amplitudes of the selected dynamic modes' pairs are summarized in Table 5.2. The amplitudes of the dynamic modes $|\alpha_i|$ (see equation (2.53) are shown in Figure 5.6,

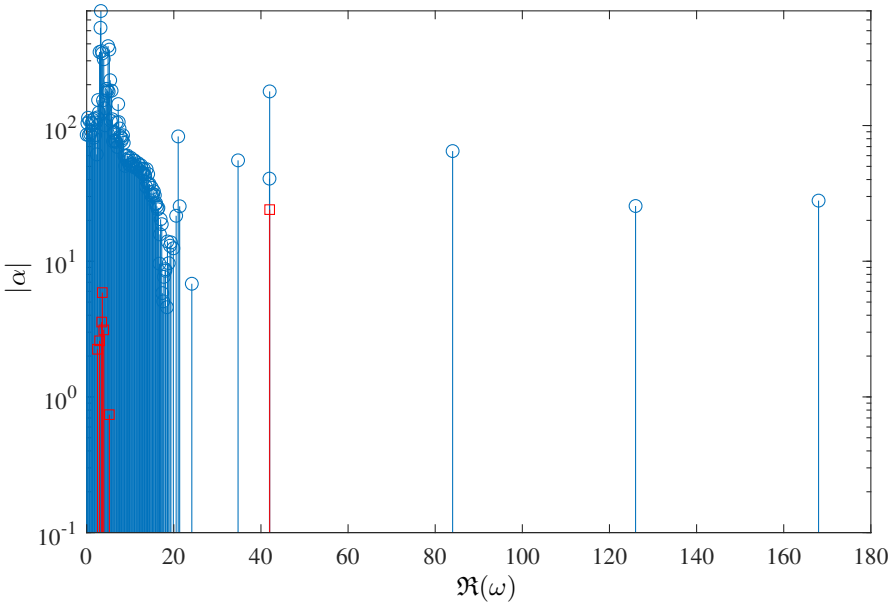

Figure 5.6: Dependence of the absolute value of the DMD amplitudes α_i on the angular frequency $\Re(\omega)$. The results are obtained using the standard (blue stems) and the sparsity-promoting algorithm (red stems). Due to the symmetry of amplitudes' distribution, only positive frequencies are shown.

which compares the results of the standard DMD algorithm (blue stems) with the results of the sparsity-promoting DMD algorithm (red stems). Among the modes selected by the SP-DMD, the ones having the largest amplitude correspond to the tip vortices (see Figure 5.7(a)) and, in fact, oscillate at a characteristic angular frequency $\omega = 42$, equal to three times the rotational angular frequency of the turbine. It is interesting to note that the remaining selected modes are characterized by low frequencies and large-scale spatial structures, as can be observed in Figure 5.7(b-g). This is in contrast with POD analysis, where large-scale structures are ranked low, and, therefore, not considered energetically relevant. The different outcomes of the POD and the sparsity-promoting DMD are justified and discussed in the following concluding section.

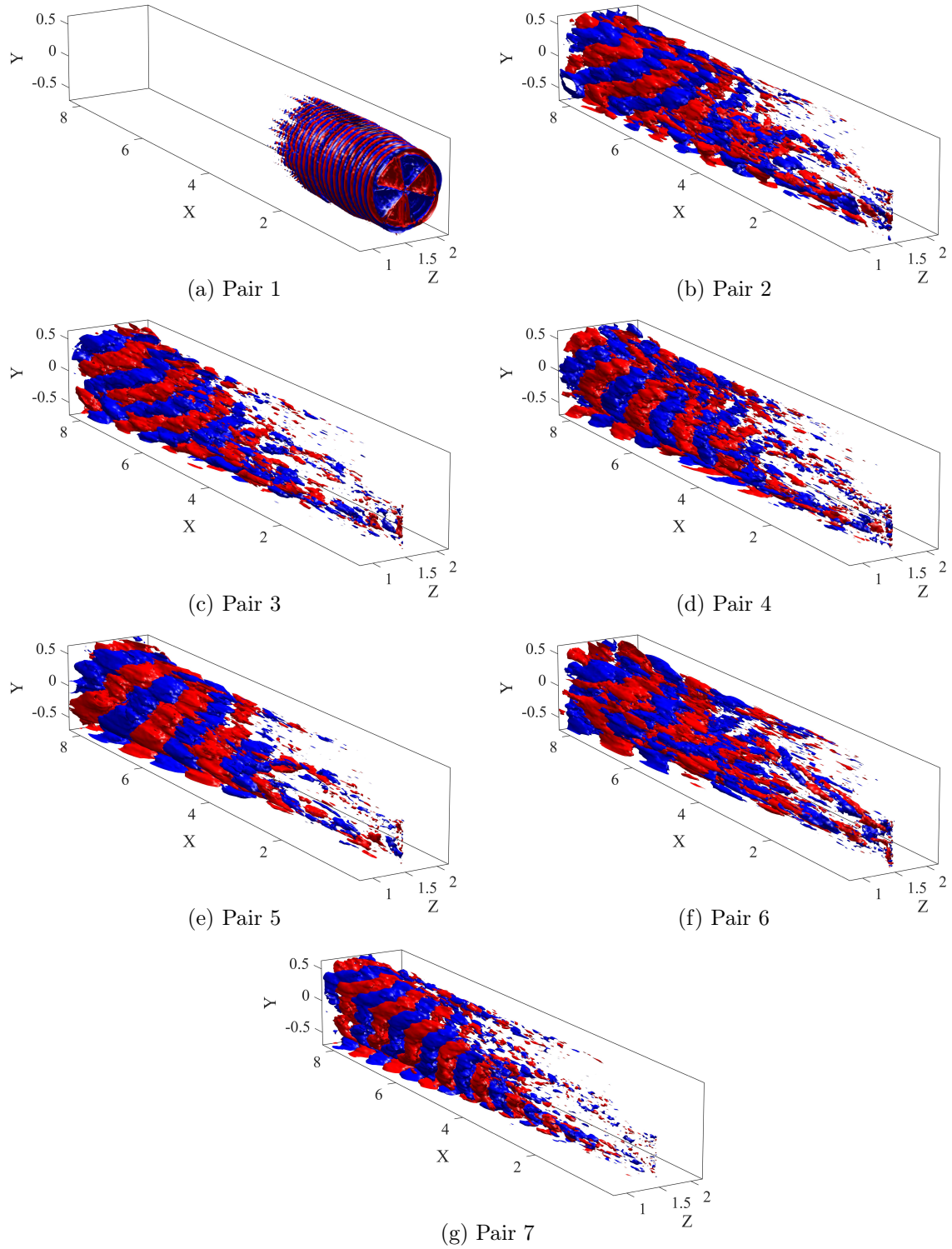

(a) Pair 1

(b) Pair 2

(c) Pair 3

(d) Pair 4

(e) Pair 5

(f) Pair 6

(g) Pair 7

Figure 5.7: Streamwise velocity iso-surfaces (red for positive, blue for negative values) of the real part of the 7 dynamic modes' pairs selected by the sparsity-promoting algorithm, ordered according to their amplitude $|\alpha|$.

5.5 Conclusions

In this chapter, the wake produced by the reference utility-scale wind turbine NREL 5-MW is analyzed using two modal decomposition techniques, namely the Proper Orthogonal Decomposition (POD) and the Dynamic Mode Decomposition (DMD). The POD generates orthogonal modes that optimally capture the energy of a given dataset. However, the most energetic POD modes may not correspond with the dynamically important ones. Therefore, the selection of the POD basis for a reduced-order model is not trivial. On the other hand, DMD computes eigenvalues and eigenvectors of a linear operator that approximates the underlying nonlinear dynamics. This can be seen, in fact, as an approximation of the Koopman operator. The DMD provides frequencies and growth rates for each mode, and if the data are periodic, the decomposition amounts to Discrete Fourier Transform (DFT) [82]. However, even for the DMD, the selection of dynamically relevant modes is not straightforward nor trivial. For this reason the sparsity-promoting DMD (SP-DMD) algorithm is employed for this analysis, which is able to find a set of modes that best approximated the dataset, given a sparsity constraint. The results show a quite different behavior of the two methods. The POD analysis appears to be biased toward near-wake, high-frequency modes, as the tip vortices and, in particular, their harmonics. The SP-DMD still selects the tip vortices in the wake, but also a set of large-scale coherent structures in the far wake. According to the POD, the latter are characterized by a low energy, but nevertheless, SP-DMD proves they are dynamically relevant. The difference between the two modal-decomposition techniques points out that POD may not be suitable for obtaining a low-dimensional model of a turbulent wind turbine wake and sparsity-promoting DMD should be preferred.

Chapter 6

Final remarks

In the present thesis the study of wind turbines wakes has been approached using data-driven modal-decomposition techniques and meanflow linear analysis.

Large Eddy Simulations of a model wind turbine at moderate Reynolds number and tip-speed ratio $\lambda = 3$ were performed, using the Actuator Line Method to model the aerodynamic forces exerted by the blades and the Immersed Boundary Method to simulate the tower and nacelle. The turbine was simulated with and without tower and nacelle, and the Proper Orthogonal Decomposition of three-dimensional velocity data allowed us to isolate the most energetic coherent structures characterizing the two cases. The analysis of time-averaged flow fields and POD modes showed that the vortex-shedding from tower and nacelle, interacting with the tip-vortex helices, leads to a marked asymmetry of the wake and a faster recovery. A further insight into the effect of tower and nacelle on wake recovery was provided by computing the contribution of each POD mode to mean-kinetic-energy flux through a cylindrical surface enclosing the wake. It was found that tip-vortices and their harmonics have a negative impact on wake recovery, whereas coherent structures generated by the presence of tower and nacelle, as the von Kármaán vortex street and oscillations produced by its interaction with tip vortives, promote the recovery of the wake.

The physical origin of coherent structures isolated by the Proper Orthogonal Decom-

position in the case without tower and nacelle was then investigated. In order to do so, a linear stability and optimal forcing analysis were performed on the meanflow. In particular the quasi-parallel hypothesis was made and the flow was analyzed by means of bilocal stability analysis in cross-flow planes at different locations along the streamwise direction. The effect of turbulent fluctuations was taken into account by modeling the Reynolds stress using the frozen eddy-viscosity approach. Most unstable (amplified) modes were compared with POD modes and, despite lacking in predictive abilities, linear analysis of the meanflow has proved to be well suited to model some of the structures arising in the far wake.

Finally, the wake produced by a utility-scale wind turbine at high Reynolds number and tip-speed ratio $\lambda = 7$ was analyzed using the Proper Orthogonal Decomposition and the Dynamic Mode Decomposition, in its sparsity-promoting variant. A visual analysis of the snapshots' ensemble highlighted a different dynamics with respect to the model wind turbine. In particular, in this case, the wake remains substantially straight and axisymmetric, despite the presence of tower. The most energetic POD modes were relative to the tip-vortices dynamics, the breakdown of which did not seem to be not related to the interaction with tower's wake. The tower's wake characteristic flow structures were also captured by the first POD modes. Large-scale coherent structures arising in the far wake were, instead, not present among the most energetic modes. The sparsity-promoting dynamic mode decomposition, performed on the same dataset, selected a non-trivial limited subset of dynamic modes that optimally reconstruct the entire data sequence. In particular a pair of dynamic modes related to the tip vortices was selected, but, in contrast to POD, the remaining selected dynamic modes captured low-frequency large-scale coherent structures arising in the far wake. The latter result suggests that an energy-based criterion, like POD, may not be the more suitable for formulating a reduced-order model of wind turbine wake, and the sparsity-promoting DMD should be preferred for finding a low-dimensional representation of flow data.

Scientific production

International conferences

- G. De Cillis, S. Cherubini, O. Semeraro, S. Leonardi, P. De Palma
  Coherent structures in a wind turbine wake: POD and stability analysis
  17th European Turbulence Conference, 2019

- G. De Cillis, S. Cherubini, O. Semeraro, S. Leonardi, P. De Palma
  POD analysis of the recovery process in wind turbine wakes
  Torque, 2020

Papers

- G. De Cillis, S. Cherubini, O. Semeraro, S. Leonardi, P. De Palma
  POD-based analysis of a wind turbine wake under the influence of tower and nacelle
  [Accepted for publication]. *Wind Energy, 2020*

- G. De Cillis, S. Cherubini, O. Semeraro, S. Leonardi, P. De Palma
  Stability and optimal forcing analysis of a wind turbine wake: comparison with POD
  [Submitted for publication]. *Physical Review Fluids, 2020*

Proceedings

- G. De Cillis, S. Cherubini, O. Semeraro, S. Leonardi, P. De Palma
  POD analysis of the recovery process in wind turbine wakes
  Journal of Physics: Conference Series **1618** 062016

- G. De Cillis, S. Cherubini, O. Semeraro, S. Leonardi, P. De Palma
  Data driven modal decomposition of the wake behind a NREL 5-MW wind turbine
  [Submitted for publication]. *Proceedings of 14th European Conference on Turbomachinery Fluid dynamics & Thermodynamics, 2021*

Bibliography

[1] Aitken, M. L., and Lundquist, J. K. Utility-scale wind turbine wake characterization using nacelle-based long-range scanning lidar. *J. Atmos. Ocean. Technol. 31*, 7 (2014), 1529–1539.

[2] Ali, N., Cortina, G., Hamilton, N., Calaf, M., and Cal, R. Turbulence characteristics of a thermally stratified wind turbine array boundary layer via proper orthogonal decomposition. *J. Fluid Mech. 828* (2017), 175–195.

[3] Ali, N., Hamilton, N., DeLucia, D., and BayoÃąn Cal, R. Assessing spacing impact on coherent features in a wind turbine array boundary layer. *Wind Energy Sci. 3*, 1 (2 2018).

[4] Andersen, S. J., Sørensen, J. N., and Mikkelsen, R. Simulation of the inherent turbulence and wake interaction inside an infinitely long row of wind turbines. *J. Turbul. 14*, 4 (2013), 1–24.

[5] Ashton, R., Viola, F., Camarri, S., Gallaire, F., and Iungo, G. V. Hub vortex instability within wind turbine wakes: Effects of wind turbulence, loading conditions, and blade aerodynamics. *Phys. Rev. Fluids 1* (Nov 2016), 073603.

[6] Ashton, R., Viola, F., Gallaire, F., and Iungo, G. V. Effects of incoming wind condition and wind turbine aerodynamics on the hub vortex instability. *J. Phys. Conf. Ser. 625* (jun 2015), 012033.

[7] BAGHERI, S. Koopman-mode decomposition of the cylinder wake. *J. Fluid Mech. 726* (2013), 596–623.

[8] BARKLEY, D. Linear analysis of the cylinder wake mean flow. *EPL 75*, 5 (2006), 750.

[9] BARTHELMIE, R. J., FRANDSEN, S. T., NIELSEN, M., PRYOR, S., RETHORE, P.-E., AND JØRGENSEN, H. E. Modelling and measurements of power losses and turbulence intensity in wind turbine wakes at middelgrunden offshore wind farm. *Wind Energy 10*, 6 (2007), 517–528.

[10] BARTL, J. M. S., AND SÆTRAN, L. R. Blind test comparison of the performance and wake flow between two in-line wind turbines exposed to different turbulent inflow conditions. *Wind Energy Sci.* (2017).

[11] BASTINE, D., VOLLMER, L., WÄCHTER, M., AND PEINKE, J. Stochastic wake modelling based on pod analysis. *Energies 11*, 3 (2018), 612.

[12] BASTINE, D., WITHA, B., WÄCHTER, M., AND PEINKE, J. Towards a simplified dynamicwake model using pod analysis. *Energies 8*, 2 (2015), 895–920.

[13] BERKOOZ, G., HOLMES, P., AND LUMLEY, J. L. The proper orthogonal decomposition in the analysis of turbulent flows. *Annu. Rev. Fluid Mech. 25*, 1 (1993), 539–575.

[14] BP. Bp statistical review of world energy. Tech. rep., British Petroleum, 2017.

[15] BUCCI, M. A., PUCKERT, D., ANDRIANO, C., LOISEAU, J.-C., CHERUBINI, S., ROBINET, J.-C., AND RIST, U. Roughness-induced transition by quasi-resonance of a varicose global mode. *J. Fluid Mech.* (2017).

[16] CAL, R. B., LEBRÓN, J., CASTILLO, L., KANG, H. S., AND MENEVEAU, C. Experimental study of the horizontally averaged flow structure in a model

wind-turbine array boundary layer. *J. Renew. Sustain. Energy 2*, 1 (2010), 013106.

[17] CHEN, K. K., TU, J. H., AND ROWLEY, C. W. Variants of dynamic mode decomposition: boundary condition, koopman, and fourier analyses. *J. Nonlinear Sci. 22*, 6 (2012), 887–915.

[18] CHURCHFIELD, M. J., SCHRECK, S., MARTÍNEZ-TOSSAS, L. A., MENEVEAU, C., AND SPALART, P. R. An advanced actuator line method for wind energy applications and beyond. *35th Wind Energy Symposium, 2017*, January (2017), 1–20.

[19] CIRI, U., PETROLO, G., SALVETTI, M. V., AND LEONARDI, S. Large-eddy simulations of two in-line turbines in a wind tunnel with different inflow conditions. *Energies 10*, 6 (2017), 821.

[20] CIRI, U., ROTEA, M. A., AND LEONARDI, S. Model-free control of wind farms: A comparative study between individual and coordinated extremum seeking. *Renew. Energy 113* (2017), 1033–1045.

[21] CIRI, U., SALVETTI, M., CARRASQUILLO, K., SANTONI, C., IUNGO, G., AND LEONARDI, S. Effects of the subgrid-scale modeling in the large-eddy simulations of wind turbines. In *Direct and Large-Eddy Simulation X*. Springer, 2018, pp. 109–115.

[22] COSSU, C. Evaluation of tilt control for wind-turbine arrays in the atmospheric boundary layer. *Wind Energ. Sci. Discuss. 2020* (2020), 1–16.

[23] COSSU, C. Replacing wakes with streaks in wind turbine arrays. *arXiv preprint arXiv:2007.01617* (2020).

[24] COURANT, R., FRIEDRICHS, K., AND LEWY, H. On the partial difference equations of mathematical physics. *IBM J. Res. Dev. 11*, 2 (1967), 215–234.

[25] DE TULLIO, MARCO, D., DE PALMA, P., IACCARINO, G., PASCAZIO, G., AND NAPOLITANO, M. An immersed boundary method for compressible flows using local grid refinement. *J. Comput. Phys. 225*, 2 (2007), 2098–2117.

[26] DEBNATH, M., SANTONI, C., LEONARDI, S., AND IUNGO, G. V. Towards reduced order modelling for predicting the dynamics of coherent vorticity structures within wind turbine wakes. *Philos. Trans. Royal Soc. A 375* (2017).

[27] FERRER, E., BROWNE, O., AND VALERO, E. Sensitivity analysis to control the far-wake unsteadiness behind turbines. *Energies 10*, 10 (Oct 2017), 1599.

[28] FORTES-PLAZA, A., CAMPAGNOLO, F., WANG, J., WANG, C., BOTTASSO, C., ET AL. A pod reduced-order model for wake steering control. In *J. Phys. Conf. Ser.* (2018), vol. 1037.

[29] FOTI, D., YANG, X., GUALA, M., AND SOTIROPOULOS, F. Wake meandering statistics of a model wind turbine: Insights gained by large eddy simulations. *Phys. Rev. Fluids 1*, 4 (2016), 044407.

[30] FOTI, D., YANG, X., SHEN, L., AND SOTIROPOULOS, F. Effect of wind turbine nacelle on turbine wake dynamics in large wind farms. *J. Fluid Mech. 869* (2019), 1–26.

[31] GIANNETTI, F., AND LUCHINI, P. Structural sensitivity of the first instability of the cylinder wake. *J. Fluid Mech. 581*, 1 (2007), 167–197.

[32] GÓMEZ, F., BLACKBURN, H., RUDMAN, M., SHARMA, A., AND MCKEON, B. A reduced-order model of three-dimensional unsteady flow in a cavity based on the resolvent operator. *J. Fluid Mech. 798* (2016).

[33] GUDMUNDSSON, K., AND COLONIUS, T. Instability wave models for the near-field fluctuations of turbulent jets. *J. Fluid Mech. 689* (2011), 97–128.

[34] GUPTA, V., AND WAN, M. Low-order modelling of wake meandering behind turbines. *J. Fluid Mech. 877* (2019), 534–560.

[35] HAMILTON, N., TUTKUN, M., AND CAL, R. B. Wind turbine boundary layer arrays for cartesian and staggered configurations: Part ii, low-dimensional representations via the proper orthogonal decomposition. *Wind Energy 18*, 2 (2015), 297–315.

[36] HAMILTON, N., TUTKUN, M., AND CAL, R. B. Low-order representations of the canonical wind turbine array boundary layer via double proper orthogonal decomposition. *Phys. Fluids 28*, 2 (2016), 025103.

[37] HAMILTON, N., TUTKUN, M., AND CAL, R. B. Anisotropic character of low-order turbulent flow descriptions through the proper orthogonal decomposition. *Phys. Rev. Fluids 2* (Jan 2017), 014601.

[38] HAMILTON, N., VIGGIANO, B., CALAF, M., TUTKUN, M., AND CAL, R. B. A generalized framework for reduced-order modeling of a wind turbine wake. *Wind Energy 21*, 6 (2018), 373–390.

[39] HEMATI, M. S., ROWLEY, C. W., DEEM, E. A., AND CATTAFESTA, L. N. Debiasing the dynamic mode decomposition for applied koopman spectral analysis of noisy datasets. *Theor. Comput. Fluid Dyn. 31*, 4 (2017), 349–368.

[40] HEMATI, M. S., WILLIAMS, M. O., AND ROWLEY, C. W. Dynamic mode decomposition for large and streaming datasets. *Phys. Fluids 26*, 11 (2014), 111701.

[41] HYVÄRINEN, A., AND SEGALINI, A. Effects from complex terrain on wind-turbine performance. *J. Energy Resour. Technol. 139*, 5 (2017).

[42] IACCARINO, G., AND VERZICCO, R. Immersed boundary technique for turbulent flow simulations. *Appl. Mech. Rev. 56*, 3 (05 2003), 331–347.

[43] IEA. Global energy & co2 status report 2017. Tech. rep., International Energy Agency, 03 2018.

[44] IEA. Global energy & co2 status report 2018. Tech. rep., International Energy Agency, 03 2019.

[45] ILAK, M., AND ROWLEY, C. W. Modeling of transitional channel flow using balanced proper orthogonal decomposition. *Phys. Fluids 20*, 3 (2008), 034103.

[46] IUNGO, G. V., SANTONI-ORTIZ, C., ABKAR, M., PORTÉ-AGEL, F., ROTEA, M. A., AND LEONARDI, S. Data-driven reduced order model for prediction of wind turbine wakes. In *J. Phys. Conf. Ser.* (2015), vol. 625, IOP Publishing, p. 012009.

[47] IUNGO, G. V., VIOLA, F., CAMARRI, S., PORTÉ-AGEL, F., AND GALLAIRE, F. Linear stability analysis of wind turbine wakes performed on wind tunnel measurements. *J. Fluid Mech. 737* (2013), 499–526.

[48] IUNGO, G. V., WU, Y.-T., AND PORTÉ-AGEL, F. Field measurements of wind turbine wakes with lidars. *J. Atmos. Ocean. Technol. 30*, 2 (2013), 274–287.

[49] IVANELL, S., MIKKELSEN, R., SØRENSEN, J. N., AND HENNINGSON, D. Stability analysis of the tip vortices of a wind turbine. *Wind Energy 13*, 8 (2010), 705–715.

[50] JONKMAN, J., BUTTERFIELD, S., MUSIAL, W., AND SCOTT, G. Definition of a 5-mw reference wind turbine for offshore system development. Tech. rep., National Renewable Energy Lab.(NREL), Golden, CO (United States), 2009.

[51] JOVANOVIĆ, M. R., SCHMID, P. J., AND NICHOLS, J. W. Sparsity-promoting dynamic mode decomposition. *Phys. Fluids 26*, 2 (2014), 024103.

[52] KANG, S., YANG, X., AND SOTIROPOULOS, F. On the onset of wake meandering for an axial flow turbine in a turbulent open channel flow. *J. Fluid Mech. 744* (2014), 376–403.

[53] KIM, J., AND MOIN, P. Application of a fractional-step method to incompressible navier-stokes equations. *J. Comput. Phys. 59*, 2 (1985), 308–323.

[54] KNUDSEN, T., BAK, T., AND SVENSTRUP, M. Survey of wind farm controlâĂŤpower and fatigue optimization. *Wind Energy 18*, 8 (2015), 1333–1351.

[55] KROGSTAD, P. Å., AND ERIKSEN, P. E. 'blind test' workshop calculations for a model wind turbine.

[56] KROGSTAD, P. Å., AND ERIKSEN, P. E. 'blind test' calculations of the performance and wake development for a model wind turbine. *Renew. Energy 50* (2013), 325–333.

[57] LE CLAINCHE, S., LORENTE, L. S., AND VEGA, J. M. Wind predictions upstream wind turbines from a lidar database. *Energies 11*, 3 (2018), 543.

[58] LESSHAFFT, L., SEMERARO, O., JAUNET, V., CAVALIERI, A. V., AND JORDAN, P. Resolvent-based modeling of coherent wave packets in a turbulent jet. *Phys. Rev. Fluids 4*, 6 (2019), 063901.

[59] LEWEKE, T., QUARANTA, H., BOLNOT, H., BLANCO-RODRÍGUEZ, F., AND LE DIZÈS, S. Long-and short-wave instabilities in helical vortices. In *J. Phys. Conf. Ser* (2014), vol. 524, p. 012154.

[60] LIGNAROLO, L., RAGNI, D., SCARANO, F., FERREIRA, C. S., AND VAN BUSSEL, G. Tip-vortex instability and turbulent mixing in wind-turbine wakes. *J. Fluid Mech. 781* (2015), 467–493.

[61] LUHAR, M., SHARMA, A., AND MCKEON, B. On the structure and origin of pressure fluctuations in wall turbulence: predictions based on the resolvent analysis. *J. Fluid Mech.* (2014), 1–33.

[62] LUMLEY, J. *Stochastic tools in turbulence*. Applied mathematics and mechanics. Academic Press, 1970.

[63] MAO, X., AND SØRENSEN, J. Far-wake meandering induced by atmospheric eddies in flow past a wind turbine. *J. Fluid Mech. 846* (2018), 190–209.

[64] MARTÍNEZ-TOSSAS, L. A., CHURCHFIELD, M. J., AND LEONARDI, S. Large eddy simulations of the flow past wind turbines: actuator line and disk modeling. *Wind Energy 18*, 6 (2015), 1047–1060.

[65] MARTÍNEZ-TOSSAS, L. A., CHURCHFIELD, M. J., AND MENEVEAU, C. Optimal smoothing length scale for actuator line models of wind turbine blades based on gaussian body force distribution. *Wind Energy 20*, 6 (2017), 1083–1096.

[66] MEDICI, D. *Experimental studies of wind turbine wakes: power optimisation and meandering*. PhD thesis, KTH, 2005.

[67] MO, J.-O., CHOUDHRY, A., ARJOMANDI, M., AND LEE, Y.-H. Large eddy simulation of the wind turbine wake characteristics in the numerical wind tunnel model. *J. Wind. Eng. Ind. Aerodyn. 112* (2013), 11–24.

[68] MORRA, P., SEMERARO, O., HENNINGSON, D. S., AND COSSU, C. On the relevance of reynolds stresses in resolvent analyses of turbulent wall-bounded flows. *J. Fluid Mech. 867* (2019), 969–984.

[69] MULD, T. W., EFRAIMSSON, G., AND HENNINGSON, D. S. Flow structures around a high-speed train extracted using proper orthogonal decomposition and dynamic mode decomposition. *Comput. Fluids 57* (2012), 87–97.

[70] MUNTERS, W., AND MEYERS, J. Dynamic strategies for yaw and induction control of wind farms based on large-eddy simulation and optimization. *Energies 11*, 1 (2018), 177.

[71] OKULOV, V., AND SØRENSEN, J. N. Stability of helical tip vortices in a rotor far wake. *J. Fluid Mech. 576* (2007), 1–25.

[72] ORLANDI, P., AND LEONARDI, S. Dns of turbulent channel flows with two-and three-dimensional roughness. *J. Turbul.*, 7 (2006), N73.

[73] ORLANSKI, I. A simple boundary condition for unbounded hyperbolic flows. *J. Comput. Phys. 21* (1976), 251–269.

[74] PALMA, J., CASTRO, F. A., RIBEIRO, L. F., RODRIGUES, A., AND PINTO, A. Linear and nonlinear models in wind resource assessment and wind turbine micro-siting in complex terrain. *J. Wind. Eng. Ind. Aerodyn. 96*, 12 (2008), 2308–2326.

[75] PICARD, C., AND DELVILLE, J. Pressure velocity coupling in a subsonic round jet. *Int. J. Heat Fluid Fl. 21*, 3 (2000), 359–364.

[76] PIERELLA, F., AND SÆTRAN, L. Wind tunnel investigation on the effect of the turbine tower on wind turbines wake symmetry. *Wind Energy 20*, 10 (2017), 1753–1769.

[77] POPE, S., POPE, S., ECCLES, P., AND PRESS, C. U. *Turbulent Flows*. Cambridge University Press, 2000.

[78] PORTÉ-AGEL, F., BASTANKHAH, M., AND SHAMSODDIN, S. Wind-turbine and wind-farm flows: A review. *Boundary Layer Meteorol.* (2019), 1–59.

[79] REN. Renewable 2019. market analysis and forecast from 2019 to 2024. Tech. rep., International Energy Agency, 10 2019.

[80] REYNOLDS, W., AND HUSSAIN, A. The mechanics of an organized wave in turbulent shear flow. part 3. theoretical models and comparisons with experiments. *J. Fluid Mech. 54*, 2 (1972), 263–288.

[81] ROCCHIO, B., CIRI, U., SALVETTI, M. V., AND LEONARDI, S. Appraisal and calibration of the actuator line model for the prediction of turbulent separated wakes. *Wind Energy 23*, 5 (2020), 1231–1248.

[82] ROWLEY, C. W., MEZIC, I., BAGHERI, S., SCHLATTER, P., AND HENNINGSON, D. S. Spectral analysis of nonlinear flows. *J. Fluid Mech. 641*, 1 (2009), 115–127.

[83] SAGAUT, P. *Large eddy simulation for incompressible flows: an introduction*. Springer Science & Business Media, 2006.

[84] SANDERSE, B., VAN DER PIJL, S., AND KOREN, B. Review of computational fluid dynamics for wind turbine wake aerodynamics. *Wind energy 14*, 7 (2011), 799–819.

[85] SANTONI, C., CARRASQUILLO, K., ARENAS-NAVARRO, I., AND LEONARDI, S. Effect of tower and nacelle on the flow past a wind turbine. *Wind Energy 20* (2017), 1927–1939.

[86] SANTONI, C., GARCÍA-CARTAGENA, E. J., CIRI, U., ZHAN, L., VALERIO IUNGO, G., AND LEONARDI, S. One-way mesoscale-microscale coupling for simulating a wind farm in north texas: Assessment against scada and lidar data. *Wind Energy 23*, 3 (2020), 691–710.

[87] SANZ RODRIGO, J., CHAVEZ ARROYO, R. A., MORIARTY, P., CHURCHFIELD, M., KOSOVIĆ, B., RÉTHORÉ, P.-E., HANSEN, K. S., HAHMANN, A., MIROCHA, J. D., AND RIFE, D. Mesoscale to microscale wind farm flow modeling and evaluation. *Wiley Interdiscip. Rev. Energy Environ. 6*, 2 (2017), e214.

[88] SARLAK, H., MENEVEAU, C., AND SØRENSEN, J. N. Role of subgrid-scale modeling in large eddy simulation of wind turbine wake interactions. *Renew. Energy 77* (2015), 386–399.

[89] SARMAST, S., DADFAR, R., MIKKELSEN, R. F., SCHLATTER, P., IVANELL, S., SØRENSEN, J. N., AND HENNINGSON, D. S. Mutual inductance instability of the tip vortices behind a wind turbine. *J. Fluid Mech. 755* (2014), 705–731.

[90] SCHMID, P. J. Dynamic mode decomposition of numerical and experimental data. *J. Fluid Mech. 656* (2010), 5–28.

[91] SCHMID, P. J., AND HENNINGSON, D. S. *Stability and Transition in Shear Flows*. No. v. 142 in Applied Mathematical Sciences. Springer-Verlag, 2001.

[92] SCHMIDT, O. T., TOWNE, A., RIGAS, G., COLONIUS, T., AND BRÃĹS, G. A. Spectral analysis of jet turbulence. *J. Fluid Mech. 855* (2018), 953âĂŞ982.

[93] SEENA, A., AND SUNG, H. J. Dynamic mode decomposition of turbulent cavity flows for self-sustained oscillations. *Int. J. Heat Fluid Flow 32*, 6 (2011), 1098–1110.

[94] SEGALINI, A., AND DAHLBERG, J.-Å. Blockage effects in wind farms. *Wind Energy 23*, 2 (2020), 120–128.

[95] SHEPHERD, D. G. Historical development of the windmill. Tech. rep., Cornell Univ., Ithaca, NY (USA). Dept. of Mechanical and Aerospace Engineering, 1990.

[96] SIROVICH, L. Turbulence and the dynamics of coherent structures. parts i-iii. *Q. Appl. Math. 45*, 3 (1987), 561–590.

[97] SØRENSEN, J. N., MIKKELSEN, R., SARMAST, S., IVANELL, S., AND HENNINGSON, D. Determination of wind turbine near-wake length based on stability analysis. In *J. Phys. Conf. Ser.* (2014), vol. 524, IOP Publishing, p. 012155.

[98] SØRENSEN, J. N., MIKKELSEN, R. F., HENNINGSON, D. S., IVANELL, S., SARMAST, S., AND ANDERSEN, S. J. Simulation of wind turbine wakes using the actuator line technique. *Philos. Trans. Royal Soc. A 373*, 2035 (2015), 20140071.

[99] SØRENSEN, J. N., AND SHEN, W. Z. Computation of wind turbine wakes using combined navier-stokes/actuator-line methodology. In *1999 European Wind Energy Conference and Exhibition* (1999), pp. 156–159.

[100] STATNIKOV, V., SAYADI, T., MEINKE, M., SCHMID, P., AND SCHRÖDER, W. Analysis of pressure perturbation sources on a generic space launcher afterbody in supersonic flow using zonal turbulence modeling and dynamic mode decomposition. *Phys. Fluids 27*, 1 (2015), 016103.

[101] STEVENS, R. J., AND MENEVEAU, C. Flow structure and turbulence in wind farms. *Annu. Rev. Fluid Mech. 49* (2017).

[102] TAMMISOLA, O., AND JUNIPER, M. Coherent structures in a swirl injector at re = 4800 by nonlinear simulations and linear global modes. *J. Fluid Mech. 792* (2016), 620–657.

[103] TOWNE, A., LOZANO-DURÃĄN, A., AND YANG, X. Resolvent-based estimation of spaceâĂŞtime flowÂăstatistics. *J. Fluid Mech. 883* (2020), A17.

[104] TOWNE, A., SCHMIDT, O. T., AND COLONIUS, T. Spectral proper orthogonal decomposition and its relationship to dynamic mode decomposition and resolvent analysis. *J. Fluid Mech. 847* (2018), 821–867.

[105] VERHULST, C., AND MENEVEAU, C. Large eddy simulation study of the kinetic energy entrainment by energetic turbulent flow structures in large wind farms. *Phys. Fluids 26*, 2 (2014), 025113.

[106] VERMEER, L., SØRENSEN, J. N., AND CRESPO, A. Wind turbine wake aerodynamics. *Prog. Aerosp. Sci. 39*, 6-7 (2003), 467–510.

[107] VIOLA, F., IUNGO, G. V., CAMARRI, S., PORTÉ-AGEL, F., AND GALLAIRE, F. Prediction of the hub vortex instability in a wind turbine wake: stability analysis with eddy-viscosity models calibrated on wind tunnel data. *J. Fluid Mech. 750* (2014).

[108] VIOLA, F., IUNGO, G. V., CAMARRI, S., PORTÉ-AGEL, F., AND GALLAIRE, F. Instability of wind turbine wakes immersed in the atmospheric boundary layer. *J. Phys. Conf. Ser. 625* (jun 2015), 012034.

[109] WRAY, A. A. Minimal storage time advancement schemes for spectral methods. *NASA Ames Research Center, California, Report No. MS 202* (1990).

[110] WU, Y.-T., AND PORTÉ-AGEL, F. Simulation of turbulent flow inside and above wind farms: model validation and layout effects. *Boundary Layer Meteorol. 146*, 2 (2013), 181–205.

[111] YANG, X., PAKULA, M., AND SOTIROPOULOS, F. Large-eddy simulation of a utility-scale wind farm in complex terrain. *Appl. Energy 229* (2018), 767–777.